

## Interferometric Photonic Sensors in Silicon-On-Insulator Waveguides

*To my misses, the lovely Lisa X*

# **Interferometric Photonic Sensors in Silicon-On-Insulator Waveguides**

by

ADAM WILLIAM PRESCOTT

B.Sc. Honors Photonics (Wilfrid Laurier University) 2006

A Thesis  
Submitted to the School of Graduate Studies  
in Partial Fulfilment of the Requirements  
for the Degree  
Master of Applied Science

McMaster University  
©Copyright via Adam W. Prescott, 2008

MASTER OF APPLIED SCIENCE (2008)

(Engineering Physics)

McMaster University

Hamilton, Ontario

TITLE: Interferometric Photonic Sensors in Silicon-On-Insulator Waveguides

AUTHOR: Adam William Prescott

SUPERVISOR: Dr. Paul E. Jessop

NUMBER OF PAGES: vi,142

# Abstract

An optical temperature sensor and Fourier spectrometer, working in the 1550nm telecommunications wavelength range, were fabricated in silicon-on-insulator. Both devices were based on asymmetric Mach-Zehnder Interferometer waveguide geometries. The temperature sensor underwent a two phase design. The various asymmetry factors, due to different path length differences, of the Mach-Zehnder arms resulted in different levels of temperature sensitivity, which in turn was the driving mechanism behind the Fourier spectrometer. Due to the asymmetry of the Mach-Zehnder arms, there exists an inherent optical path length difference which is further changed with temperature variation due to the thermo-optic effect. The phase I temperature sensor showed an accuracy of 1-2°C and a sensitivity of 0.5°C for  $\Delta L$  of 37.23 $\mu\text{m}$  and 23.46 $\mu\text{m}$ , respectively. The phase II temperature sensor design, which allowed for self normalization, resulted in a 1°C temperature accuracy and a 0.5°C sensitivity for a  $\Delta L$  of 27.85 $\mu\text{m}$ . Both the phase I and II temperature sensors showed repeatable and stable results for the temperature range of 20-100°C, and agreed well with the theoretical design performance. Upon analysis of the highly asymmetric Mach-Zehnder designs it was found that both the 1.05cm and 3.05cm path length differences resulted in a temperature accuracy of 0.1°C, with a 0.05°C sensitivity over a small temperature range.

The Fourier spectrometer exhibited decent agreeability with theoretical design performance and demonstrated proof of concept. A 1.05cm path length difference was insufficient to resolve two wavelengths at 1546.12nm and 1564.68nm, which agreed with the theoretical model. However, the 3.05cm  $\Delta L$  was sufficient to resolve the two wavelengths in a repeatable manner.

# Acknowledgements

I would like to take this opportunity to thank those that have helped me over the past two years, and without whom, this would not be possible. First and foremost, I would like to send my full gratitude to my supervisor Dr. Paul Jessop, who introduced and taught me about the vast and interesting world of SOI. Dr. Jessop gave me the opportunity to take on this project and always had a direction to point me in. I would also like to thank Doug Bruce and Doris Stevanovic for countless hours of invaluable discussion and training. The first year was a steep learning curve, and if it was not for the experienced and knowledge of my lab mates Mike Bulk, Chris Brooks, and Edgar Huante Ceron, the curve would have been impossible to climb. Although there are many people to mention, this needs to be kept brief. I thank those from the Team Jessop Lab for keeping things light and entertaining.

To my misses Lisa, and my Family, I send you my deepest gratitude for being supportive and understanding. Time was not always a commodity, but without you I would have truly been lost. Thank you for always supporting my goals.

Cheers...

---

# Contents

---

<b>Contents</b>	<b>i</b>
<b>List of Figures</b>	<b>iii</b>
<b>List of Tables</b>	<b>vi</b>
<b>1 Introduction</b>	<b>1</b>
1.1 The Mach-Zehnder Interferometer . . . . .	2
1.1.1 MZI Operational Properties . . . . .	5
1.2 Refractive Index . . . . .	6
1.2.1 Thermo-Optic Effect . . . . .	10
1.3 Photoelastic Effect . . . . .	12
1.4 Fourier Transform Spectrometer . . . . .	13
1.5 Polarization of Light in Waveguides . . . . .	16
1.6 Optical Vibration / Temperature Sensors and Spectrometers	17
1.6.1 Vibration Sensors . . . . .	17
1.6.2 Temperature Sensors . . . . .	20
1.6.3 Prism Spectrometer . . . . .	26
<b>2 Theory</b>	<b>29</b>
2.1 Electromagnetic Wave Propagation . . . . .	30
2.1.1 Plane Waves . . . . .	33
2.1.2 Plane Waves at an Interface . . . . .	34
2.2 Plane Waves in an Asymmetric Slab Waveguide . . . . .	38
2.3 Rib Waveguides . . . . .	43
2.3.1 Single Mode Condition . . . . .	44
2.3.2 Effective Index Method . . . . .	47
2.3.3 Losses in SOI Rib Waveguides . . . . .	51
2.4 Strain Relation to Vibration . . . . .	58
2.5 Fourier Spectroscopy . . . . .	60
2.5.1 Fourier Transform Spectrometer . . . . .	62
2.6 Metal Clad Rib Polarizer in SOI . . . . .	64

<b>3</b>	<b>Device Design and Fabrication</b>	<b>67</b>
3.1	Waveguide Geometry . . . . .	68
3.1.1	Etch Depth and Rib Width . . . . .	68
3.1.2	Bend Radius and Y-Branched . . . . .	70
3.2	Mach-Zehnder Design . . . . .	73
3.2.1	Mach-Zehnder Temperature Sensor . . . . .	74
3.2.2	Mach-Zehnder Vibration Sensor . . . . .	77
3.2.3	Mach-Zehnder Fourier Spectrometer . . . . .	78
3.2.4	Polarizers on SOI Rib Waveguides . . . . .	78
3.3	Fabrication . . . . .	79
3.3.1	Waveguides . . . . .	79
3.3.2	Polarizers . . . . .	79
<b>4</b>	<b>Results and Discussion</b>	<b>87</b>
4.0.3	Experimental Setup . . . . .	87
4.1	Asymmetric Mach-Zehnder Temperature Sensor . . . . .	89
4.1.1	Phase I Temperature Sensor . . . . .	89
4.1.2	Phase II Temperature Sensor . . . . .	94
4.2	Asymmetric Mach-Zehnder Fourier Spectrometer . . . . .	98
4.3	Polarizer on SOI Rib Waveguide . . . . .	106
<b>5</b>	<b>Conclusion and Future Work</b>	<b>109</b>
	<b>Bibliography</b>	<b>113</b>
<b>A</b>	<b>Maple Programs</b>	<b>121</b>
A.1	Single Mode Condition . . . . .	122
A.2	Effective Index Method . . . . .	123
A.3	Bend Loss . . . . .	125
<b>B</b>	<b>MatLab Programs</b>	<b>133</b>
B.1	Fourier Spectrometer Program . . . . .	133
<b>C</b>	<b>Various FFT Outputs due to Zero Buffering</b>	<b>135</b>
<b>D</b>	<b>Photomask</b>	<b>137</b>
<b>E</b>	<b>List of Symbols and Abbreviations</b>	<b>141</b>

---

# List of Figures

---

1.1	MZI based on Rib Waveguides . . . . .	2
1.2	Dispersion Relation for Silicon based on Equation 1.6 . . . . .	9
1.3	Various Thermo-Optic Coefficients of Silicon Above Room Temperature [1, p.368] . . . . .	11
1.4	Michelson Interferometer Diagram (Adapted from [2, pg.536]) . . . . .	14
1.5	Silicon Cantilever with Fiber Optic Transmission . . . . .	18
1.6	Fiber Optic Cantilever . . . . .	19
1.7	Silicon Energy-Band Structure (Adapted from J.R. Chelikowsky and M.L.Cohen, Phys. Rev. B 14 (1976) 556 ) . . . . .	21
1.8	Indirect Band-Energy Gap with respect to Temperature . . . . .	23
1.9	Fiber Bragg Grating . . . . .	24
1.10	Output Spectrum of Fiber Bragg Grating at a Constant Temperature (Adapted from Encyclopedia of Laser Physics and Technology) . . . . .	26
2.1	Reflection and Refraction of Plane Wave at Refractive Index Boundary . . . . .	35
2.2	Asymmetric Slab Waveguide . . . . .	38
2.3	Rib Waveguide Cross Section . . . . .	44
2.4	Single Mode Condition for Various $\alpha$ Constants . . . . .	46
2.5	Effective Index Method: Cross Sectional Analysis . . . . .	49
2.6	Effective Index Method: Topographical Analysis . . . . .	49
2.7	Metal Clad Rib Waveguide: TE and TM Modes . . . . .	65
2.8	Straight Rib Waveguides Without a Metal Cladding Layer: TE and TM Modes . . . . .	66
3.1	Rendering of Mach-Zehnder Interferometer in SOI . . . . .	68
3.2	Rib Waveguide Cross Section - SEM Image . . . . .	69
3.3	Straight Arm Y-Splitter and S-Bend Splitter . . . . .	71
3.4	Radiation Bend Loss of Fundamental Mode: TE Polarization . . . . .	73
3.5	Radiation Bend Loss of Fundamental Mode: TM Polarization . . . . .	74

3.6	Normalized Output of MZI with $\Delta L$ of $27.85\mu\text{m}$ for Various $\lambda$ , Temperature range of 200K to 500K . . . . .	75
3.7	Normalized Output of MZI with $\Delta L$ of $27.85\mu\text{m}$ for Various $\lambda$ , Temperature range of 273K to 400K . . . . .	77
3.8	Normalized Output of MZI with $\Delta L$ of $27.85\mu\text{m}$ . A Comparison of Contributing Factors when $\lambda$ is 1548.51nm . . . . .	78
3.9	Photoresist after regular processing: Note sidewall angle . . . . .	80
3.10	Surface Damage due to Micromasking after RIE . . . . .	82
3.11	Initial Silicon Surface Unprocessed and Silicon Rib Waveguide After RIE . . . . .	84
3.12	Metalization of Entire Surface and Photoresist Over Rib Waveguide . . . . .	84
3.13	Final Metalized Rib Polarizer: Cross Section View . . . . .	85
4.1	Experimental Bench Apparatus . . . . .	88
4.2	Phase I Mask Design - Set of Asymmetric MZI . . . . .	90
4.3	Normalized Theoretical Output of Phase I Device for $\lambda=1546.12\text{nm}$ . . . . .	90
4.4	Normalized Experimental Output of Phase I Device for $\lambda=1546.12\text{nm}$ . . . . .	91
4.5	Normalized Experimental Extinction Ratios of Phase I Device via Wavelength Tuning . . . . .	92
4.6	Normalized Experimental Wavelength Tuning: Tunable Laser Source Directly Into Optical Power Meter . . . . .	94
4.7	Phase I - Wavelength Variation with Fiber to Sample Distance Varied . . . . .	95
4.8	Phase II Mask Design - Asymmetric MZI and Normalization Arm . . . . .	95
4.9	Phase II Experimental Data Type 1 - Normalized . . . . .	97
4.10	Phase II Experimental Data Type 2 - Normalized . . . . .	98
4.11	Phase II Experimental Data - Fiber Bonded . . . . .	99
4.12	High Asymmetry MZI ( $\Delta L = 1.05\text{cm}$ ) - Normalized experimental against theoretical for $1^\circ$ temperature range and $0.2\text{nm}$ wavelength scan . . . . .	100
4.13	High Asymmetry MZI ( $\Delta L = 3.05\text{cm}$ ) - Normalized experimental with polarization against theoretical for $1^\circ$ temperature range and $0.1\text{nm}$ wavelength scan . . . . .	100
4.14	High Asymmetry MZI ( $\Delta L = 1.05\text{cm}$ ) - Theoretical FFT output for $\lambda=1546.12\text{nm}$ and $\lambda=1564.68\text{nm}$ . Top - Input Wavelengths / Center - Output Interference Spectrum / Bottom - FFT of Output Interference Spectrum . . . . .	102
4.15	High Asymmetry MZI ( $\Delta L = 3.05\text{cm}$ ) - Theoretical FFT output for $\lambda=1546.12\text{nm}$ and $\lambda=1564.68\text{nm}$ . Top - Input Wavelengths / Center - Output Interference Spectrum / Bottom - FFT of Output Interference Spectrum . . . . .	103
4.16	High Asymmetry MZI ( $\Delta L = 1.05\text{cm}$ ) - Experimental FFT output for $\lambda=1546.12\text{nm}$ and $\lambda=1564.68\text{nm}$ . . . . .	104

4.17 High Asymmetry MZI ( $\Delta L = 3.05\text{cm}$ ) - Experimental FFT output for $\lambda=1546.12\text{nm}$ and $\lambda=1564.68\text{nm}$ . . . . .	105
4.18 Aluminum Clad Rib Polarizer - TM Input and TM Input Normalized . . . . .	107
4.19 Aluminum Clad Rib Polarizer - TE Input and TE Input Normalized . . . . .	108
A.1 Cross Section of Rib Waveguide With Geometric Variables . . . . .	121
C.1 Sample 1 MZI ( $\Delta L = 3.05\text{cm}$ ) - Experimental FFT output for $\lambda=1546.12\text{nm}$ and $\lambda=1564.68\text{nm}$ with Various Zero Buffering . . . . .	136
C.2 Sample 2 MZI ( $\Delta L = 3.05\text{cm}$ ) - Experimental FFT output for $\lambda=1546.12\text{nm}$ and $\lambda=1564.68\text{nm}$ with Various Zero Buffering . . . . .	136
D.1 Phase I Photomask Tile . . . . .	138
D.2 Phase II Photomask . . . . .	139

---

# List of Tables

---

2.1 Compliance and Photoelastic Coefficients for Silicon . . . . . 59

# Chapter 1

---

## Introduction

---

The research described in this thesis was motivated by a need in the steel industry for simple temperature and vibration sensors that can survive in a harsh environment and do not require any electrical signals at the point of measurement. The solution that was developed employs an asymmetric Mach-Zehnder interferometer (MZI) fabricated in a silicon-on-insulator (SOI) optical waveguide. The optical path length difference between the two arms of a MZI is temperature dependant, resulting in a sinusoidal dependence of the MZI output signal on temperature. By using a small path length difference, on the order of tens of microns, the sensor can be made to operate so that the entire temperature range of interest encompasses less than one cycle of the sinusoid. This removes problems of temperature ambiguity and sensitivity null points, but it results in temperature sensitivity of only about 2 degrees. This sensitivity is adequate for the anticipated application, however. We also investigated a quite different application of

the asymmetric MZI.

By making the path length difference very large, on the order of 1-3cm, the output signal becomes much more temperature sensitive. For a monochromatic input signal the output will sweep through hundreds of cycles of a sine wave for a temperature tuning of 40 degrees, which would make a temperature sensor more complicated than necessary. But we have shown that such a device acts as an integrated optical version of a Fourier-transform spectrometer.

## 1.1 The Mach-Zehnder Interferometer

Named after physicists Ludwig Mach and Ludwig Zehnder, the MZI is a well known and abundantly used device in the world of optics. The basic operational principle of the MZI is phase shift sensitivity due to splitting and re-combining of coherent light signals along two separate arms, as shown in Fig. 1.1. It is used for various applications, but is most well know for its robust applications in modulation [3] and sensing [4, 5, 6].

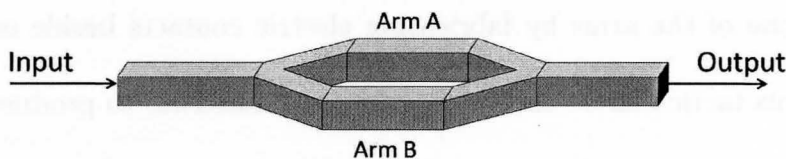


Figure 1.1: MZI based on Rib Waveguides

The principle of operation lies in the splitting of the light signal. In

an ideal system, the signal is split, with each separate propagating signal containing half the power of the original. In the case of a symmetric MZI, the two signals will re-combine at the output, and because the optical path lengths are identical, there will be no difference in phase between the two signals. Hence, upon recombination, the two separate signals will re-form the original input signal with the original input power. However, if the MZI is asymmetric, there will be an inherent phase shift between the two recombining signals due to a difference in the optical path lengths of the two arms. The output field is a superposition of the combining fields from the two arms and the output intensity is a sinusoidal function of the phase difference.

In the case of a symmetric MZI, there is no inherent phase change, so the output will not vary with the input wavelength or device temperature. However, there are many available ways to manipulate parameters surrounding an arm of the MZI so as to break the symmetry. One example of parameter manipulation involves creating a diaphragm under the arm which would cause sensitivity to pressure or vibration [7]. One can create an electric field across one of the arms by fabricating electric contacts beside one of the arms. This tactic can be used in electro-optic materials to produce RF modulators. Moreover, thermal heating of a contact pad which is directly above one of the arms can cause thermal modulation of the signal. There are an abundance of possibilities for symmetric MZI applications, however,

since there is no inherent path length difference to cause a passive phase change, one of the arms must be actively influenced in order for an output signal change to occur.

The asymmetric MZI will have an inherent phase difference between the two arms. The phase difference comes from the optical path length difference of the two adjacent arms. Due to this optical path length difference, the overall system will be passively sensitive to thermal changes. As coherent light propagates along each arm, changes in the system will cause different optical responses in each of the arms due to the non-uniform path lengths. Upon recombination of the two signals, there will be an additional phase change between the arms. This additional phase change will give rise to variations in the output signal with respect to physical manipulation. On this basis, an asymmetric MZI could be designed to give optical responses to physical stimulus such as variation in temperature, pressure, vibration, or acceleration.

$$L_{opt} = N_{eff}L \quad (1.1)$$

The optical path length of each is given by equation 1.1, where L is the physical path length of each arm. A list of symbols can be found in appendix... A monochromatic signal that is split and then recombined in the MZI will have an output power that depends on wavelength, temperature, or strain changes, since these all contribute to changes in the path length difference. In the case of a temperature sensor, the greatest change

comes from the thermo-optic effect, though there is also a thermal expansion component involved.

### 1.1.1 MZI Operational Properties

In order to design a device that will work in accordance with design specifications, the basic operational properties of the MZI need to be fully understood. In the case of the asymmetric MZI the influence of the MZI on the original signal is described by equation 1.2. The intensity radiating from the output of the MZI, neglecting all loss, is due to the phase offset from the signals propagating in the two arms. Each arm has a different length, denoted  $L_1$  and  $L_2$ , and due to this difference, there is a path length difference between the arms, denoted  $\Delta L$ . One can easily see that the optical path length difference,  $N_{eff}\Delta L$ , will inherently have an effect on the outcome of the signal due to the nature of the cosine function. One can utilize this oscillating behavior to create a sensor, for if the path length, wavelength, or effective index are changed, the phase along each arm will change in turn, and hence cause a different interference pattern upon signal recombination.

$$I = \cos(k_o[N_1L_1 - N_2L_2]) \quad (1.2)$$

where  $N_1$  and  $N_2$  are the effective indices in each of the arms.

In the case of temperature variation, there is a change in effective index, as well as path length. The phase change caused by the effective index change is two orders of magnitude greater than the phase change caused by

thermal path length variation. However, for thorough analysis, one should take both into account. The variation in effective index with temperature, known as the thermo-optic effect is denoted as  $\frac{dn}{dT}$ , and the linear thermal expansion is denoted as  $\frac{dL}{dT}$ . Based on this, the output intensity of an asymmetric MZI will depend on temperature as

$$I(T) = \cos \left( \left( n + \frac{dn}{dT} \Delta T \right) k_0 \left( \Delta L + \frac{dL}{dT} \Delta T \right) \right) \quad (1.3)$$

Upon use of this, the MZI now has a temperature dependence that can be conditioned to fall into operational specifications.

## 1.2 Refractive Index

The refractive index is a dimensionless parameter that depends on many variables such as temperature, stress/strain, wavelength, and material density. Topics, with regards to refractive index, which are of lesser importance to the understanding of this thesis will be described in this (Refractive Index) section for purposes of clarity and completeness.

The velocity at which light propagates in a medium,  $v$ , is directly dependant on the refractive index of the material. The relationship between  $v$  and the speed of light in a vacuum,  $c$ , is governed by equation 1.4, where  $n$  is the refractive index. This relationship shows that as the refractive index increases, the velocity of the propagating light wave will decrease. More directly, phase velocity of electromagnetic waves travelling in a nonmag-

netic dielectric material is dependant on the relative permittivity  $\epsilon_r$  of the material as shown in 1.5, where  $\epsilon_o$  is the permittivity of free space and  $\mu_o$  is the permeability of free space [8, p.7]. In substituting  $v$  from equation 1.5 into 1.4, one can easily find the relationship between the refractive index and the relative permittivity. Due to the nature of crystalline material, the refractive index for waves polarized along different crystal directions can differ. However, silicon is uniaxial in nature, so the following arguments will be based on the refractive index of crystalline silicon.

$$n = \frac{c}{v} \quad (1.4)$$

$$v^2 = \frac{1}{\epsilon_r \epsilon_o \mu_o} \quad (1.5)$$

The index of refraction is directly related to the dielectric constant  $\epsilon$ , where the dielectric constant can take on complex values, and hence, the refractive index can also take on complex values. The complex dielectric constant is  $\epsilon = \epsilon_1 - i\epsilon_2$ . The index of refraction is related to the dielectric constant via  $n^2 = \epsilon = \epsilon_r$ , where  $n = n_1 + ik$ . The values  $\epsilon_1$  and  $n_1$  are the real components, and the  $\epsilon_2$  and  $k$  and the complex components of the dielectric and refractive index respectively. Equating the real and imaginary parts gives  $\epsilon_1 = (n_1^2 - k^2)$  and  $\epsilon_2 = 2n_1n_2$ .

As the wavelength of light, propagating through a medium, is altered, the refractive index and the velocity of the travelling wave changes [2, p.119]. Coherent light travelling in air ( $n=1$ ), will be travelling at  $c$ , as this light wave enters a second medium of higher index, the velocity of the light wave

will decrease. This decrease in propagation speed results in a decrease of wavelength as well, though the frequency will remain the same as the original vacuum frequency. The changing wavelength, and hence propagation speed of the light wave, will give rise to a change in light-medium interaction, and the outcome is a refractive index dependence on wavelength. In the case of silicon, when the wavelength of interest is far from the absorbing region, the refractive index will decrease with increasing wavelength [9], as described in equation 1.6 [10]. Equation 1.6 is valid for wavelengths greater than  $1.2\mu\text{m}$ , and a graphical representation for wavelengths of greatest interest is shown in Fig. 1.2. However, when approaching the absorption edge of silicon ( $\sim 1046\text{nm}$ ) from lower wavelengths, the refractive index tends to increase [9] relative to the predictions of equation 1.6 and Fig. 1.2.

$$n^2 = 11.6858 + \frac{0.939818}{\lambda^2(\mu\text{m})} + \frac{0.009934}{\lambda^2(\mu\text{m}) - 1.22567} \quad (1.6)$$

An important point to note is the dependence of refractive index on material density and crystalline uniformity for silicon. The refractive index has a dependence on the density of silicon, where crystalline silicon has the highest density, and porous silicon will have the lowest density. Silicon itself can come in an array of states; bulk, semi-crystalline, amorphous, and porous. Bulk silicon is in crystal form and has a uniform and consistent diamond cubic lattice structure throughout. In amorphous silicon there is no apparent crystal structure and the refractive index can range from 2.4 to

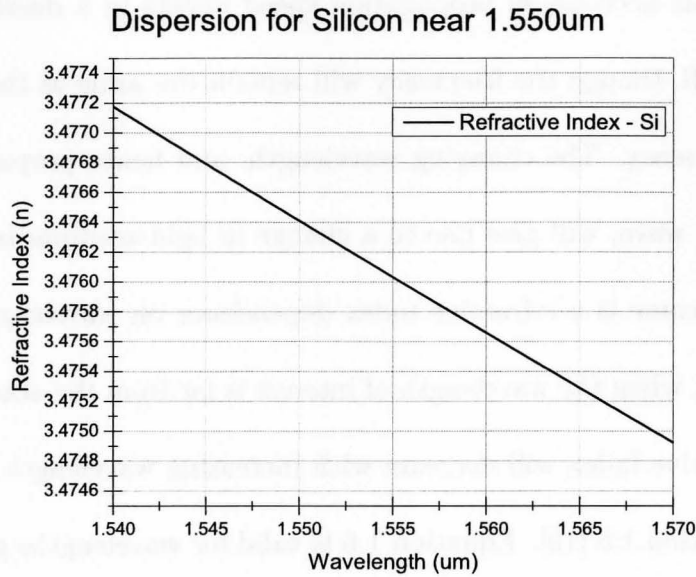


Figure 1.2: Dispersion Relation for Silicon based on Equation 1.6

3.2 [11]. Semi-crystalline silicon, however, is a mixture of amorphous and crystalline, in which the majority is amorphous and there are patches of crystalline silicon within the amorphous. Porous silicon, however, is a network of capillaries, in which air or silicon dioxide is present. The capillaries, or pores, can range in size from 2nm to 50nm. As the porosity increases from 0 percent to one hundred percent the index decreases with a linear trend from 3.47 to 1. Depending on the ratio of silicon to air, the refractive index varies accordingly. The above mentioned forms of silicon will have various refractive indices due to the nature of the material itself, however, detail will not be mentioned, but the reader can refer to the following references.

[12, 11, 10]

### 1.2.1 Thermo-Optic Effect

The refractive index of silicon is dependent on many factors, though for the scope of this thesis most will not be discussed. However, of great importance is the temperature dependence of the index of refraction due to the implications on device design and functionality.

The temperature tuning of the refractive index for constant pressure, is known as the thermo-optic effect, and if not appropriately analyzed can have devastating effects on device performance. The notation,  $\frac{dn}{dT}$ , is self explanatory, where units are in Kelvins or per degree Celsius. In the case of semiconductor materials, the thermo-optic effect causes index changes per temperature variation, on the order of  $10^{-6}K^{-1}$  to  $10^{-3}K^{-1}$  [1]. This small effect will have implications on modal confinement as well as wave propagation characteristics if the operational temperature range is large.

A model described in [1, p.370] describes the thermo-optic effect with regards to the temperature dependence of a semiconductor bandgap. The thermo-optic effect is described as follows;

$$\frac{dn}{dT} = \frac{n^2 - 1}{2n} \left( -3 \frac{dL}{dT} \frac{1}{L} - \frac{2}{E_g} \frac{dE_g}{dT} \frac{1}{1 - (\frac{E}{E_g})^2} \right) \quad (1.7)$$

$$E_g(T) = E_g(0) - \frac{\alpha T^2}{T + \beta} \quad (1.8)$$

Where  $n$ , the refractive index,  $\frac{1}{L} \frac{dL}{dT}$ , the thermal expansion coefficient, and  $\frac{dE_g}{dT}$ , are all temperature dependant. The accepted value of the thermal

expansion coefficient of silicon is around  $2.5 \times 10^{-6} K^{-1}$  [10] near room temperature. However, a more precise coefficient is,  $\frac{1}{L} \frac{dL}{dT} = 3.725 \times 10^{-6} (1 - \exp(-5.88 \times 10^{-3}(T - 124))) + 5.548 \times 10^{-10} T$  [10], which is valid between the temperatures 120K to 1500K. The temperature dependence of the bandgap, when at constant volume, is given by equation 1.8, where  $E_g(0)$ , is the indirect energy gap of silicon at 0 Kelvin, and  $\alpha$  and  $\beta$  are material constants, which will be described in more detail later in the chapter. Though many groups have reported various thermo-optic coefficients near room temperature, as shown in Fig. 1.3, for the wavelength of 1550nm, the best appears to be  $1.818 \times 10^{-4} K^{-1}$  labeled "this work", which is valid for temperatures from around 300K to 400K.

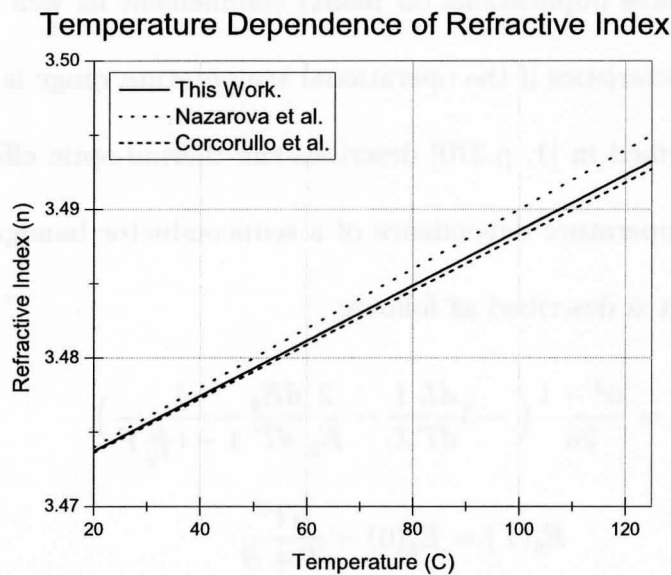


Figure 1.3: Various Thermo-Optic Coefficients of Silicon Above Room Temperature [1, p.368]

### 1.3 Photoelastic Effect

The photoelastic effect refers to a change in refractive index in a periodic crystal due to an induced stress or strain in the system. As a rigid body is acted upon by an external force, that stress will cause a known amount of strain in the body that is being acted upon. Strain is a quantification of material deformation with respect to the magnitude of stress. In the most simple case, which is in one dimension, strain is conceived as the change in length due to the material deformation with respect to the original length, and is noted by the symbol  $\epsilon$ .

$$\epsilon = \frac{\Delta L}{L} \quad (1.9)$$

However, most systems are not as simple as one dimension, and for a solid system of three dimensions the strain is more accurately depicted by a 3x3 tensor with the following flavor.

$$\epsilon = \begin{pmatrix} \epsilon_{11} & \epsilon_{12} & \epsilon_{13} \\ \epsilon_{21} & \epsilon_{22} & \epsilon_{23} \\ \epsilon_{31} & \epsilon_{32} & \epsilon_{33} \end{pmatrix} \quad (1.10)$$

where the subscripts 1,2, and 3 refer to the strain along the orthogonal axes x, y, and z, respectively [13]. Moreover, the subscripts 11, 22, and 33 are normal strain components along one of the axes and scripts such as 12 and 31 refer to shear strains which are perpendicular to an axis. However, since the strain tensor is symmetric about the diagonal, i.e.  $\epsilon_{xy} = \epsilon_{yx}$ , one is able

to simplify the tensor from a 9 component system down to a 6 component system as follows.

$$\epsilon = \begin{pmatrix} \epsilon_1 & \epsilon_6 & \epsilon_5 \\ \epsilon_6 & \epsilon_2 & \epsilon_4 \\ \epsilon_5 & \epsilon_4 & \epsilon_3 \end{pmatrix} \quad (1.11)$$

The photoelastic effect itself is described by the following equation,

$$\Delta\left(\frac{1}{n^2}\right)_i = \sum_{j=1}^6 p_{ij}\epsilon_j \quad (1.12)$$

where,  $p$  is the photoelastic tensor for silicon, and  $\epsilon$  is a strain field which takes into account the 6x6 compliance tensor and stress field, as will be described later in chapter 2.

The basic argument behind the photoelastic effect, in a silicon waveguide, is that a force acts upon a body, which induces a stress in the system, this stress goes on to alter the crystal axis of the silicon, and in doing so causes a dynamic stress along a waveguide. The stress in the waveguide alters the refractive index and thus causes a change in the propagational properties of light.

## 1.4 Fourier Transform Spectrometer

A spectrometer is an instrument used to measure the relative intensity of an input lightwave as a function of wavelength. A conventional Fourier spectrometer is based on a Michelson interferometer, as shown in Fig. 1.4.

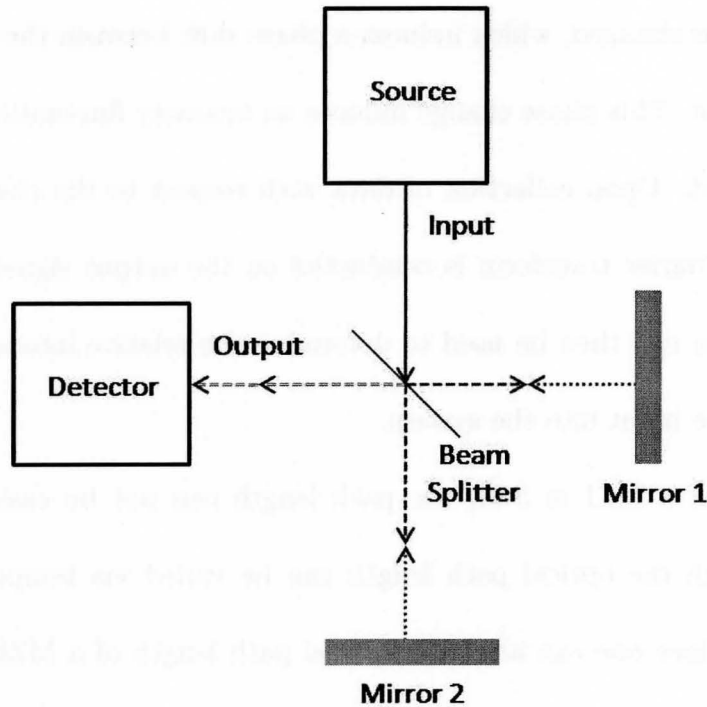


Figure 1.4: Michelson Interferometer Diagram (Adapted from [2, pg.536])

A Michelson interferometer, assuming the source is monochromatic, will have a sinusoidal output, which can be expressed as a Fourier Transform of the source spectrum. There can be a distribution of wavelengths in the source that can be found via a Fourier transform of the output signal. Multiple coherent signals are combined within the source and sent out, as shown as the input. The input beam will contain a superposition signal, which is split by a beam splitter and consequently reflected to two mirrors. When the two mirrors are equidistant from the beam splitter, the output signal, composed of the re-combining signals reflected to mirror 1 and 2, will be the same as the output, for there will be no consequent phase shifting. However, when one of the mirrors is moved towards or away from the beam splitter,

the path length is changed, which induces a phase shift between the beams upon convergence. This phase change induces an intensity fluctuation that can be monitored. Upon collection of data with respect to the change in path length, a Fourier transform is conducted on the output signal. The Fourier transform can then be used to determine the relative intensity vs. wavelength of the input into the system.

In the case of a MZI in SOI, the path length can not be easily manipulated, though the optical path length can be varied via temperature manipulation. Since one can alter the optical path length of a MZI, there lies the basis for Fourier transform spectrometer, which will act much the same as the above described Michelson, though the range of manipulation will be slightly less. However, unlike the Michelson, a MZI in SOI has the advantage of exceptional path length precision as well as perfect signal recombination.

The idea to utilize a MZI for the purpose of a spectrometer was demonstrated through a simple program in MatLab. The program shows that for a path length difference 3.05cm, two coherent telecommunications signals at 18nm spacing could be measured for a temperature tuning range of 40°C. The temperature tuning range assumed in the MatLab program was 0°C to 100°C, however, due to experimental limitations, the experimental temperature range able to be covered is 15 to 60°C.

## 1.5 Polarization of Light in Waveguides

Polarization of light is one of the key fundamentals to understanding how a light wave propagates in a medium or a vacuum. Light itself is an electromagnetic wave in which there is both an electric and magnetic component, both of which oscillate normal to each other, and to the direction of propagation, with respect to time, and hence the wave is considered to be transverse. Terms TE and TM polarization are often used to describe polarization within a waveguide with respect to the structure of the waveguide itself. The TE polarization in a waveguide is  $\mathbf{E}$  in the waveguide plane, and TM polarization is mostly  $\mathbf{E}$  perpendicular to the waveguide plane.

Most SOI rib waveguides have air or  $\text{SiO}_2$  as the upper cladding. In the case of SOI rib waveguides there is not symmetrical confinement, for the effective index in the horizontal plane ( $N_{TE}$ ) will not be the same as the effective index in the vertical plane ( $N_{TM}$ ), which is due to the  $\text{SiO}_2$  / air barriers in the vertical plane and the silicon slab height in the horizontal plane. Although, there are cases when confinement of one of the modes is not desirable, in fact at some points it is highly desirable to propagate a single polarization, and effectively attenuate the other. Although there are manners to which one can propagate a single polarization such as polarization maintaining (PM) fiber or polarization paddles, it is often costly and time consuming to properly adhere a fiber to a rib waveguide device in a manner that locks in either TE or TM polarization. Devices, such as

MZI's, will generally give a more clean and true signal if one or the other polarization is locked in, and hence it is advantageous to design an on-board polarizer that will be highly attenuating to one polarization, but leave the other relatively unscathed.

## 1.6 Optical Vibration / Temperature Sensors and Spectrometers

Until recently the main focus of optical components has been directed towards the telecommunications industry, though lately more attention has been directed towards sensors. The nature of optical based sensors allows them to work in conditions where conventional electrical sensors would not be feasible. This section will touch on sensors that are currently used to detect vibration and temperature. As well, some possible sensors based on previous analysis will be discussed.

### 1.6.1 Vibration Sensors

#### Silicon Cantilever

A vibration sensor design based on a silicon cantilever and optical fiber coupling has been developed and tested by *Peiner et al.* [14]. The basis of this design is the utilization of a silicon cantilever to disrupt the transmitted power between two optical fibers as shown in Fig. 1.5.

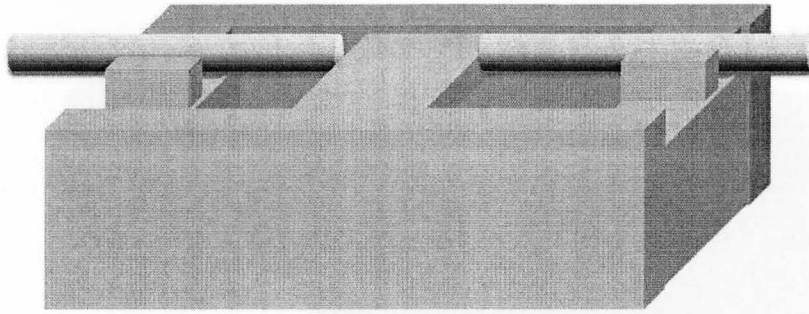


Figure 1.5: Silicon Cantilever with Fiber Optic Transmission

The fibers are set into V-grooves and aligned for maximum transmission. The cantilever is designed such that the cantilever will sit slightly above the propagational axis of the optical fiber pathway. The range of sensitivity can be tuned via cantilever length as well as position above the center of the fiber. As the system undergoes vibration, the silicon cantilever will oscillate about the point of attachment. The magnitude as well as frequency of oscillation will give rise to a modulation of the transmitted signal from fiber to fiber. The sensor design allowed for measurements in the range of 0.2g to 1.57g and was sensitive to frequencies of 150Hz and 420Hz.

### **Fiber Cantilever**

A more popular design utilizes the actual fiber as the cantilever, in that vibration causes the loose fiber to oscillate, which in turn modulates the signal transmission, as depicted in Fig. 1.6. Though the actual physics behind the vibration of a fiber is complex, the basis of operation will be

outlined from a mechanical standpoint.

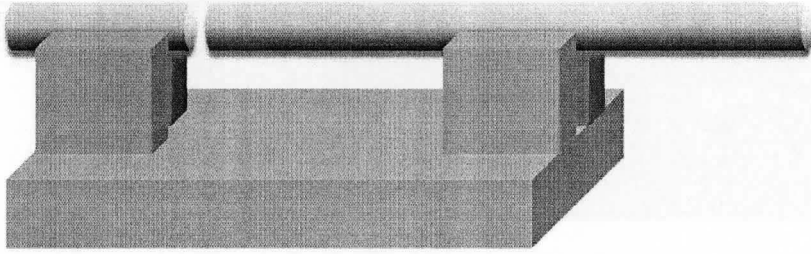


Figure 1.6: Fiber Optic Cantilever

Taking the cantilever to be a uniform rod composed of consistent material, one can determine the first resonant frequency or the required length given the first resonance via equations 1.13 and 1.14, respectively. Where  $E$  is Young's Modulus,  $I$  is the second area moment of inertia described by equation 1.15,  $\rho$  is the material density,  $A$  is the cross sectional area,  $d$  is the fiber diameter, and  $L$  is the length of the cantilever [15, 16, 17]. This is a simplified model; air resistance, material creep, inherent sag, and damping are not taken into account. The lateral displacement of the tip of the fiber is given via equation 1.16, where  $a$  is acceleration, though once again, this is a simplified analytical formula, for in actuality the fiber tip will follow a sinusoidal pattern.

$$f_1 = \frac{3.52}{2\pi L^2} \sqrt{\frac{EI}{\rho A}} \quad (1.13)$$

$$L = \frac{7.04d}{16\pi f_1} \sqrt{\frac{E}{\rho}} \quad (1.14)$$

$$I = \frac{\pi d^4}{64} \quad (1.15)$$

$$x = \frac{A\rho L^4}{8EI}a \quad (1.16)$$

By using equations 1.13 to 1.16, one can find a length of fiber that will fit the required criterion for frequency of vibration. However, the cantilever will respond linearly to frequencies that are at or below 20% of the first resonant frequency, which puts limitations on the range of operation.

In the case of one dimensional displacement, assuming a single mode fiber with a  $7\mu\text{m}$  core diameter, displacements of a few nanometers will alter the signal transmission by easily measurable amounts. The distance between the cantilever fiber and fixed fiber as shown in Fig. 1.6 will also have an effect on the sensitivity as well as signal throughput [18, 19].

The basis of signal transmission lies in the misalignment of the fiber cores. As the amplitude of vibration increases, the signal will undergo more drastic changes. The actual output signals of this design has been documented by *Kalenik et al.* [18] and *Kimura et al.* [19].

## 1.6.2 Temperature Sensors

### Semiconductor Bandgap - Signal Transmission

High purity semiconductors are highly absorbing for photon energies above the bandgap energies and highly transmitting for photon energies below the bandgap energies. The energy band structure of silicon is shown below in Fig. 1.7. Although the direct bandgap of silicon has an energy gap of 4.2eV

at room temperature, there lies an indirect energy gap which is only 1.12eV at room temperature. Due to the indirect gap having a lower potential energy it is the defining factor in the absorbing region of wavelengths.

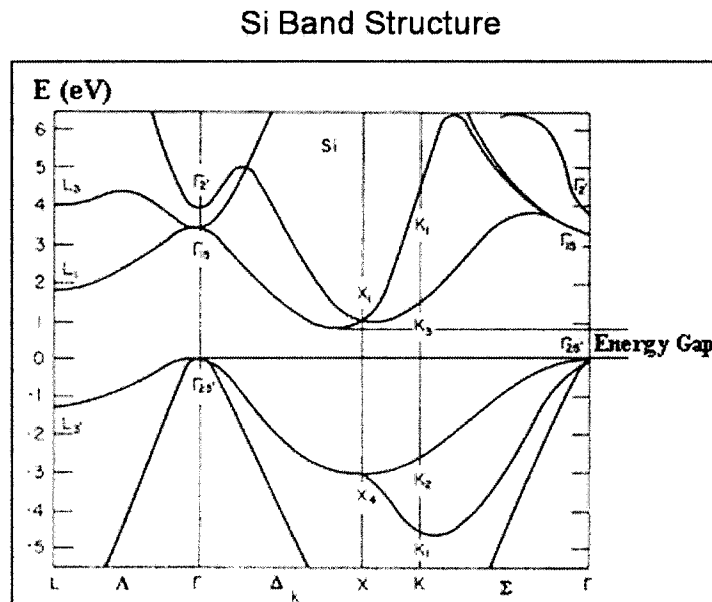


Figure 1.7: Silicon Energy-Band Structure (Adapted from J.R. Chelikowsky and M.L.Cohen, Phys. Rev. B 14 (1976) 556 )

Coherent propagating light waves will have a photon energy based on their wavelength. The bandgap energy of the material that the light is propagating through is described by equation 1.17, where  $h$  is Plank's constant,  $c$  is the speed of light, and  $\lambda$  is the wavelength. For the telecommunication wavelength of 1550nm, the photon energy is 0.80eV. This energy is well below that of the indirect gap of silicon. Because the propagating photons do not carry sufficient energy to excite electrons into the next energy level, the photon is free to travel throughout the crystal and no energy absorption will take place, hence silicon is transparent at wavelengths near 1550nm. How-

ever, when the photon energy begins to approach that of the indirect band energy, absorption will occur. Based on this, if an appropriate wavelength is chosen, near the absorption edge, there will be reduced signal transmission due to absorption.

$$E_g(\text{eV}) = \frac{hc}{\lambda_{gap}} \quad (1.17)$$

$$E_g(T) = E_g(0) - \frac{\alpha T^2}{T + \beta} \quad (1.18)$$

One of the properties of the energy band of semiconductors is a sensitivity to temperature. The formula which governs this temperature sensitivity is given by equation 1.18 [20, p.15], where  $E_g(T)$  is the energy gap at a given temperature,  $E_g(0)$ , is the energy gap at 0 Kelvin,  $\alpha$  and  $\beta$  are material constants, and  $T$  is the temperature in Kelvins. More specifically,  $\alpha$  is related to the electron-phonon interaction, and  $\beta$  is related to the Debye temperature of the semiconductor [1]. For silicon  $E_g(0)$  is 1.17eV,  $\alpha$  is  $4.9 \times 10^{-4}$ , and  $\beta$  is 655 [10]. Given these values, the indirect band energy of silicon will decrease with temperature as shown in Fig. 1.8, which is more well known as the Varshni curve.

In taking the Varshni curve as well as the band-energy temperature relation into account for Silicon, one can determine the wavelength associated with the absorption edge near room temperature to be near 1100nm for silicon. Thus, for a given thickness of silicon, there will be an signal absorption coefficient,  $\alpha$ , defined by equation 1.19, which is dependant on the temperature of the silicon slab, as defined by  $E_g(T)$  in equation 1.18, where

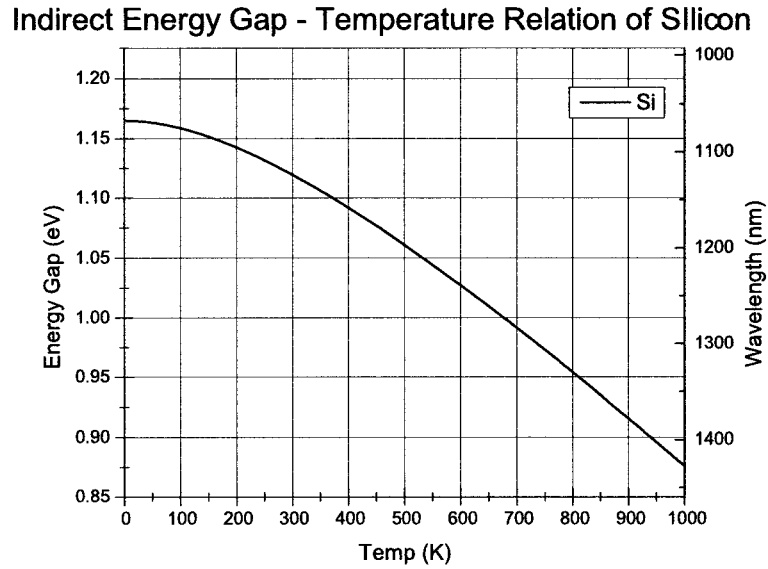


Figure 1.8: Indirect Band-Energy Gap with respect to Temperature

$h$  is Planck's constant,  $\nu$  is the frequency of the photon, and  $\gamma$  is  $\frac{3}{2}$  due to the indirect bandgap [20, p.52].

$$\alpha \propto (h\nu - E_g(T))^\gamma \quad (1.19)$$

Based on the above arguments, one can tune the sensor by increasing distance traversed by the monochromatic signal through the silicon, which would cause increased absorption. The wavelength can be adjusted to be greater than 1100nm, which in turn reduces the photon energy and thus reduces the absorption. On the other hand, by lowering the wavelength below 1100nm, the photon energy increased, and hence the absorption increases as well. The system works as a sensor in that as the temperature increases the indirect band-energy gap will decrease, thereby causing greater absorption for a fixed wavelength of 1100nm. Barry Stoute, from the Engineering

Physics Department of McMaster University is developing a temperature sensor of this type as part of his M.A.Sc. research.

### Fiber Bragg Grating

A Fiber Bragg Grating (FBG) is simply a section of fiber, single mode in most cases, where there is a periodic refractive index variation, as shown in Fig. 1.9 by the darker sections of the fiber core. The grating section can be part of a longer fiber which can contain many FBG's. The ability to have many FBG's on a single fiber, along with the ability to multiplex signals, makes this system very robust and attractive for distributed sensor application.

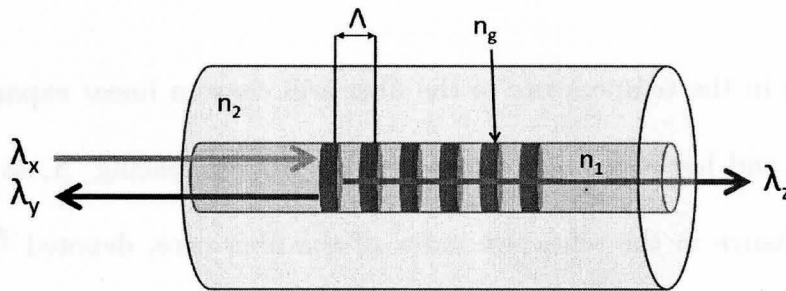


Figure 1.9: Fiber Bragg Grating

The operational principle of the FBG is periodic refractive index change shown as  $n_g$ , the grating spacing is given by  $\Lambda$ , and the index of the core is given by  $n_1$ . As a broadband signal,  $\lambda_x$ , is propagated along the core of the fiber, it will impinge in the periodic grating and as each individual index transition is met, there will be a small amount of reflection in the opposite

direction of propagation if the Bragg condition (equation 1.20) is met. The periodicity of the grating,  $\Lambda$  will cause a specific wavelength,  $\lambda_y$  to back-reflect, if the Bragg condition is met, in phase, and as a result a coherent signal will be reflected in the opposite direction of original propagation. The wavelength that is reflected will be specific to the given grating period and is known as the Bragg wavelength. The rest of the broadband signal will be transmitted through the fiber, and is shown as  $\lambda_z$ . However it should be noted that for Bragg gratings in waveguide structures  $\lambda = \lambda_o/N_{eff}$ .

$$\Lambda = \frac{m\lambda_o}{2N_{eff}} \quad (1.20)$$

where  $m$  is a positive integer that is representative of the order of the Bragg grating.

A change in the temperature of the fiber will cause a linear expansion in the fiber, and hence a small change in the grating spacing,  $\Lambda$ , as well as a small change in the refractive index of the fiber core, denoted  $\frac{dN_{eff}}{dT}$ . Due to a change in grating spacing, there is also a change in the Bragg wavelength,  $\Delta\lambda$ , which is proportional to the temperature change  $\Delta T$ , via the relationship expressed in equation 1.21, where  $K$  is the linear thermal expansion coefficient of the fiber and  $\frac{dN}{dT}$  is the thermo-optic coefficient of the fiber.

$$\Delta\lambda = \left( (K + \frac{dN}{dT}) \Delta T \right) \lambda \quad (1.21)$$

The output of a FBG at a constant temperature will resemble Fig. 1.10.

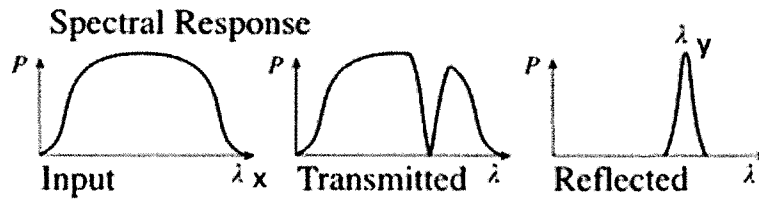


Figure 1.10: Output Spectrum of Fiber Bragg Grating at a Constant Temperature (Adapted from Encyclopedia of Laser Physics and Technology)

Either a broadband source or a tunable laser source could be used in this case. A broadband source will reflect a single wavelength, which corresponds to  $\lambda_y$  in Fig. 1.9 and the transmitted wavelengths,  $\lambda_z$ , as shown in Fig. 1.10 and Fig. 1.9. As a temperature sensor, thermal expansion and effective index changes due to temperature variation will cause a change in grating periodicity as stated by equation 1.20 and 1.21. As the temperature is changed the Bragg wavelength will also change in accordance to the grating periodicity, which will in turn shift the transmitted and reflected peaks. Various researchers have achieved sensitivity of 0.01nm peak shifts for 1 degree Celsius temperature changes [21, 22].

### 1.6.3 Prism Spectrometer

The prism spectrometer is based on the dispersion characteristics of a glass prism, whereby a source of light is collimated via a lens and directed through a prism. The collimated beam, upon exiting the prism will have diverged into its separate wavelength components based on dispersion. The incident beam, composed of various wavelengths, enters the prism at an angle and

upon entry is bent at an angle based on Snell's law. The degree of bending is dependant on the specific wavelengths which comprise the original signal. This causes wavelength components to be dispersed and will exit the prism at slightly different locations and at different angles. A simple example of this is the rainbow effect produced by a prism which is diffracting sunlight. The decomposed signal will exit the prism as a number of separate waves which will be spaced with a defined spectral deviation based on the geometry of the prism as well as point of measurement. When one collects the refracted signals, taking into account the beam separation, the spectral components of the initial beam can be determined.

The range of measurement is highly dependant on the absorption of the material one wishes to employ. For example, a prism made of quartz or SodaLime would be sufficient for determining the spectral composition of a light source in the visible region, though would not suffice for the IR regions. However, prisms composed of salts such as NaCl, KCl, and Al<sub>2</sub>O<sub>3</sub>, would be sufficient for the IR spectrum [2, pg120].



## Chapter 2

---

# Theory

---

The operational basis of this sensor is the capacity for successful transportation of an optical signal via a rib waveguide as discussed in the introduction to Chapter 1. In order for coherent light to propagate with as little attenuation as possible, the optical and physical characteristics of the rib waveguide are of great concern. Phenomena such as mode characteristics, dispersion, and loss need to be taken into account when fabricating a waveguide device. In the case of this particular sensor, a MZI is implemented, and in order to operate appropriately the waveguides must be single mode to avoid interference problems. Path length differences in the MZI will give way to thermal and mechanical sensitivity in a predictable and measurable manner via dispersion and the photoelastic effect.

The aim of this chapter is to review electromagnetic theory with relation to the propagation of light through crystalline silicon. The theory will then

be extended to more complex systems in order to gain an appreciation of the operational principles of the sensor. The purpose is to produce a lucid mathematical understanding of the operational principles that govern this particular sensor. Topics such as single mode propagation in Silicon-on-Insulator (SOI) rib waveguides, bend loss, photoelastic effect with relation to stress and strain, and polarization dependence will be discussed in this chapter.

## 2.1 Electromagnetic Wave Propagation

Coherent light propagation through media is governed by the well known Maxwell's equations, which describe electromagnetic phenomena. Maxwell's equations are listed as equations 2.1 to 2.4, where  $\mathbf{E}[\frac{V}{m}]$  is the electric field vector,  $\mathbf{H}[\frac{A}{m}]$  is the magnetic field vector,  $\mathbf{D}[\frac{C}{m^2}]$  is the electric displacement, and  $\mathbf{B}[\frac{W}{m^2}]$  is the magnetic displacement. Though, in the case of optical waveguides the medium contains no charge density,  $\rho$ , nor current density,  $\mathbf{J}$ , thus both are set to 0. The electric displacement,  $\mathbf{D}$ , can be further defined in terms of permittivity in a vacuum, electric polarization  $\mathbf{P}$ , and the electric field vector  $\mathbf{E}$ , as  $\mathbf{D} = \epsilon_o\mathbf{E} + \mathbf{P}$ . Furthermore, the magnetic displacement  $\mathbf{B}$  can be described in terms of the permeability of a vacuum, the magnetic field vector  $\mathbf{H}$ , and the magnetic polarization  $\mathbf{M}$  as  $\mathbf{B} = \mu_o[\mathbf{H} + \mathbf{M}]$ . However, in the case of passive optical waveguides the

material has no magnetic polarizability, thus  $\mathbf{M}$  can be set to 0.

$$\nabla \times \mathbf{E} + \frac{\partial \mathbf{B}}{\partial t} = 0 \quad (2.1) \quad \nabla \times \mathbf{H} - \frac{\partial \mathbf{D}}{\partial t} = \mathbf{J} \quad (2.2)$$

$$\nabla \cdot \mathbf{D} = \rho \quad (2.3) \quad \nabla \cdot \mathbf{B} = 0 \quad (2.4)$$

Utilizing Maxwell's equations, one can readily develop the wave equation for monochromatic coherent light propagation in a medium where current density and charge density are 0, such as silicon. The propagation of light in a rib waveguide structure is further broken down into the transverse electric field (TE-polarization), and transverse magnetic field (TM-polarization). Wave equations for the following plane waves will be brought about and developed via Maxwell's equations.

### The Wave Equation

Assuming  $\mathbf{M}=0$ , the magnetic displacement simply becomes  $\mathbf{B} = \mu_o \mathbf{H}$ , and equation 2.1 becomes equation 2.5.

$$\nabla \times \mathbf{E} + \mu_o \frac{\partial \mathbf{H}}{\partial t} = 0 \quad (2.5)$$

Applying the Curl operator to equation 2.5 and dividing by  $\mu$  will result in equation 2.6

$$\nabla \times \left( \frac{1}{\mu} \nabla \times \mathbf{E} \right) + \frac{\partial}{\partial t} (\nabla \times \mathbf{H}) = 0 \quad (2.6)$$

Differentiating 2.2 with respect to time, with current density set to 0 and replacing  $\frac{\partial}{\partial t}(\nabla \times \mathbf{H})$  from equation 2.6 will result in the following relation; equation 2.7

$$\nabla \times \left( \frac{1}{\mu} \nabla \times \mathbf{E} \right) - \frac{\partial^2 \mathbf{D}}{\partial t^2} = 0 \quad (2.7)$$

The governing equation for electric displacement without the polarization component,  $\mu \mathbf{E}$ , will replace  $\mathbf{D}$  from equation 2.7 and give the following;

$$\nabla \times \left( \frac{1}{\mu} \nabla \times \mathbf{E} \right) - \epsilon \frac{\partial^2 \mathbf{E}}{\partial t^2} = 0 \quad (2.8)$$

Since  $\mu = \mu_o$ , which is equal to a constant the term,  $\nabla \frac{1}{\mu}$  vanishes and we are left with.

$$\nabla(\nabla \cdot \mathbf{E}) - \mu \epsilon \frac{\partial^2 \mathbf{E}}{\partial t^2} + (\nabla \ln \mu) \times (\nabla \times \mathbf{E}) - \nabla(\nabla \cdot \mathbf{E}) = 0 \quad (2.9)$$

Using vector identities and remembering that silicon is a homogeneous isotropic material, the wave equation for the electric field will become the following [23].

$$\nabla^2 \mathbf{E}(\mathbf{r}, t) - \mu \epsilon \frac{\partial^2 \mathbf{E}(\mathbf{r}, t)}{\partial t^2} = 0 \quad (2.10)$$

Following a similar line of reasoning for the magnetic field gives,

$$\nabla^2 \mathbf{H}(\mathbf{r}, t) - \mu \epsilon \frac{\partial^2 \mathbf{H}(\mathbf{r}, t)}{\partial t^2} = 0 \quad (2.11)$$

### 2.1.1 Plane Waves

The monochromatic plane wave,

$$\Psi = A \exp i(\mathbf{k} \cdot \mathbf{r} - \omega t) \quad (2.12)$$

will satisfy the electromagnetic wave equations 2.10 and 2.11, where  $A$  is the amplitude of the wave. The magnitude of the propagation vector  $\mathbf{k}$ , also known as the propagation constant, is related to the angular frequency  $\omega$  via equation 2.13. In most cases the system will be described in Cartesian coordinates, in which case  $\mathbf{r}$  can be conveniently described as  $(x, y, z)$ .

$$|\mathbf{k}| = \omega \sqrt{\mu\epsilon} \quad (2.13)$$

Specific forms of this equation, which is time and space dependant, will be of more use with consideration to the electromagnetic wave equations, which are;

$$\mathbf{E}(\mathbf{r}, t) = \mathbf{E}_o(\mathbf{r}, t) \exp i(\mathbf{k} \cdot \mathbf{r} - \omega t) \quad (2.14)$$

$$\mathbf{H}(\mathbf{r}, t) = \mathbf{H}_o(\mathbf{r}, t) \exp i(\mathbf{k} \cdot \mathbf{r} - \omega t) \quad (2.15)$$

which in Cartesian coordinates will take the form;

$$\mathbf{E}(x, y, z, t) = \mathbf{E}_o(x, y, z, t) \exp i(\mathbf{k} \cdot \mathbf{r} - \omega t) \quad (2.16)$$

$$\mathbf{H}(x, y, z, t) = \mathbf{H}_o(x, y, z, t) \exp i(\mathbf{k} \cdot \mathbf{r} - \omega t) \quad (2.17)$$

In this form, the wave equations have amplitude functions, defined as  $\mathbf{E}_o(\mathbf{r}, t)$  and  $\mathbf{H}_o(\mathbf{r}, t)$ , for the electric field and magnetic field respectively.

By putting equations 2.14 and 2.15 back into Maxwell's curl equations along with the aid of the constituent equations for  $\mathbf{D}$  and  $\mathbf{B}$ , equations can be found that relate the electric and magnetic fields in a homogeneous, isotropic dielectric medium. The solutions, equations 2.18 and 2.19, describe the nature of coupling between the  $\mathbf{E}$  and  $\mathbf{H}$  fields. These equations show that  $\mathbf{E}$  and  $\mathbf{H}$  are orthogonal to each other, while both are orthogonal to the propagation vector  $\mathbf{k}$ . Furthermore, this indicates that as the electric and magnetic fields propagate, they are oriented perpendicular to the direction of propagation and remain at a normal angle with respect to each other.

$$\mathbf{k} \times \mathbf{E} = \omega\mu\mathbf{H} \quad (2.18)$$

$$\mathbf{k} \times \mathbf{H} = -\omega\epsilon\mathbf{E} \quad (2.19)$$

### 2.1.2 Plane Waves at an Interface

An inherent and unavoidable issue when dealing with layered media is the interaction of light with the interfaces of the various regions. The reflection and refraction of monochromatic plane waves at dielectric boundaries between homogeneous isotropic media brings about various problems [23].

The simple problem of reflection and refraction at a boundary is a well known and documented problem. In general, an incident wave will be split into a transmitted and reflected wave when a medium boundary is met.

As the incident beam meets the boundary, a portion will be transmitted into the second medium, while a portion will be reflected back into the first medium. Also, the initial power of the incident wave will be equal to the sum of the reflected and transmitted wave if it is assumed that the mediums are not lossy.

For non-normal incidence, the various angles involved with the reflected and transmitted wave are directly related to the refractive indices of the two media as well as the angle of incidence by;  $n_1 \sin(\theta_i) = n_1 \sin(\theta_r) = n_2 \sin(\theta_t)$ . This relation states that the angle of incidence is equal to the angle of reflection, and gives the elegant relation known as Snell's Law, represented in equation 2.20.

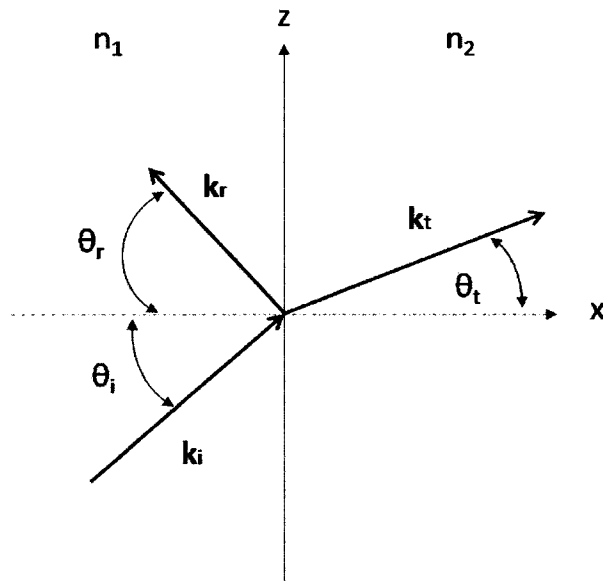


Figure 2.1: Reflection and Refraction of Plane Wave at Refractive Index Boundary

$$\frac{\sin(\theta_i)}{\sin(\theta_t)} = \frac{n_2}{n_1} \quad (2.20)$$

An important extrapolation of Snell's Law is the definition of the critical angle,  $\theta_c$ , which is the smallest angle at which there will be complete reflection, and no transmission. To determine this the transmitted angle,  $\theta_t$  must be set to  $90^\circ$ , for at  $90^\circ$ , there will be no transmitted wave into the second medium. However, in order for  $\theta_t$  to be  $90^\circ$ , the transmitted angle will need to have a specific value, which is deemed the critical angle,  $\theta_c$ . Snell's Law can be rearranged, as shown in equation 2.21, to determine the critical angle for total internal reflection (TIR). Total internal reflection further comes into play when one deals with various waveguide structures, for without TIR confinement could not be achieved, and hence light propagation in any practical manner would be futile.

$$\sin(\theta_c) = \frac{n_2}{n_1} \quad (2.21)$$

There is also a polarization dependence to the reflection and refraction of a plane wave at a dielectric boundary. Describing the reflection, specific to polarization, are the Fresnel formulae, given by equations 2.22 and 2.23.

$$r_{TE} = \frac{n_1 \cos(\theta_i) - n_2 \cos(\theta_t)}{n_1 \cos(\theta_i) + n_2 \cos(\theta_t)} \quad (2.22)$$

$$r_{TM} = \frac{n_2 \cos(\theta_i) - n_1 \cos(\theta_t)}{n_2 \cos(\theta_i) + n_1 \cos(\theta_t)} \quad (2.23)$$

Using Snell's law, the Fresnel formulae can be re-composed as follows;

$$r_{TE} = \frac{n_1 \cos(\theta_i) - \sqrt{n_2^2 - n_1^2 \sin^2(\theta_i)}}{n_1 \cos(\theta_i) + \sqrt{n_2^2 - n_1^2 \sin^2(\theta_i)}} \quad (2.24)$$

$$r_{TM} = \frac{n_2 \cos(\theta_i) - \sqrt{n_2^2 - n_1^2 \sin^2(\theta_i)}}{n_2 \cos(\theta_i) + \sqrt{n_2^2 - n_1^2 \sin^2(\theta_i)}} \quad (2.25)$$

The transmission, assuming that the media are lossless, can be found via  $1 = T + R$ , which states that the transmitted power and reflected power are equal to the incident power. In the case of the Fresnel formulae, the reflection coefficient,  $r$ , is given by the ratio  $\frac{E_r}{E_i}$  and the reflectance is given as  $R = r^2$ .

When the critical angle is exceeded, and the condition for TIR is met, the value found under the root sign in equations 2.24 or 2.25 will become negative, and hence the reflection coefficient is complex with magnitude 1. If the reflection coefficient is complex, a phase shift,  $\phi$ , will result for the reflected wave, as given by equations 2.26 and 2.27.

$$\phi_{TE} = 2 \arctan \left( \frac{\sqrt{\sin^2(\theta_i) - \left(\frac{n_2}{n_1}\right)^2}}{\cos(\theta_1)} \right) \quad (2.26)$$

$$\phi_{TE} = 2 \arctan \left( \frac{\sqrt{\frac{n_1^2}{n_2^2} \sin^2(\theta_i) - 1}}{\frac{n_2}{n_1} \cos(\theta_1)} \right) \quad (2.27)$$

However, if the incident angle,  $\theta_i$  is less than the critical angle, there will only be fractional reflection, and the reflection coefficient will be real, with a phase shift of either zero or  $\pi$ .

## 2.2 Plane Waves in an Asymmetric Slab Waveguide

The asymmetric slab waveguide is more complex than the symmetric slab waveguide and of great practical use when analyzing light propagation through media. Although the actual geometry employed in this research is a rib waveguide, the analysis of a slab waveguide is useful for practical purposes and important in developing the modal propagation in a rib waveguide. The slab itself consists of a region of high refractive index surrounded by two regions of lower refractive index, though each surrounding region can have different dielectric constants, as shown in Fig. 2.2. It is this difference in refractive index that allows for confinement of the propagating wave to a desired layer. In order for a lightwave to be confined, the index of the film must be greater than that of the surrounding region, ( $n_{air} \leq n_{substrate} \leq n_{film}$ ), which is necessary for total internal reflection, as described in section 2.1.2.

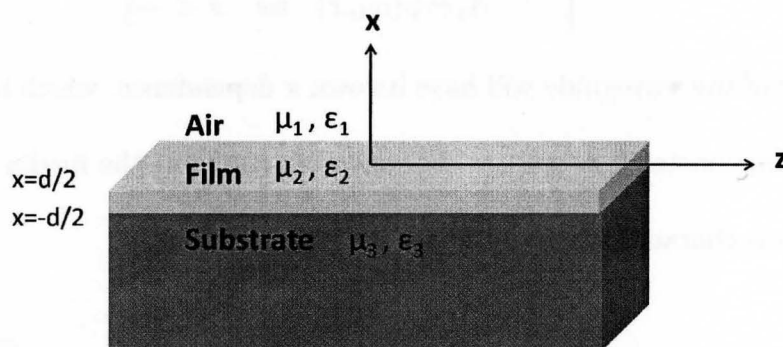


Figure 2.2: Asymmetric Slab Waveguide

In order to obtain useful information based on dimensions as well as ma-

material properties of the slab waveguide, one must adapt the plane wave equations 2.14 and 2.15 for appropriate light propagation within the waveguide. The adaptations take into account the behavior of the propagating mode in the various regions of the slab. In order to properly develop modal equations for the given system, one must treat the TE and TM modes separately.

### TE Modes

The TE mode will not have an even nor odd solution due to the asymmetry of the system, however, one can assume that the modal field takes the form as presented in 2.28, where  $A_x$  is an amplitude constant. Also, given the choice of coordinates, the waveguide mode solution will be independent of  $y$ , which in turn causes  $\frac{\partial}{\partial y} = 0$ .

$$\mathbf{E}_y(x, z) = \exp(-i\beta z) \begin{cases} A_1 \exp(-\alpha_{1x}x) & \text{for } x > \frac{d}{2} \\ A_2 \cos(k_{2x}x + \psi) & \text{for } |x| \leq \frac{d}{2} \\ A_3 \exp(\alpha_{3x}x) & \text{for } x < -\frac{d}{2} \end{cases} \quad (2.28)$$

Each layer of the waveguide will have its own  $x$  dependence, which takes the propagation constant, as well as dielectric constants of the media into account. This is characterized as follows,

$$\alpha_{1x} = \sqrt{\beta^2 - \omega^2 \mu_1 \epsilon_1} \quad (2.29)$$

$$\alpha_{3x} = \sqrt{\beta^2 - \omega^2 \mu_3 \epsilon_3} \quad (2.30)$$

$$k_{2x} = \sqrt{\omega^2 \mu_2 \epsilon_2 - \beta^2} \quad (2.31)$$

The  $\mathbf{H}$  component for the TE mode can be found via alteration of Maxwell's curl equation 2.2, which will take the form;

$$\mathbf{H}_z(x, z) = i \frac{1}{\omega \mu} \frac{\partial}{\partial x} \mathbf{E}_y(x, z) \quad (2.32)$$

Inputting the appropriate forms of equations 2.28 into equation 2.32, and taking the differential of  $\mathbf{E}_y(x, z)$ , one can find the equations that govern the behavior of the  $\mathbf{H}$  component of the TE mode, noted as equations 2.33.

$$\mathbf{H}_z(x, z) = \exp(-i\beta z) \begin{cases} -\frac{i\alpha_{1x}}{\omega\mu_1} A_1 \exp(-\alpha_{1x}x) & \text{for } x > \frac{d}{2} \\ -\frac{ik_{2x}}{\omega\mu_2} A_2 \sin(k_{2x}x + \psi) & \text{for } |x| \leq \frac{d}{2} \\ \frac{i\alpha_{3x}}{\omega\mu_3} A_3 \exp(\alpha_{3x}x) & \text{for } x < -\frac{d}{2} \end{cases} \quad (2.33)$$

Applying the boundary conditions at the air-film interface,  $x = \frac{d}{2}$  for  $\mathbf{E}$  and  $\mathbf{H}$ , will give tangential values for the electric and magnetic components, as shown in equations 2.34 and 2.34, respectively.

$$A_1 \exp\left(-\alpha_{1x} \frac{d}{2}\right) = A_2 \cos\left(k_{2x} \frac{d}{2} + \psi\right) \quad (2.34)$$

$$A_1 \exp\left(-\alpha_{1x} \frac{d}{2}\right) = \frac{\mu_1 k_{2x}}{\mu_2 \alpha_{1x}} A_2 \sin\left(k_{2x} \frac{d}{2} + \psi\right) \quad (2.35)$$

Ratioing 2.34 and 2.35 to eliminate  $A_1$ , will give forth to  $A_2$ , producing the following relationship;

$$\tan\left(k_{2x} \frac{d}{2} + \psi\right) = \frac{\mu_2 \alpha_{1x}}{\mu_1 k_{2x}} \quad (2.36)$$

By applying boundary conditions at the film-substrate interface, where  $d =$

$-\frac{d}{2}$  will yield the following ratio condition;

$$\tan\left(k_{2x}\frac{d}{2} - \psi\right) = \frac{\mu_2\alpha_{3x}}{\mu_3k_{2x}} \quad (2.37)$$

Utilizing the well known tangential identity,  $\tan x = \tan(x \pm n\pi)$ , equations 2.36 and 2.37, can be re-written as follows;

$$k_{2x}\frac{d}{2} + \psi = \frac{1}{2}\sigma_1^{TE} \pm n\pi \quad (2.38)$$

$$k_{2x}\frac{d}{2} - \psi = \frac{1}{2}\sigma_3^{TE} \pm m\pi \quad (2.39)$$

Where,

$$\sigma_1^{TE} = 2 \arctan\left(\frac{\mu_2\alpha_{1x}}{\mu_1k_{2x}}\right) \quad (2.40)$$

$$\sigma_3^{TE} = 2 \arctan\left(\frac{\mu_2\alpha_{3x}}{\mu_3k_{2x}}\right) \quad (2.41)$$

The sum of equations 2.38 and 2.39 will cause the  $\psi$  term to fall out, and will leave a relation, equation 2.42, that governs the guidance condition of the TE mode in an asymmetric slab waveguide, where  $p$  can be any positive integer that describes the particular mode of interest. Once the solution to a particular mode has been found, the field in that region can be solved via boundary conditions of the tangential  $\mathbf{E}$  field as described in equation 2.34. The final outcome of the TE mode fields for the various regions, such as the

substrate, film, or air cladding, is given by the array equation 2.43

$$2k_{2x}d - \sigma_1^{TE} - \sigma_3^{TE} = 2p\pi \quad (2.42)$$

$$\mathbf{E}_y(x, z) = A_2 \exp(-i\beta z) \begin{cases} \cos(k_{2x}\frac{d}{2} + \psi) \exp(-\alpha_{1x}(x - \frac{d}{2})) & \text{for } x > \frac{d}{2} \\ \cos(k_{2x}x + \psi) & \text{for } |x| \leq \frac{d}{2} \\ \cos(k_{2x}\frac{d}{2} - \psi) \exp(-\alpha_{xx}(x - \frac{d}{2})) & \text{for } x < -\frac{d}{2} \end{cases} \quad (2.43)$$

### TM Modes

In the same manner as described above, the TM mode is solved via setting boundary conditions and solving in order to obtain an equation for the waveguide guidance. Upon solving for the guidance condition, the TM mode propagating in a slab waveguide will follow from the array equation 2.44

$$\mathbf{H}_y(x, z) = A_2 \exp(-i\beta z) \begin{cases} \cos(k_{2x}\frac{d}{2} + \psi') \exp(-\alpha_{1x}(x - \frac{d}{2})) & \text{for } x > \frac{d}{2} \\ \cos(k_{2x}x + \psi') & \text{for } |x| \leq \frac{d}{2} \\ \cos(k_{2x}\frac{d}{2} - \psi') \exp(-\alpha_{xx}(x - \frac{d}{2})) & \text{for } x < -\frac{d}{2} \end{cases} \quad (2.44)$$

## 2.3 Rib Waveguides

The rib waveguide structure, as shown in Fig. 2.3 is widely used to confine light in two dimensions. The simple asymmetric slab waveguide has high confinement in the perpendicular direction due to the difference in refractive index in the material layers, but no confinement in the horizontal direction. Due to the lack of confinement in the horizontal direction, slab waveguide mode solutions are not adequate when bends need to be implemented, or for more complicated manipulation of coherent light. However, the rib waveguide has high confinement in the perpendicular direction due to the various material layers, and there is also confinement in the horizontal direction due to the effective index variation, which is caused by slab height difference and will be described later in section 2.3.2. However, the modal shape as well as propagation characteristics are more complicated due to the rib formation, and analytical models via electromagnetic beam propagation software, namely BeamPROP were used.

The geometry of the rib is such that the height of the rib is  $H$ , the slab height is  $h$ , and the rib width is  $W$ . Depending on the dimensions of  $H, h$ , and  $W$  the waveguide may be single or multi-mode [24]. In the case of interferometers the waveguide must be single mode.

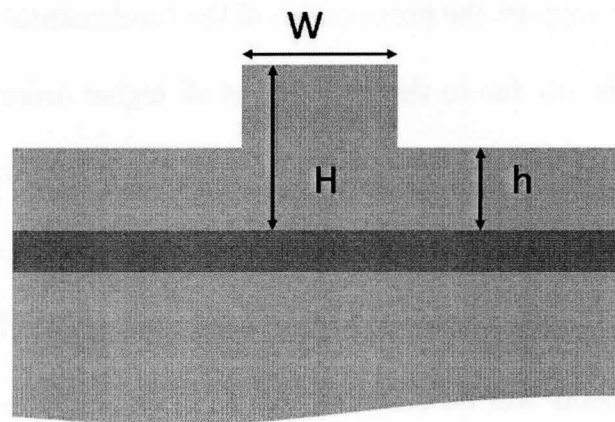


Figure 2.3: Rib Waveguide Cross Section

### 2.3.1 Single Mode Condition

Single mode propagation is essential in the telecommunications industry, for it allows long haul signal transmission with minimal pulse broadening. Optical rib waveguides are most often implemented via fiber optic input and output in an industrial setting. Interferometers must be single mode, therefore one must design the waveguide in a manner that ensures the single mode condition used by the fibers themselves is held throughout the device. Furthermore, the fundamental mode is the least lossy of all modes, and is the most stable.

The term single mode, is slightly ambiguous, as specific rib waveguide geometry is not necessarily single mode. If geometry is chosen wisely, the fundamental mode will encounter negligible losses due to the geometry of the waveguide, though higher order modes will suffer from very high losses in comparison. From an engineering standpoint, this means that certain rib

geometries will only support the propagation of the fundamental mode after a distance of straight rib due to the high loss of all higher order modes.

The geometry itself has been determined for Reactive Ion Etched (RIE) ribs, which have vertical sidewalls, as well as chemically etched ribs, which will have angled sidewalls. Since RIE has been utilized for fabrication, the following arguments will be based on this form of geometry. Based on the Beam Propagation Method (BPM) and Effective Index Method (EIM), a well known formula, equation 2.45, has been devised, which takes into account the various dimensions of a rib waveguide, as shown in Fig. 2.3 [25, 26, 24, 27]. However, the work by *Powell et al.* [24] was done mainly with wet etched silicon rib guides. Anisotropic wet etching causes the sidewalls to be angled. The work composed by Soref, Pogossian, and Lousteau was done with silicon ribs, which had vertical sidewalls, and the following arguments are based on this geometry. The variables  $W$ ,  $H$ , and  $h$  are dimensions of the various regions of the waveguide cross-section, shown in Fig. 2.3.  $\alpha$  is a matching constant and had been defined to be 0.3 by *Soref et al.* [25], to be 0 via EIM, and  $-0.05$  by *Pogossian et al.* [26], as shown in Fig. 2.4. However, an additional expectation for the single mode condition was proposed by *Soref et al.*, and is expressed in equation 2.46, whereby a mode with at least two vertical maxima will inherently be leaky due to coupling with the fundamental mode in the surrounding slab [25]. As an addition, *Lousteau et al.* have completed some excellent work, which helps

to determine specific geometries within the single mode region, which are most lossy to higher order modes, and hence least lossy to the fundamental.

$$\frac{W}{H} \leq \alpha + \frac{\frac{h}{H}}{\sqrt{1 - (\frac{h}{H})^2}} \quad (2.45)$$

$$\frac{h}{H} \geq 0.5 \quad (2.46)$$

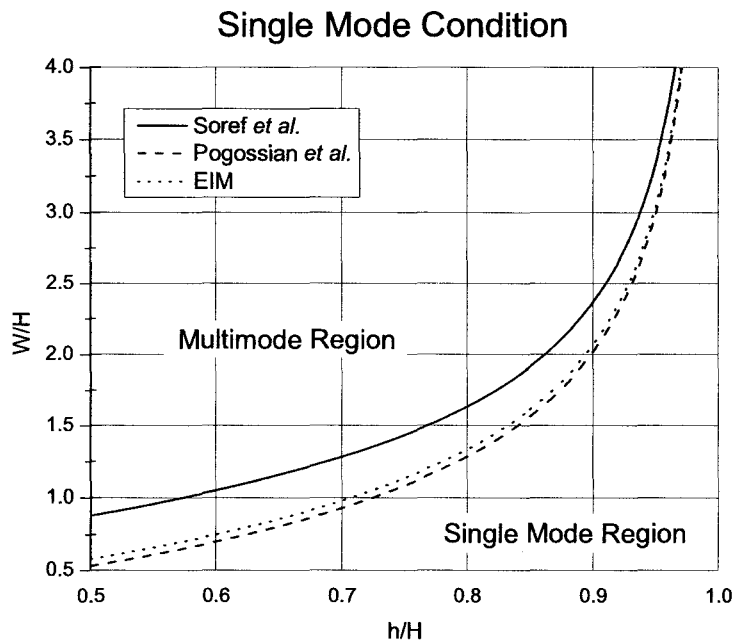


Figure 2.4: Single Mode Condition for Various  $\alpha$  Constants

However, *Pogossian et al.* have further developed a manner to which the single mode condition for rib geometry is met. Pogossian proposed that the effective dimensions of the rib be found. In using this method, precision is better and propagation constants are taken into account. The effective dimensions used to find the single mode condition are proposed by

*Pogossian et al.* as follows,

$$\begin{aligned}
 H_{eff} &= H + q \\
 h_{eff} &= h + q \\
 W_{eff} &= W + 2 \frac{\gamma_c}{k_o(n_f^2 - n_c^2)^{\frac{1}{2}}} \\
 q &= \frac{\gamma_c}{k_o(n_f^2 - n_c^2)^{\frac{1}{2}}} + \frac{\gamma_s}{k_o(n_f^2 - n_s^2)^{\frac{1}{2}}}
 \end{aligned} \tag{2.47}$$

where  $k_o$  is the propagation constant  $\frac{2\pi}{\lambda}$ , and  $n_s$ ,  $n_f$ , and  $n_c$  are the indices of the substrate, film, and cover, respectively. Also,  $\gamma_{c,s}$  for TE modes is equal to one, while  $\gamma_c = (\frac{n_c}{n_f})^2$  and  $\gamma_s = (\frac{n_s}{n_f})^2$  for TM modes. By implementing these values in equations 2.45 and 2.46 it is possible to obtain a more accurate expression for the single mode rib waveguide dimensions. The optimized relationship for rib dimensions for successful fundamental mode propagation will take the form;

$$\frac{W_{eff}}{H_{eff}} \leq \alpha + \frac{\frac{h_{eff}}{H_{eff}}}{\sqrt{1 - (\frac{h_{eff}}{H_{eff}})^2}} \tag{2.48}$$

$$\frac{h_{eff}}{H_{eff}} \geq 0.5 \tag{2.49}$$

### 2.3.2 Effective Index Method

The effective index of a rib waveguide is an important variable in that it is used to determine bend losses, as well as propagation characteristics of the waveguide itself. The effective index method(EIM) allows one to analyze

a two dimensional waveguide structure by breaking the problem down into two separate one dimensional problems and repeating the analysis. The basis of analysis is to solve the waveguide equation in one direction, then in the other, though care must be taken for rib waveguides, for polarization must be taken into consideration. The refractive index of bulk material at a given wavelength has previously been explained in section 1.2, though when dealing with dimensions that are near those of the wavelength being used, the dimensions appear to the propagating light to be slightly different from the actual physical dimensions. The relationship between the propagation constant,  $\beta$ , and the effective index,  $n_{eff}$ , of a mode is defined as,

$$\beta = n_{eff}k_o \quad (2.50)$$

The effective index is found by solving the following scalar wave equation [28].

$$\frac{\partial^2 \phi(x, y)}{\partial x^2} + \frac{\partial^2 \phi(x, y)}{\partial y^2} + k_o^2 (\epsilon_r(x, y) - n_{eff}^2) \phi(x, y) = 0 \quad (2.51)$$

Once  $n_{eff}$  is determined, the mode shapes (in one dimension) are given by equations 2.28 or 2.44. However, equation 2.51 is cumbersome to solve so the effective index method is used to find approximate solutions for the two dimensional mode shape, based on two one-dimensional solutions.

The EIM is an approximate method for dealing equations 2.51. In a more graphical sense, one can view the EIM as finding the effective index across the cross section of the various regions, denoted I, II, and III, of the rib waveguide geometry, as shown in Fig. 2.5. After this, one can take the corresponding indices,  $n_{eff1}$ ,  $n_{eff2}$ , and  $n_{eff3}$ , and apply them to the slab in a topographical manner, as shown in Fig. 2.6.

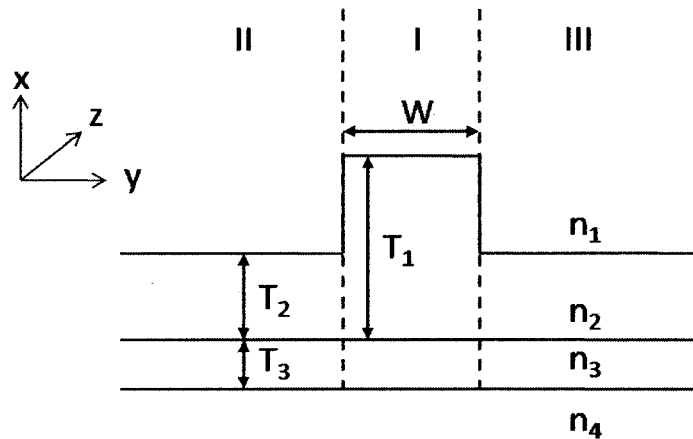


Figure 2.5: Effective Index Method: Cross Sectional Analysis

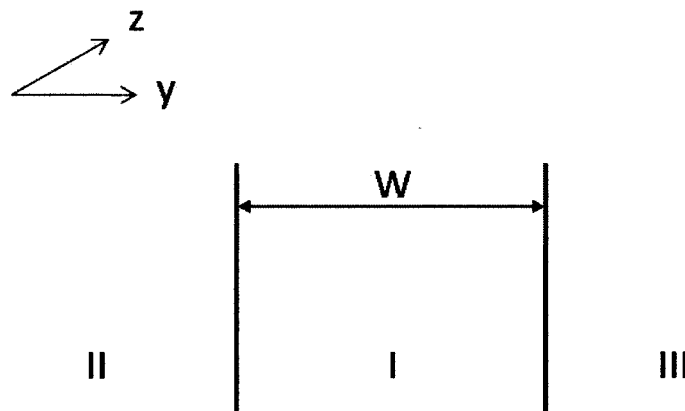


Figure 2.6: Effective Index Method: Topographical Analysis

However, one must assume that there is no interaction between the x

and  $y$  variables, which would correspond to the TE and TM modes, which from section 2.1 has been shown otherwise. Though, for the purpose of this argument, the assumption is valid. Separating the above wave equation into two functions,  $\phi(x, y) = f(x) \cdot g(y)$ , and substituting the separated wave function back into equation 2.51, results in;

$$\frac{\partial^2(f(x) \cdot g(y))}{\partial x^2} + \frac{\partial^2(f(x) \cdot g(y))}{\partial y^2} + k_o^2 (\epsilon_r(x, y) - n_{eff}^2) f(x) \cdot g(y) = 0 \quad (2.52)$$

now, we divide equation 2.52 by  $f(x) \cdot g(y)$ , which yields the following.

$$\frac{1}{f(x)} \frac{\partial^2 f(x)}{\partial x^2} + \frac{1}{g(y)} \frac{\partial^2 g(y)}{\partial y^2} + k_o^2 (\epsilon_r(x, y) - n_{eff}^2) = 0 \quad (2.53)$$

Forcing the sum of the second and third terms to be equal to  $k_o^2 N^2(x)$  gives,

$$\frac{1}{g(y)} \frac{d^2 g(y)}{dy^2} + k_o^2 \epsilon_r(x, y) = k_o^2 N^2(x) \quad (2.54)$$

which would cause the sum of the first and last term to be equal to,

$$\frac{1}{f(x)} \frac{d^2 f(x)}{dx^2} + k_o^2 n_{eff}^2 = -k_o^2 N^2(x) \quad (2.55)$$

In this manner, two independent equations come forth, which allow for the calculation of the various effective indices over the cross section, as well as the overall index over the topographical via the use of equations 2.56 and 2.57.

$$\frac{d^2 f(x)}{dx^2} + k_o^2 [N^2(x) - n_{eff}^2] f(x) = 0 \quad (2.56)$$

$$\frac{d^2g(y)}{dy^2} + k_o^2[\epsilon_r(x, y) - N^2(x)]g(y) = 0 \quad (2.57)$$

A more simplified and less mathematically rigorous manner in which the effective indices can be found, has been presented by [29]. *Yuanyuan et al.* modifies the EIM, though it is simplified and compacted to a single equation, as shown below.

$$N_j^2 = n_2^2 - \frac{\pi^2}{\frac{2\pi d_j}{\lambda} + 2(n_2^2 - n_3^2)^{\frac{1}{2}}} \quad (2.58)$$

$$d_j = \begin{cases} T_1 & \text{for Sections I} \\ T_2 & \text{for Sections II, III} \end{cases} \quad (2.59)$$

where  $T_1$  and  $T_2$  are the heights of the rib and slab regions respectively. To use this method, equation 2.58 is implemented to find the effective indices of regions I, II, and III, from a cross sectioned standpoint. Then those indices are put back into equation 2.58 to determine an overall effective index,  $N_{eff}$ , across the rib. The variables  $n_2$  and  $n_3$  correspond to the refractive indices of silicon and silicon dioxide, respectively, and  $\lambda$  is the free space wavelength.

### 2.3.3 Losses in SOI Rib Waveguides

In the industrial world, silicon photonics processing has been developed to the point where SOI rib waveguides can have propagation losses as low as 0.1dB/cm. However, achieving such a low loss requires careful geometry choice and processing techniques.

There are three major contributing factors that will cause an optical waveguide to suffer from loss: scattering, absorption, and radiation [30]. Of these three, the greatest loss, based on simple SOI waveguides, will come from scattering and radiation, as the operational wavelength is well beyond the bandedge wavelength of 1100nm. In the case of scattering, the main factor contributing to the loss is slab and sidewall roughness. Slab and sidewall roughness on rib waveguides is often caused during the reactive ion etching (RIE) process. Depending on the RIE process, the surface and sidewall roughness can be minimal or devastating, though in most cases, the chemical recipe has been perfected to solve this problem. In the case of radiation, a straight waveguide should exhibit very little loss due to radiation. However, when bends or splitting of waveguides is needed for device design, radiation loss is no longer negligible, though it can be minimized with appropriate design choices.

### **Splitting Loss in Rib Waveguides**

A Y-branch is a simple waveguide formation that allows for a signal propagating in a waveguide to be split into two separate waveguides. A splitting branch can take on two forms: straight arm splitting or s-bend splitting, depending on the device requirement. In either case, the main purpose of the split is to transmit power into both arms with an equal splitting ratio and as little loss as possible. In an ideal case, the splitter would be symmetrical,

and thus the power ratio between the two branches would be 50/50.

In the region of the splitter from the point where the split initiates to the point where two separate guides diverge, the width of the region can be up to twice the width of the initial single waveguide. Due to this greater width, higher order modes can be excited. If one looks at this as an energy system, the fundamental mode meets the splitting region, at this point some of the energy from the fundamental is used in exciting higher order modes. The higher order modes will propagate in the splitting region along with the fundamental, until the point of guide divergence. After the guides diverge, and are of original width, the higher order modes suffer from high loss due to the single mode geometry of the waveguides, as intentionally set up. The fundamental is then able to propagate along each of the branches. The power lost by the fundamental, in exciting the higher order modes is lost with the attenuation of the higher order modes upon guide divergence, and is not converted back to the fundamental. Because of this, the splitting region will have an inherent loss that is controllable, though not extinguishable. An in depth analysis of losses caused by splitting can be found in [31, p36-39], and will not be discussed in depth.

In parallel with splitting, there is also the problem of dissimilar modal fields when a straight segment of waveguide couples to a bent segment, as in the case of a straight bend, or in the case of an s-bend, known as transitional losses. The transitional loss is due to a change in the mode shape when there

is a variation in the radius of the two waveguides. The modal symmetry, which exists in a straight waveguide, is broken upon entrance into a curved waveguide. If the transition from straight segment to an angled or curved segment has no reflections, the losses due to the transition can be estimated by the logarithm of the overlap integral formed by the mode fields in the straight and bent waveguides. The overlap integral is as follows [32];

$$\langle \psi_B, \psi_S \rangle = \frac{1}{2} \int_A \int (\mathbf{E}_S \times \mathbf{H}_B^* + \mathbf{E}_B^* \times \mathbf{H}_S) \cdot \mathbf{z} dA \quad (2.60)$$

where B denotes the bent segment, and S the straight segment with regards to the electric and magnetic modal fields  $\mathbf{E}$  and  $\mathbf{H}$  respectively, and the '\*' denotes the conjugate. A is the cross section of the waveguide. The loss, in dB, is found via the following logarithm of the normalized overlap integral [32].

$$L_T[dB] = -10 \log_{10} \frac{|\langle \psi_B, \psi_S \rangle|^2}{|\langle \psi_B, \psi_B \rangle| |\langle \psi_S, \psi_S \rangle|} \quad (2.61)$$

An approximate approach used to find the transitional loss from a straight waveguide to a curved waveguide is as follows [33],

$$L_{T-R} = \exp \left( \frac{-a^2}{2\omega_o^2} \left( 1 + \frac{(k_o N_{eff} \omega_o)^2 a}{2R} \right)^2 \right) \frac{1}{1 + \frac{(k_o N_{eff} \omega_o)^4 \omega_o^2}{2R^2}} \quad (2.62)$$

where,  $\omega_o$  is the modal width, a is the lateral offset, and R is the radius of curvature.

### **Bend Loss of Rib Waveguides**

Waveguide devices often require bends, and in the case of a MZI, it is the bends that form the actual operational component of the device. If we assume the initial direction of propagation to be along the z-axis, the propagating wave travels along the bend of defined radius,  $R$ , the modal shape will become off-center, and thus the symmetry is broken. Also, the modal profile is not completely contained within in the confine of the rib as there is a portion of the propagating mode that resides in the slab region, noted at the evanescent portion of the mode. Upon meeting a curve, the mode will shift towards the outside of the curved portion of the waveguide. Since the mode profile must remain intact at all times, as this is the fundamental property of the mode, the evanescent wave on the outside of the curvature would be required to travel at a higher velocity than the central portion of the mode in order for shape to be conserved. However, since light has an upper speed boundary, the evanescent tail is not capable of keeping pace with the central mode velocity, and due to this there is power leakage from the evanescent tail as it can not travel at a faster speed than the main propagating mode. The loss caused by the bend is caused by the mode shape integrity, for as the tail loses power, energy from the main propagating mode shifts into the tail in order for the modal shape to be preserved. Based on this, curved waveguides will suffer an inherent loss. However, it is possible to minimize the radiation bend loss by choosing an appropri-

ate bend radius and arc angle. If, in fact, the bend radius is sufficiently large, the modal profile along the bend should not show a substantial difference from that of the straight waveguide [34]. Since bend radius is of great importance in device creation, various groups have devised methods to analytically calculate the radiation bend loss based on the geometry of the waveguide.

Lee proposed a model based on a simple bending loss formula as shown below [34],

$$\alpha = C_1 \exp(-C_2 R) \quad (2.63)$$

where  $\alpha$  is the bend loss coefficient,  $C_1$  and  $C_2$  are constants that are dependant on a number of factors, and  $R$  is the bend radius, which will be described below.

$$C_{1-Lee} = \frac{\alpha_x^2 \lambda}{\pi(\alpha_x w + 2)} \cos^2\left(\frac{k_{2x} w}{2}\right) \exp(\alpha_x w) \quad (2.64)$$

$$C_{2-Lee} = \frac{2\alpha_x(k_z - k_1)}{k_1} \quad (2.65)$$

Marcatili proposed a similar model, which uses the same formula as Lee, though the constants are different, and shown below [35].

$$C_{1-Marcatilli} = \frac{\lambda \cos^2(k_{2x} \frac{w}{2})}{w^2 \alpha_x N_{eff2} (\frac{w}{2} + \frac{1}{2k_{2x}} \sin(k_{2x} w) + \frac{1}{\alpha_x} \cos^2(k_{2x} \frac{w}{2}))} \exp(\alpha_x w) \quad (2.66)$$

$$C_{2-Marcatilli} = 2\alpha_x \left( \frac{\lambda \beta}{2\pi N_{eff2}} - 1 \right) \quad (2.67)$$

Again, using Lee's original formula, Marcuse's method has constants as follows [36, p.398],

$$C_{1-Marcuse} = \frac{\alpha_x^2 k_{2x}}{k_o^3 N_{eff3} (1 + \alpha_x \frac{w}{2}) (N_{eff1}^2 - N_{eff2}^2)} \exp(\alpha_x w) \quad (2.68)$$

$$C_{2-Marcuse} = \frac{2\alpha_x^3}{3\beta^2} \quad (2.69)$$

Where for all forms, the variables are defined as follows;

$$\alpha_x = k_o \sqrt{N_{eff3}^2 - N_{eff2}^2}$$

$$k_{2x} = k_o \sqrt{N_{eff1}^2 - N_{eff3}^2}$$

$$k_1 = N_{eff2} k_o$$

$$k_z = N_{eff3} k_o$$

$$k_o = \frac{2\pi}{\lambda}$$

$$\beta = k_o N_{eff3}$$

where  $\lambda$  is the wavelength,  $N_{eff1}$  is the effective index of the rib region,  $N_{eff2}$  is the effective index of the slab region, and  $N_{eff3}$  is the effective index across the slab-rib-slab region, or topographical as described before. A fourth model was proposed by Yuanyuan, which uses the basis of Marcuse's model with slight alterations. Yuanyuan's model for radiation bend loss is as follows [29].

$$C_{1-Yuanyuan} = \frac{p^2 k^2 \exp(2pd)}{2k_o^2 (N_1^2 - N_2^2) \beta (1 + pd)} \quad (2.70)$$

$$C_{2-Yuanyuan} = \frac{2p^3}{3\beta^2} \quad (2.71)$$

where  $k = \sqrt{k_o^2 N_1^2 - \beta^2}$ ,  $p = \sqrt{\beta^2 - k_o N_2^2}$ ,  $\beta$  is the propagation constant

of the straight waveguide, and  $d$  is the width of the rib guide. The effective index values noted as  $N_1$  and  $N_2$  for Yuanyuan's model are calculated via equations 2.58 and 2.59, from reference [29].

To avoid large bend losses one must choose a bend radius which is greater than the radius at which the losses become large. Waveguide structures used in this research and described models are shown in Fig. 3.4 and Fig. 3.5, found in section 3.1.2.

## 2.4 Strain Relation to Vibration

Strain,  $\epsilon_x$ , which would be induced in a waveguide via vibration can be described by the tensor  $\epsilon_x = s_{xy}\sigma$ , where the stress field is described by equation 2.72 [37]. The value of the central matrix point is the Poisson's ratio for silicon, which can be found via  $\frac{s_{12}}{s_{11}}$ , where values of  $s_{xy}$  are the compliance constants for silicon.

$$\sigma = \begin{pmatrix} 1 & 0 & 0 \\ 0 & -0.279 & 0 \\ 0 & 0 & 0 \end{pmatrix} \quad (2.72)$$

By following through with the arguments made by Graham Pearson [37], the photoelastic effect on (100) oriented SOI is found via the following, if one assumes  $\epsilon_y = \epsilon_z = 0$ .

$$\Delta n_x = -\frac{1}{2}n^3 \frac{0.721(s_{11} + s_{12})(p_{11} + p_{12}) + 1.44s_{12}p_{12} + 1.28s_{44}p_{44}}{0.721(s_{11} + s_{12}) + 1.279s_{44}} \epsilon_x \quad (2.73)$$

Compliance ( $\times 10^{-12} \text{cm}^2/\text{dyne}$ ) [38]

$$s_{11} = 0.768$$

$$s_{12} = -0.2142$$

$$s_{44} = 1.26$$

Photoelastic [39]

$$p_{11} = -0.094$$

$$p_{12} = 0.017$$

$$p_{44} = -0.051$$

Table 2.1: Compliance and Photoelastic Coefficients for Silicon

$$\Delta n_y = -\frac{1}{2}n^3 \frac{0.721(s_{11} + s_{12})(p_{11} + p_{12}) + 1.44s_{12}p_{12} - 1.28s_{44}p_{44}}{0.721(s_{11} + s_{12}) + 1.279s_{44}} \epsilon_x \quad (2.74)$$

$$\Delta n_z = -\frac{1}{2}n^3 \frac{1.44(s_{11} + s_{12})p_{12} + 1.44p_{11}}{0.721(s_{11} + s_{12}) + 1.279s_{44}} \epsilon_x \quad (2.75)$$

Where values denoted  $s_{xy}$  and  $p_{xy}$  are the compliance and photoelastic constants for silicon and are found in table 2.1. By simply inputting the values of compliance and photoelastic constants into the appropriate places, one can obtain the index variation with respect to strain. The result gives the refractive index change with respect to the x, y, and z directions for strain in the x direction.

$$\Delta n_x = 1.235\epsilon_x \quad (2.76)$$

$$\Delta n_y = -0.483\epsilon_x \quad (2.77)$$

$$\Delta n_z = -0.445\epsilon_x \quad (2.78)$$

The basis of operation is that as the silicon wafer containing the device is vibrated in a cantilever motion, a strain will be induced into the SOI wafer due to the thin wafer flexing. This flexing of the wafer will in turn

cause a repetitive strain field which can be measured via the photoelastic effect and MZI characteristics.

## 2.5 Fourier Spectroscopy

The Fourier Spectrometer based on optical path length manipulation in a Mach-Zehnder Interferometer is very similar to the more familiar version that is based on a Michelson-Interferometer [2]. In the case of the Mach-Zehnder, the optical path length is varied due to temperature variation, as described previously in equation 1.1, where the optical path length is the product of the physical path length and the effective index.

Multiple wavelengths are input into a highly asymmetric MZI in which each of the individual cosine signals can be described by equation 1.3. In the case of the Fourier spectrometer the path length change due to thermal expansion  $\frac{1}{L} \frac{dL}{dT}$  is much less than the change in refractive index due to a temperature change  $\frac{dN}{dT}$ .

$$I_T = \cos \left( \left( n + \frac{dN}{dT} \Delta T \right) k_o (\Delta L) \right) \quad (2.79)$$

However, since there will be at least two wavelengths to be resolved, there will be a small difference in effective index values, and  $k_o$  values due to the different wavelengths. If we assume two wavelengths are being coupled into the highly asymmetric MZI, the intensity output with respect to

temperature will be as follows,

$$I_T = \cos\left((n_1(\lambda, T))\frac{2\pi}{\lambda_1}(\Delta L)\right) + \cos\left((n_2(\lambda, T))\frac{2\pi}{\lambda_2}(\Delta L)\right) \quad (2.80)$$

The total signal  $I_T$  will have a phase interference that is dependent on temperature, however, there will exist an initial phase variation between the two components, which is caused by wavelength dispersion as well as the wavenumber  $k_o$ , of each individual signal. As the temperature is increased, the overall signal  $I_T$  will vary according to the superposition of the two signals. Furthermore, the two signals will act as a single intensity signal with its own phase and periodic shape. This combination of the signals will be split by the MZI and the optical path difference between the two arms will cause an overall phase variation with respect to temperature. Upon recombination at the second Y-branch of the MZI, an intensity variation with respect to temperature will be recorded. Using the Fourier transform for signal analysis, specifically the fast Fourier transform (FFT), one is able to determine the spectrum of the input lightwave.

A simple MatLab program was written to determine a physical path length as well as temperature range that would allow for one to resolve two signals with wavelengths 18nm apart, and centered around 1550nm. Taking into account the parameters which allowed for resolvable peaks in the FFT data set, one is able to have a basis for experimental parameters.

### 2.5.1 Fourier Transform Spectrometer

The resolution of the output signal, once analyzed via the FFT, is highly dependent on the scanned temperature range and physical path length. In order to find the resolution of the spectrometer, one must start with the interference pattern, which can be expressed in the form of an exponential as shown in equation 2.81. One is able to neglect the thermal expansion because  $\frac{1}{L} \frac{dL}{dT} \ll \frac{dn}{dT}$ .

$$\phi = \exp \left( i \left( n_o + \frac{dn}{dT} T \right) k_o \Delta L \right) \quad (2.81)$$

where  $\phi$  is the intensity and  $n_o$  is the refractive index of silicon at around room temperature,  $\frac{dn}{dT}$  is the thermo-optic coefficient, and  $\Delta L$  is the path length difference of the Mach-Zehnder. However, this equation can be broken down in order to extract the temperature dependant portions, shown in equation 2.82, where  $T' = \frac{dn}{dT} T \frac{\Delta L}{c}$ .

$$\exp(i\omega T') \quad (2.82)$$

The value  $T'$  has units of seconds, though it is actually normalized temperature, and the radial frequency  $\omega = 2\pi\nu$ , where  $\nu$  is the optical frequency.

Assuming an N-point data sample the Nyquist frequency needs to be taken into account in order to have appropriate resolution from the (FFT). The Nyquist frequency,  $f_N$ , is equivalent to half the sampling frequency, denoted  $f_S$ . The FFT data set contains half the number of points that the original raw data set contains. Hence, for an N-point sample of raw data,

the number of points contained in the FFT data is  $n = \frac{N}{2} - 1$ , which is representative of the Nyquist, for the FFT data points that range from 1 to  $\frac{N}{2} - 1$ . The values in this range are denoted as bin numbers, from Matlab notation, and are as follows, where one can see that bin 1 produces  $f=0$ , and bin  $\frac{N}{2}$  produces  $f = \frac{f_s}{2} = f_N$ .

$$f = \frac{BinNumber - 1}{N} f_s \quad (2.83)$$

The resolution of an N point raw data sample will correspond to  $\frac{N}{2}$  data points in the FFT, which in turn will give way to a frequency range of 0 to  $f_N$ . The frequency resolution, however, will be  $\frac{2}{N} f_N$ , which is equivalent to  $\frac{f_s}{N}$ , where

$$f_s = \frac{1}{SamplingPeriod} = (Samples/degree) \frac{c}{\frac{dn}{dT} \Delta L} \quad (2.84)$$

Which in turn gives the actual FFT resolution being as follows.

$$Resolution = \frac{Samples/degree \times c}{N \frac{dn}{dT} \Delta L} \quad (2.85)$$

or,

$$Resolution = \frac{c}{\frac{dn}{dT} \Delta T \Delta L} \quad (2.86)$$

The resolution of the system is a frequency difference of neighboring bin numbers of the FFT output. In order to have maximum resolution one desires for  $\Delta T$  and  $\Delta L$  to be as large as possible. Calculations are done appropriately iff  $\frac{N}{2} \times Resolution = f_N$  holds true. In order to find the input wavelengths from the FFT bin numbers, the following can be used,

$$\lambda_x = \frac{c \frac{N}{2}}{BinNumber \times f_N} \quad (2.87)$$

where  $c$  is the speed of light,  $N$  is the number of points in the original data set (including the appended zeros for buffering), and  $f_N$  is the Nyquist frequency.

## 2.6 Metal Clad Rib Polarizer in SOI

Dielectric media such as silicon are non-absorbing within the range of the telecommunications IR wavelengths. However, metals, which have a complex refractive index are well known to be absorbing to wavelengths near 1550nm [31, 2, 23] due to the imaginary portion of the refractive index. Furthermore, it has been documented that a metal film deposited on a slab waveguide or rib waveguide will act as a polarizer since the attenuation of the TM mode will be two orders of magnitude greater than that of the TE mode [31, 40, 41, 42]. The large difference in attenuation of the TE and TM mode allows one to use a metal cladding to create an excessively lossy environment for one mode, while leaving the other relatively untouched.

There are rigorous methods for producing analytical solutions to the problem of metal on top of a rib waveguide though a more user friendly method for achieving these solutions is via the use of Beamprop software. A rib waveguide with a rib height of  $2.5\mu\text{m}$ , a slab height of  $1.5\mu\text{m}$ , and a rib width of  $2\mu\text{m}$  is assumed for loss measurements via BeamProp software. The rib waveguide, with  $500\text{\AA}$  of aluminum cladding, was used to determine the

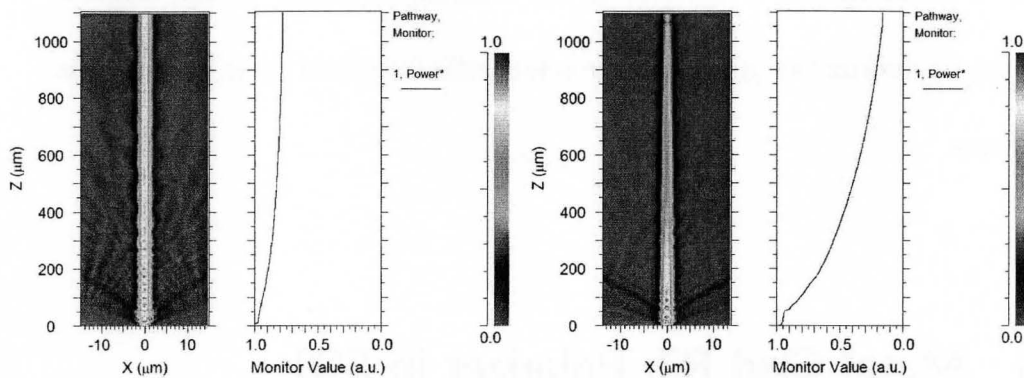


Figure 2.7: Metal Clad Rib Waveguide: TE and TM Modes

overall power loss for both TE and TM modes over a given length of metal, as shown in Fig. 2.7. The left figure shows the overall loss of the TE mode, whereas the right figure depicts the loss of the TM mode for an aluminum cladding length of  $1000\mu\text{m}$  and a thickness of  $500\text{\AA}$ . One can easily see that, in fact, the attenuation of the TM mode is much greater than that of the TE mode due to the aluminum cladding. For comparison, a rib waveguide with no metal cladding is shown in Fig. 2.8. Although the propagational distances are not equal, it is very apparent that the Aluminum cladding causes loss to the TM mode.

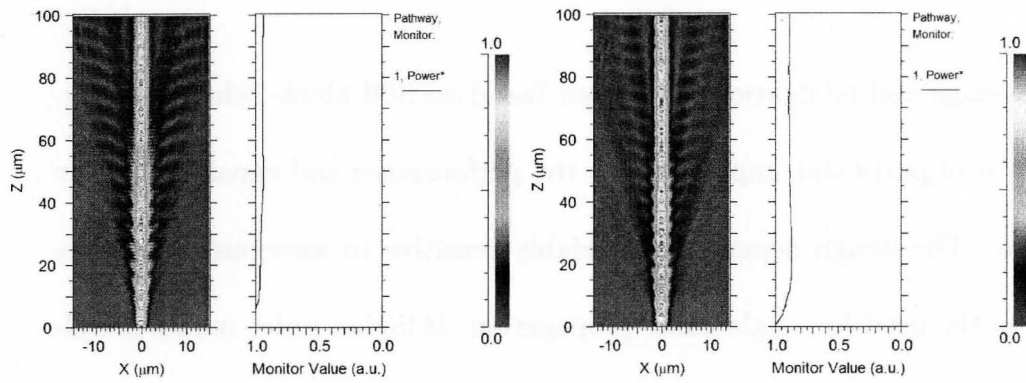


Figure 2.8: Straight Rib Waveguides Without a Metal Cladding Layer: TE and TM Modes

## Chapter 3

---

# Device Design and Fabrication

---

The design and fabrication of a sensor based on SOI Mach-Zehnder waveguides is of particular importance to the performance and capability of the sensor. The design dependence is highly sensitive to waveguide geometry due to the need for single mode propagation. If higher order modes are allowed to propagate, the system is not only much more lossy, but the entire basis of the MZI is compromised, as higher order modes tend to wash out the signal interference between arms. This chapter gives a thorough understanding of chosen design specifications, as well as fabrication procedure.

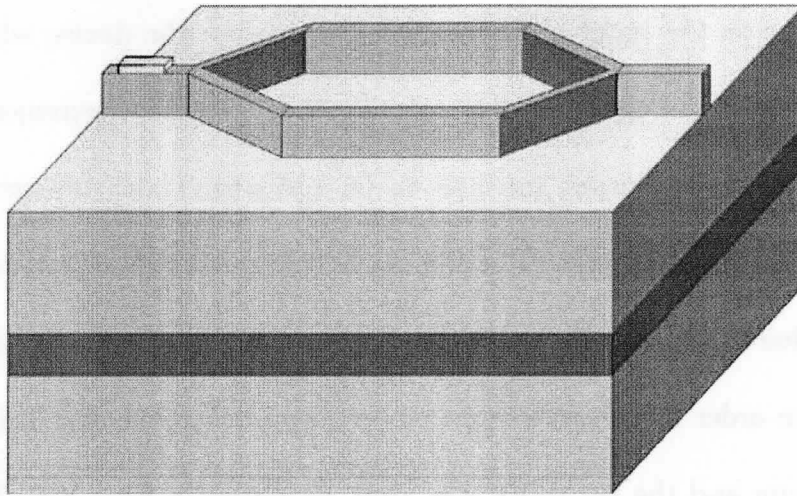


Figure 3.1: Rendering of Mach-Zehnder Interferometer in SOI

## 3.1 Waveguide Geometry

### 3.1.1 Etch Depth and Rib Width

The etch depth and rib width of a waveguide are usually chosen for single mode propagation. The initial phase one design was based on bond and etch back SOI in which the  $\text{SiO}_2$  insulating layer was  $1\mu\text{m}$  in thickness, and the silicon film was  $5\mu\text{m}$  thick. These dimensions, based on equations 2.45 and 2.46, allow for single mode propagation if the slab height is  $3\mu\text{m}$  and the rib width is  $5\mu\text{m}$ . The phase one design, however, was not designed to be self normalizing as there was only the MZI. Due to this, a second phase system was designed based on SIMOX SOI, from Intel, in which the  $\text{SiO}_2$  insulating layer was  $0.375\mu\text{m}$  thick, and the silicon film was  $2.5\mu\text{m}$  thick. SIMOX SOI was chosen for the phase II design for it is of higher quality and consistency than bond and etch back. Phase II was designed to be

self normalizing as the input waveguide was split before the device which allowed for straight through measurements as well as device measurements. In this way the device output was able to be normalized with respect to the split off straight waveguide. The thinner SOI film allowed for a tighter bend radius due to smaller waveguide dimensions, but was also used due to availability. In order to preserve single mode propagation, the slab height chosen was  $2\mu\text{m}$  and the rib width was  $2\mu\text{m}$ , as shown in Fig. 3.2. The chosen rib dimensions are strongly related to the radiation bend loss, which is described in the following section.

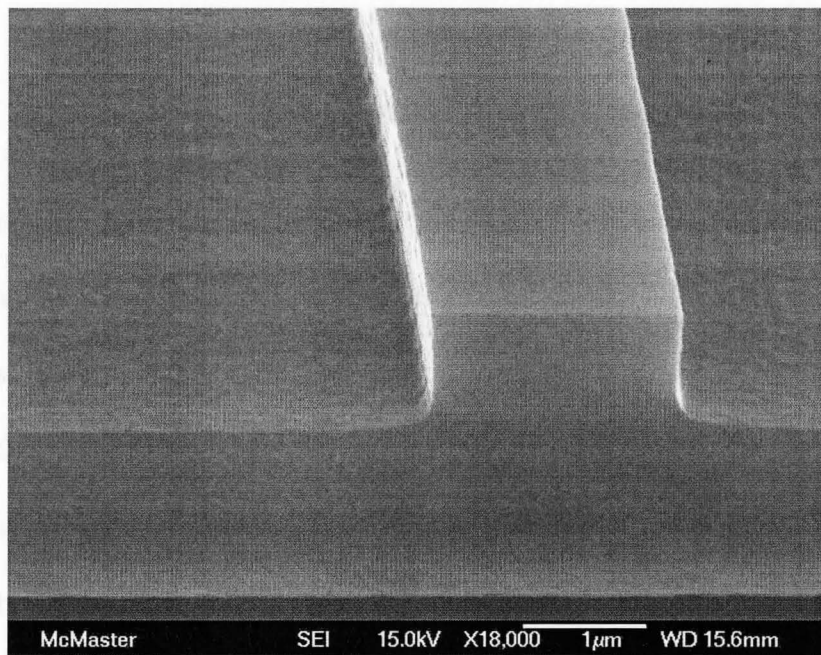


Figure 3.2: Rib Waveguide Cross Section - SEM Image

The choice of rib width and slab height that satisfy the single mode condition are easily found theoretically, however, the actual throughput power of an optical signal within the confines of the single mode region can be

greatly affected by the etch depth. Referring to Fig. 2.4, one can note the significant area in which rib geometry can cause single mode propagation. As the etch depth increases, the slab height decreases, which lowers the value of  $h$ , which in turn decreases the ratio  $\frac{h}{H}$ , as  $\frac{W}{H}$  remains constant. This causes the waveguide point in the single mode region to become closer to the multimode region. Choosing a geometry that is close to the multimode region will result in a greater throughput of power, and hence is more desirable. To give justification to this argument, an etch depth of  $0.85\mu\text{m}$  was initially used in both the phase one and phase two designs. A second etch depth of  $2\mu\text{m}$  and  $1\mu\text{m}$  was completed for the phase one and phase two geometries, respectively. The power throughput of both designs was found to increase by at least double in both cases for a number of waveguides tested. The reasoning behind the greater power throughput is modal confinement in the horizontal direction. There is a trade off, however, for greater etch depths allow for more scattering as the waveguide sidewall is larger, which allows for the mode to interact with more sidewall roughness.

### 3.1.2 Bend Radius and Y-Branched

Inherent to the design of a rib waveguide based MZI are S-Bends and Y-Branched. S-Bends are used to curve the waveguide of one MZI arm along a distance that is greater than the other, and in doing so creates asymmetry between the two arms. Furthermore, because the S-Bends of each MZI arm

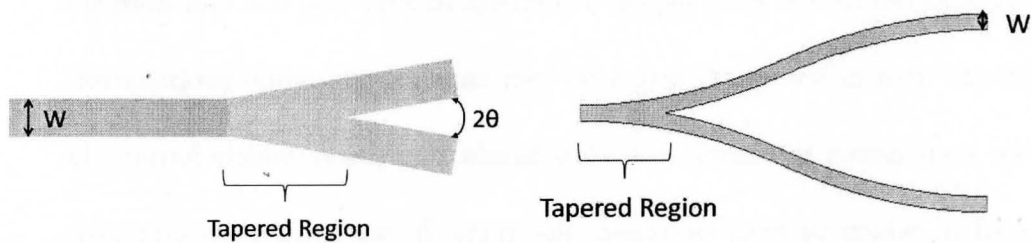


Figure 3.3: Straight Arm Y-Splitter and S-Bend Splitter

will have slightly different arc angles as well as radius, Y-branches must be implemented to ensure the appropriate 50/50 signal and power split to each arm, as previously described in section 2.3.3. The straight arm Y-branches were chosen such that the angle  $\theta$  between the arms, as shown in Fig. 3.3, was  $1^\circ$ . The actual linear distance covered by the splitting arms was  $2290\mu\text{m}$ , and the separation at that distance was  $19\mu\text{m}$ . At these dimension the splitting was gradual enough that the overlap integral at the interface of the straight waveguide and branched waveguide did not change the mode profile enough to induce excessive loss. Furthermore, a lesser angle would have resulted in a longer tapered region, which would induce greater losses, as previously described in section 2.3.3.

The construction of the MZI for this research will have S-bends, as shown in Fig. 3.3, in order to create asymmetry as well as smooth transitional phases between waveguide segments. The S-bend itself is a composition of two circular arcs which are double flipped and connected. The arc itself will

have a defined and chosen bend radius as well as arc segment angle, which is a measure of the degrees that the arc will traverse. These parameters were chosen via models that have been illustrated in section 2.3.3. In order to ensure the least amount of loss due to waveguide bending, a program was developed to calculate the various bend losses for the TE and TM fundamental modes. The program calculated bend losses in dB for an arc of  $90^\circ$  and a chosen bend radius, as shown in Fig. 3.4 and Fig. 3.5. Specific waveguide geometry is also shown in the previously mentioned figures. The various curves in each figure are based on the models developed by Lee, Marcitili, and Marcuse as described in Chapter 2. The development of each solution is based on modal effective index, which in turn is based on waveguide geometry. A program in Maple 11 has been developed that calculates and generates plots based on chosen waveguide geometry and wavelength. The program can be found in Appendix A.

Waveguide bend radius was chosen based on Fig. 3.4 and Fig. 3.5, which show that there will be little to no bend losses for a  $90^\circ$  arc if the bend radius is greater than 1.5mm. However a minimum bend radius of 3.5mm was implemented in the design of all sensors in order to be well beyond the highly loss limit. As one may note, the loss increases rapidly as the bend radius goes below 1.5mm. Furthermore, the bend loss is slightly different for TE and TM modes based on modal confinement in the horizontal and vertical directions of the waveguide.

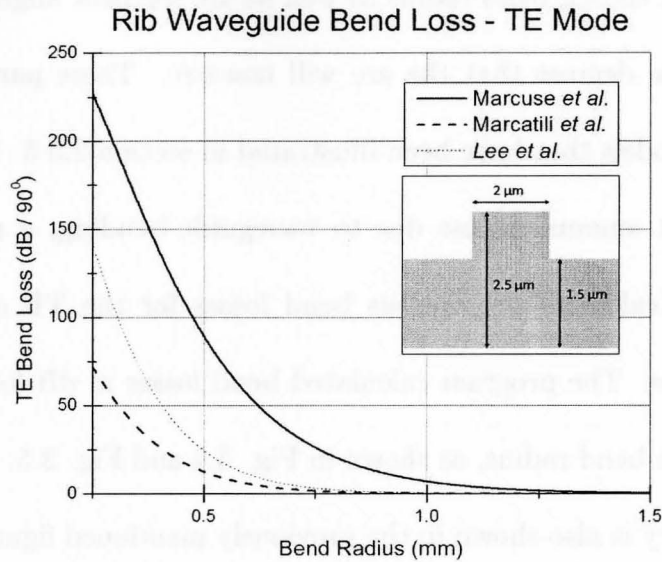


Figure 3.4: Radiation Bend Loss of Fundamental Mode: TE Polarization

## 3.2 Mach-Zehnder Design

An asymmetric Mach-Zehnder will inherently have a phase difference between arms unless the path length difference is wisely chosen with respect to the desired wavelength as well as temperature range. Given that the wavelength of choice was to be  $1.54612\mu\text{m}$  (wavelength available on ITU laser grid), the refractive index based on wavelength dispersion (equation 1.6) with no temperature dependence was found to sit at 3.4767. Given that the refractive index has a temperature dependence, as described in section 1.2.1, of  $1.818 \times 10^{-4} \text{K}^{-1}$  for temperatures in the range of 273 Kelvin to 400 Kelvin, one is able to begin putting the picture together. It is primarily this change in refractive index that brings about the variation in the optical path length of each arm in addition to the already existing asymmetry.

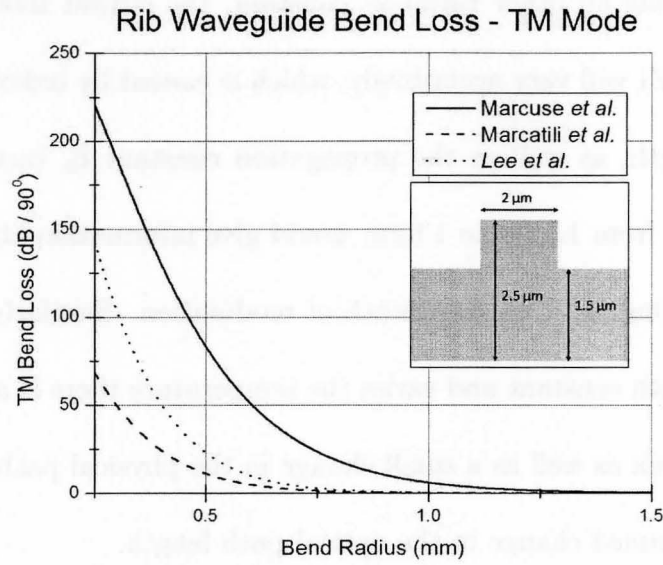


Figure 3.5: Radiation Bend Loss of Fundamental Mode: TM Polarization

However, there is an additional contribution due to linear thermal expansion, which does play a role in the optical path length change, though to the lesser degree of  $2.65 \times 10^{-6} \text{K}^{-1}$ .

### 3.2.1 Mach-Zehnder Temperature Sensor

The design of the asymmetric MZI was brought about via theoretical calculations, based on equation 1.3, which will be reiterated and normalized for ease of use and understanding.

$$I(T) = 0.5 + 0.5 \cos \left( (n_\lambda + 1.818 \times 10^{-4}T) \left( \frac{2\pi}{\lambda} \right) (\Delta L + 2.65 \times 10^{-6}T\Delta L) \right) \quad (3.1)$$

As one might infer from equation 3.1 the overall intensity will oscillate if one varies wavelength or temperature. If one decides to vary the wave-

length, while keeping all other variables constant, the output intensity of the asymmetric MZI will vary accordingly, which is caused by index dependence on wavelength, as well as the propagation constant  $k_o$  varying. A wavelength tuning from  $1.5\mu\text{m}$  to  $1.6\mu\text{m}$  would give information about the MZI such as splitting ratio via the depth of modulation. Similarly, if one holds the wavelength constant and varies the temperature there is a change in the effective index as well as a small change in the physical path length, which causes a summed change in the optical path length.

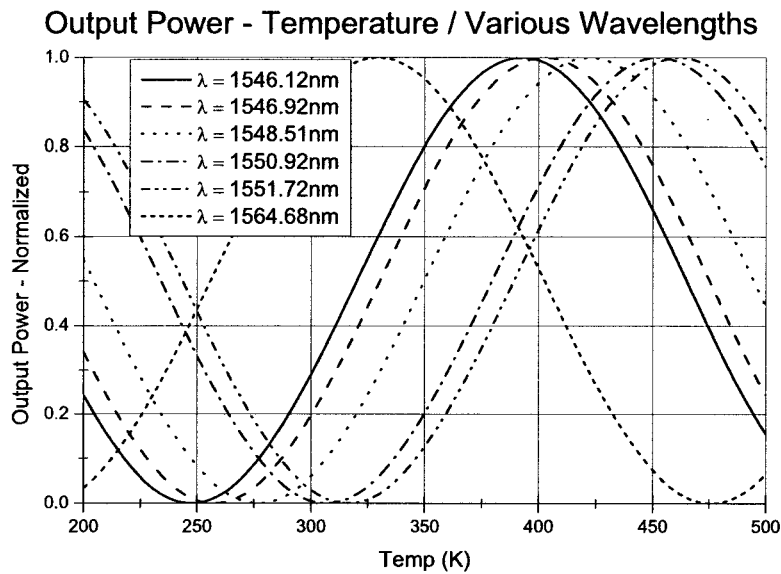


Figure 3.6: Normalized Output of MZI with  $\Delta L$  of  $27.85\mu\text{m}$  for Various  $\lambda$ , Temperature range of 200K to 500K

In order to design a temperature sensor based on the oscillating signal behaviour of a MZI, the temperature range needs to be known. The MZI output tunes monotonically in one direction with no maximum or minimum if a  $\Delta L$  and  $\lambda$  are selected appropriately, as shown in Fig. 3.6. If the path

length is chosen wisely one can force the  $\frac{\pi}{2}$  segment to be such that the low end temperature is at a max/min and the high end temperature is at a min/max, respectively. A greater temperature variation is shown in Fig. 3.6, though there are a number of widely used telecommunications wavelengths used to show the difference due to wavelength for a MZI with a path length difference of  $27.85\mu\text{m}$ . The wavelengths shown in Fig. 3.6 where chosen for they are the wavelengths available in the lab. This figure takes into account the change in refractive index due to temperature, linear thermal expansion, and refractive index wavelength dispersion. Taking a closer look at the specific range of interest, which is 293K to 400K, one is able to see that at a specific path length difference, there are wavelengths that cause the MZI intensity output to have no maxima nor minima in the desired temperature range, which are 1546.12nm, 1546.92nm, and 1548.51nm, as shown in Fig. 3.7.

In order to give a further understanding of the importance of taking the thermal expansion,  $dL/dT$ , and wavelength index dispersion,  $n(\lambda)$ , into account, each condition is taken out of equation 3.1 and compared to equation 3.1 in its entirety. The standard equation, with thermal expansion and dispersion based index with no thermal expansion are compared to the theoretical model as described in Fig. 3.8. One can see that the theoretical model which takes dispersion as well as thermal expansion into account is very different than those that do not, which reiterates the importance of

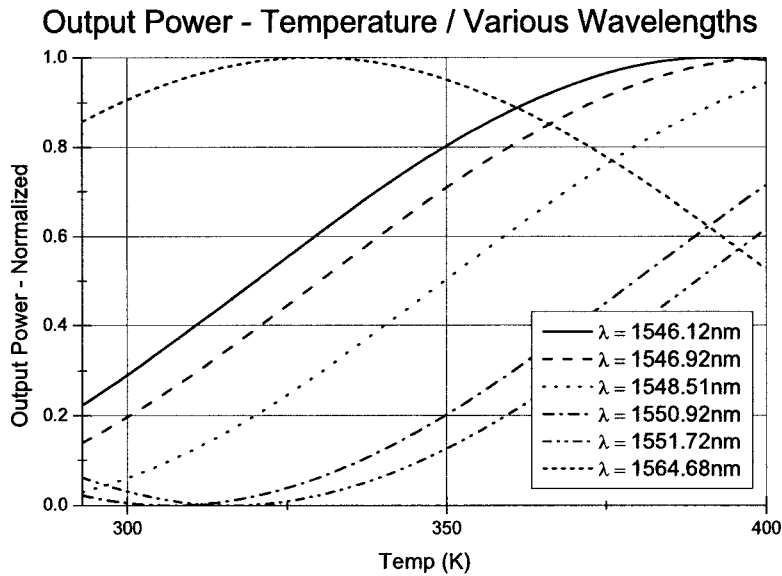


Figure 3.7: Normalized Output of MZI with  $\Delta L$  of  $27.85\mu\text{m}$  for Various  $\lambda$ , Temperature range of 273K to 400K

taking  $n(\lambda)$  and  $dL/dT$  into account.

### 3.2.2 Mach-Zehnder Vibration Sensor

The vibration sensor was designed as a highly asymmetric MZI in a manner such that the large arm would contain straight sections in order to create a strain field in the waveguides, and hence vary the refractive index. The asymmetry was varied in order to obtain a sensor which was most sensitive in a specific range from 0g to 2g. The path length differences chosen were 1.05cm, 2.05cm, and 3.05cm. Each MZI would have a larger portion of one arm to which strain could act upon, and hence greater sensitivity to varying frequencies of vibration. The design of the vibration sensor can be seen in Fig. D.2 found in Appendix D

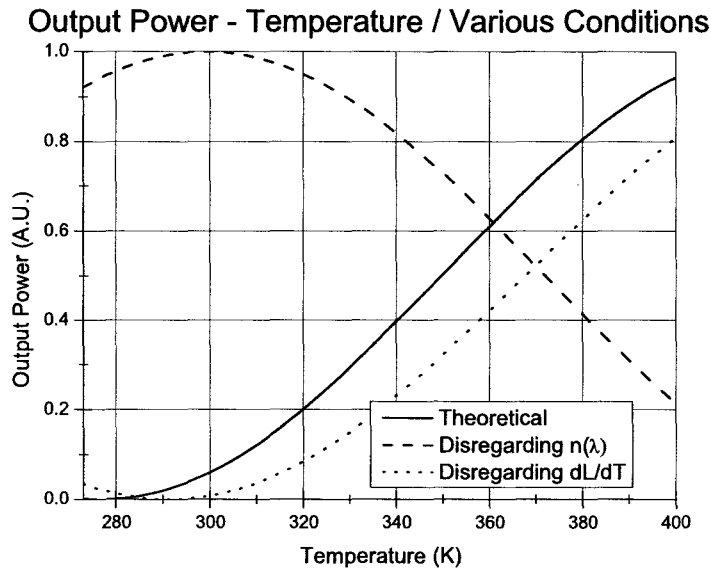


Figure 3.8: Normalized Output of MZI with  $\Delta L$  of  $27.85\mu\text{m}$ . A Comparison of Contributing Factors when  $\lambda$  is  $1548.51\text{nm}$

### 3.2.3 Mach-Zehnder Fourier Spectrometer

The highly asymmetric MZI was initially designed to be used as a vibration sensor. However, because the path length difference for the vibration design was on the order of  $1.05\text{cm}$  and  $3.05\text{cm}$  the same devices were utilized for the purpose of demonstrating the Fourier spectrometer.

### 3.2.4 Polarizers on SOI Rib Waveguides

Polarizers were designed in order to cause high attenuation of the TM mode while leaving the TE mode unaffected. To achieve this a masking system was fabricated to ensure a single strip of metal of a defined length was located on top of the rib waveguide. The metal lengths were varied from

500 $\mu\text{m}$  to 2500 $\mu\text{m}$  in intervals of 500 $\mu\text{m}$ .

## 3.3 Fabrication

### 3.3.1 Waveguides

Waveguides were fabricated via photolithography masking and Reactive Ion Etching (RIE). However, due to the nature of the waveguide dimensions some operations needed to be altered to ensure the mask features were of appropriate dimension. Soft baking was done with aluminum foil as a hotplate cover and a peatry dish lid to cover the sample, for a time of 2min 20s at 110°C. UV exposure was increased from 30mJ/cm<sup>2</sup> to 32mL/cm<sup>2</sup>, for regular exposure caused the photoresist to have angled sidewalls, as shown in Fig. 3.9. There is extensive damage to the silicon surface in Fig. 3.9, for the Gold/Chromium metalization procedure caused "micromasking"[43], which will be described in more detail in section 3.3.2. The hardbake was done in the same manner as softbake, though increasing the temperature to 130°C.

### 3.3.2 Polarizers

The procedure to produce a metal film only on top of the waveguide ribs was a two step procedure in which chromium/gold, and aluminum was evaporated onto the silicon surface after a 20 min UV ozone cleaning and 30

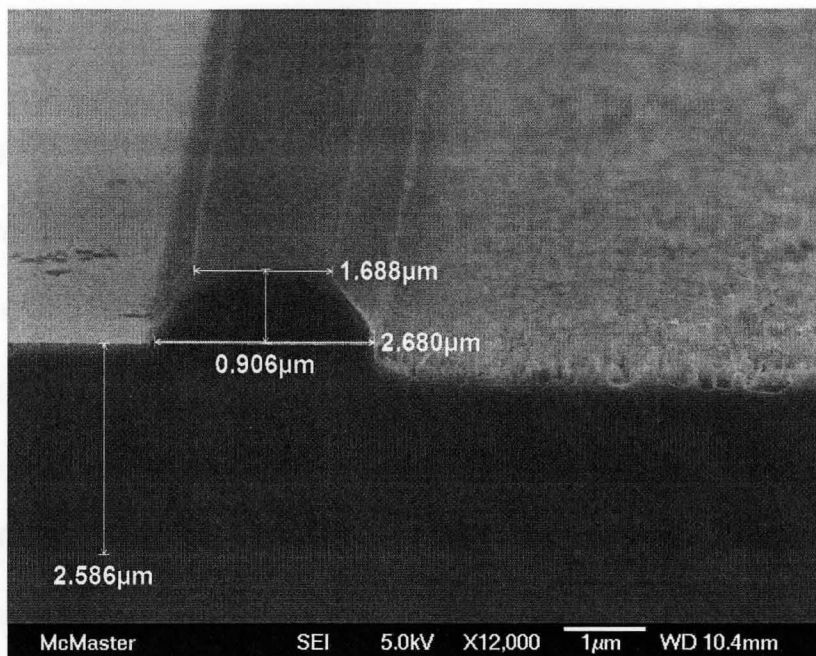


Figure 3.9: Photoresist after regular processing: Note sidewall angle

sec HF bath to ensure surface cleanliness and native oxide removal. Following metal deposition the photolithography procedure was carried out. Then a wet metal etch was used to remove metal from all places which were not coated in photoresist. The etchants for chromium/gold and aluminum are described in detail in the following subsections. The sample was then etched via RIE at the University of Western Ontario, leaving a thin coating of metal on top of the etched ribs. The second photolithography procedure was implemented in order to cover a small section of the metalized ribs over a straight section of the rib. A second metal etch is used to remove the metal film from the ribs in undesired locations, leaving a metal clad rib to act as a polarizer.

### **Gold/Chromium Metalization**

Gold was used initially as the metal of choice to act as the polarization material. However, gold is well known to have a poor sticking coefficient to silicon due to the native oxide formation on silicon. In order to overcome this a thin, 30Å film of chromium was deposited onto the silicon samples via e-beam evaporation. Then gold films of thickness 100Å, 500Å, and 1000Å were deposited over the chromium film via e-beam evaporation. Once completed the samples underwent a regular photolithography procedure as described above in the waveguide fabrication procedure, followed by a wet gold etch (5% I<sub>2</sub> + 10% KI + 85% H<sub>2</sub>O) followed by a wet chromium etch. It was found that the gold etchant in its pure form was too aggressive and would under-etch and attack the photoresist at a rate which made it unusable. In order to counter this the gold etchant was diluted 50/50 by volume with de-ionized water and a hard bake of 6 minutes at 130° C was used. Upon dilution and increased hard bake time the etch rate was reduced from a rate of 1000Å /second to a rate of around 40Å /seconds. The reduced rate allowed for more controlled processing.

The RIE portion of the processing, however, also caused issues for the process of RIE is highly selective to silicon and will not etch other materials with nearly as much vigor. It was found that upon etching, "silicon grass" or "black silicon" was formed, which is a sign of micromasking. Micromasking is caused by small amounts of material on the surface of the silicon or slightly

below the surface interfering with the silicon being etched. In this case, the thin chromium film had diffused into the silicon, and caused micromasking. The surface damage caused by the micromasking was severe and rendered the samples unusable, as shown in Fig. 3.10.

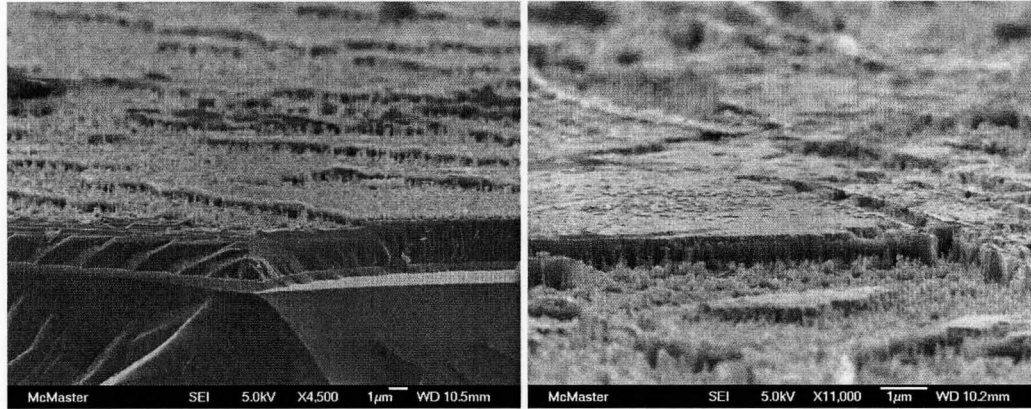


Figure 3.10: Surface Damage due to Micromasking after RIE

### Aluminum Metalization

Upon investigation it was found that aluminum would be a more appropriate material to use as a polarizer since aluminum readily sticks to silicon as well as  $\text{SiO}_2$ . The process of metalization as well as lithography was followed in the same manner as for gold. However, the aluminum also caused micromasking, though to a lesser of a degree than the Cr/Au. An attempt was made to eliminate the micromasking by growing a  $100\text{\AA}$  film of  $\text{SiO}_2$  to act as a sacrificial layer so that the diffusion of aluminum would be stopped by the thin film of oxide, as this is a method utilized in creating ohmic contacts

in silicon. The sacrificial layer did decrease the amount of micromasking, though it did not clear the problem completely. One observation of interest was the time dependence of the density of silicon grass. It was found that a longer time during which aluminum was left on silicon led to more dense silicon grass, due to greater diffusion of aluminum into the silicon. The aluminum not only diffused into the silicon but it also formed  $\text{Al}_2\text{O}_3$  [44].

Because the various methods of metalization did not work out in the manners described above, a more simplistic method was formulated in which the waveguides were etched, then metal was deposited over the entire surface. The photolithography procedure was again utilized in an attempt to align the mask ribs with the existing silicon ribs. Once the ribs were aligned to satisfaction, aluminum etchant was used to remove aluminum from all surfaces except for on top of the ribs. A second photolith and aluminum etch was used to remove aluminum from the top of the ribs, except for those places where it was desired. A graphical representation of the process is presented in Fig. 3.11 to Fig. 3.13. Fig. 3.11 shows the basic profile of an unprocessed SOI wafer as well as the rib waveguide cross sectional form after RIE. Fig. 3.12 shows the process of metalization as well as the coverage of photoresist directly above the rib. The final figure shows the cross sectional view of the metal clad rib.

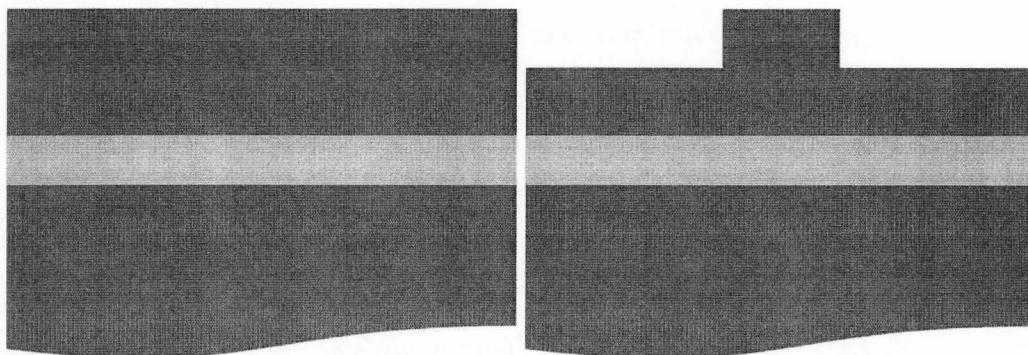


Figure 3.11: Initial Silicon Surface Unprocessed and Silicon Rib Waveguide After RIE

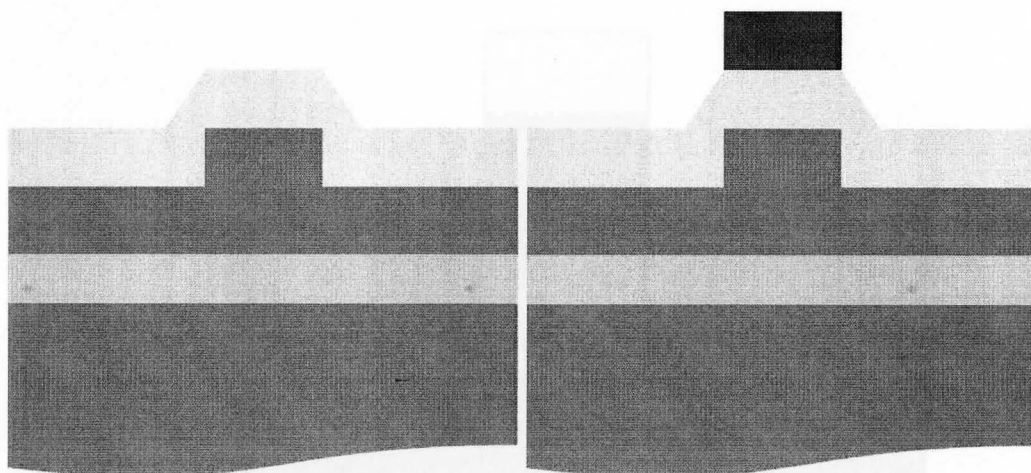


Figure 3.12: Metalization of Entire Surface and Photoresist Over Rib Waveguide

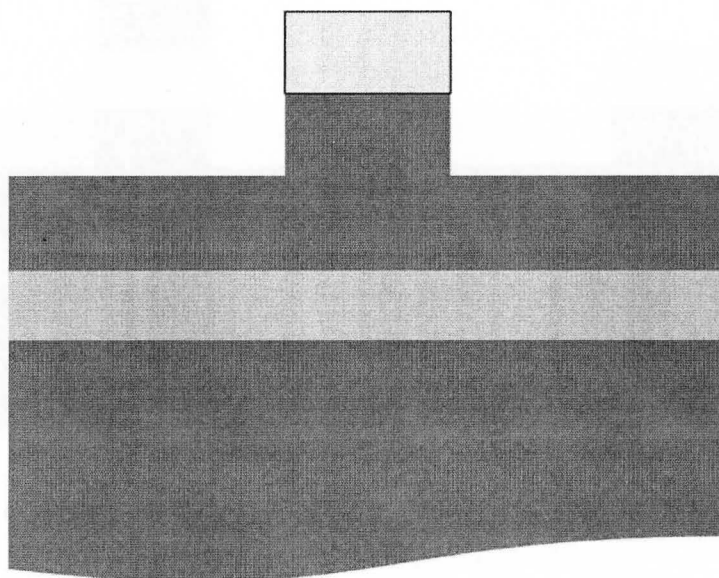


Figure 3.13: Final Metalized Rib Polarizer: Cross Section View



## Chapter 4

---

# Results and Discussion

---

The Results and Discussion section will outline the main findings of the Phase I and II temperature sensors, the Fourier Spectrometer, and Aluminum Clad Rib Polarizer.

### 4.0.3 Experimental Setup

The experimental setup consisted of several available lasers operating on ITU wavelengths ranging from 15546.12nm to 1564.68nm, to which a lead connection was sent through polarization paddles to ensure a pure TE or TM mode. The paddle output then ran out to a non-polarization-maintaining fiber, with a spot size of  $2.5\mu\text{m}$ , for best fiber to waveguide alignment. The sample rested upon a copper block, which was heated or cooled via a thermoelectric cooler/heater(TEC). The TEC was controlled via a Newport TEC controller with the aid of a feedback loop and a  $10\mu\text{A}$  thermistor. A polarizer

was utilized after the objective to ensure a clean polarization signal, after which the signal was sent through an aperture, to cut out slab guided light and radiation modes, and then on to the optical power meter. A graphical schematic can be found below in Fig. 4.1.

In the case of spectrometer testing, the apparatus was slightly altered to combine multiple wavelengths in the input fiber, however the premise of the experimental apparatus remained consistent throughout.

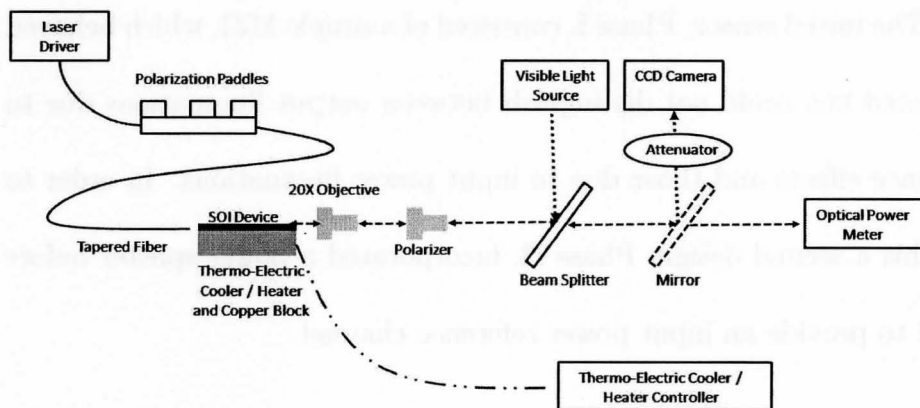


Figure 4.1: Experimental Bench Apparatus

Losses across the experimental apparatus were found by starting with the tapered fiber directly into the sensor and adding components into the apparatus, taking throughput measurements as each individual component was put in. The 20X objective creates a loss of 1.2dB, the polarization isolator creates a loss of 0.3db, the air gap between the polarizer and power meter causes a 0.03dB loss, and the beam splitter creates a loss of 0.22dB. Overall the experimental apparatus, with no sample in place, has a cumulative loss of 2.18dB. The losses were measured by using the initial power

from the tapered fiber directly into the power meter, then comparing that to the power found through each optical component.

## 4.1 Asymmetric Mach-Zehnder Temperature Sensor

The design of the MZI temperature sensor underwent a two stage process in which the original design was altered in order to create a self normalizing sensor. The initial sensor, Phase I, consisted of a simple MZI, which behaved as predicted but could not distinguish between output fluctuations due to interference effects and those due to input power fluctuations. In order to rectify this a second design, Phase II, incorporated a power splitter before the MZI to provide an input power reference channel.

### 4.1.1 Phase I Temperature Sensor

The initial, Phase I mask contained interferometers with four different path length differences in order to capture a broad range of possible temperature spectra, as shown in Fig. 4.2. It was found, both theoretically as well as experimentally that as the path length difference increases, there is a decrease in the temperature range that fits between adjacent extrema of the sinusoidal MZI output. Based on this there exists an optimal path length difference for which a specific temperature range can be measured. The Phase I device consisted of path length differences of  $2.54\mu\text{m}$ ,  $10.5\mu\text{m}$ ,

23.46 $\mu\text{m}$ , and 37.23 $\mu\text{m}$ . The theoretical performance of these MZI's, at a wavelength of 1546.12nm, are shown in Fig. 4.3, which takes into account the thermal expansion of silicon. The corresponding experimental curves are shown in Fig. 4.4.

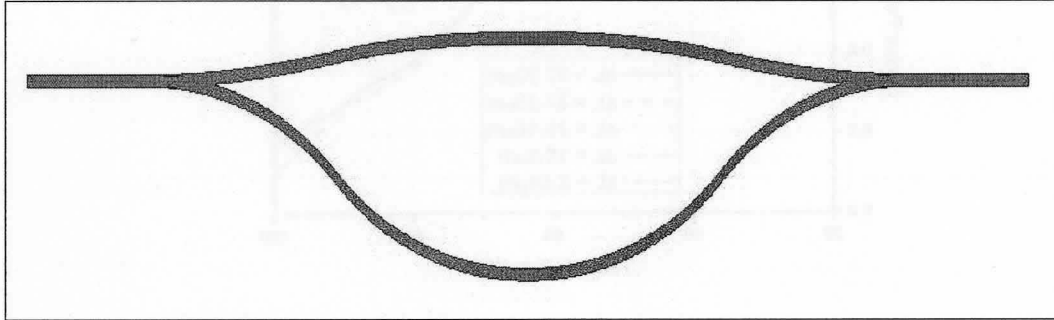


Figure 4.2: Phase I Mask Design - Single Asymmetric Mach-Zehnder Interferometer

Phase I - Normalized Power Output with Temperature Tuning

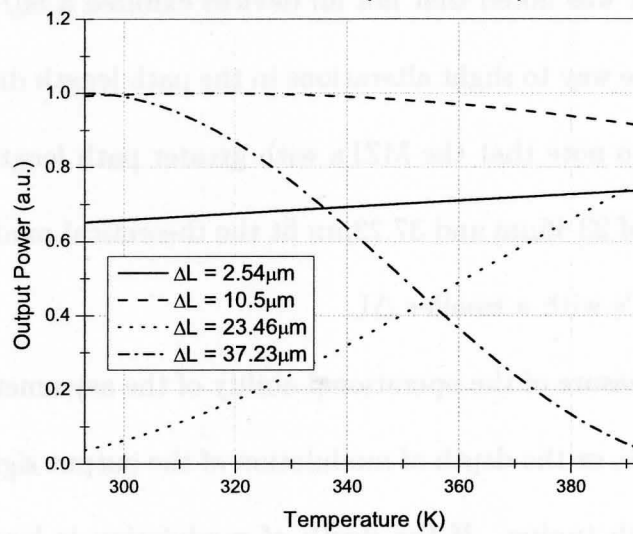


Figure 4.3: Normalized Theoretical Output of Phase I Device for  $\lambda=1546.12\text{nm}$

Although it is apparent that the experimental do not match up exactly with the theoretical, the main cause is fiber alignment and device profile.

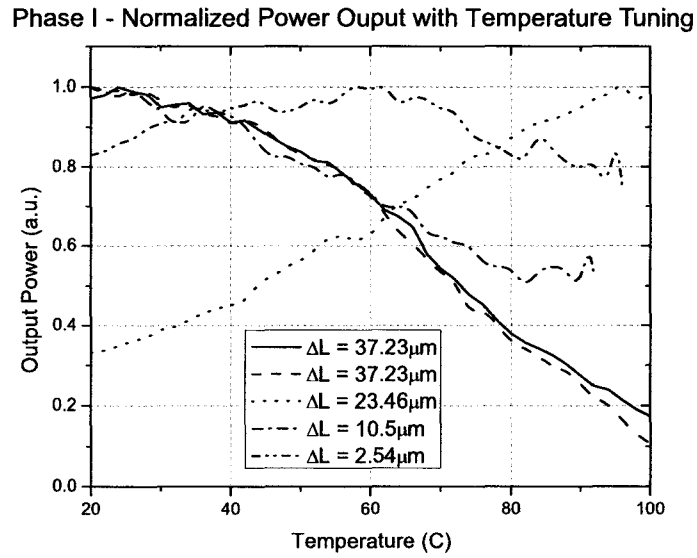


Figure 4.4: Normalized Experimental Output of Phase I Device for  $\lambda=1546.12\text{nm}$

During fabrication it was noted that not all devices exhibited a 50/50 splitting ratio, which gave way to slight alterations in the path length difference. Also, it is valuable to note that the MZI's with greater path length differences such as those of  $23.46\mu\text{m}$  and  $37.23\mu\text{m}$  fit the theoretical model much better than the MZI's with a smaller  $\Delta L$

An important measure of the operational ability of the asymmetric MZI is the extinction ratio, or the depth of modulation of the output signal with respect to wavelength tuning. If the depth of modulation is large, on a percentage basis, the signals have separated in a manner which suggests a 50/50 splitting and recombination. However, a lessened depth of modulation indicated that the splitting ratio is not 50/50. When the splitting or recombination of signals along the arms or the MZI is not equal, the signal

in one arm will contain less power and will have less of an effect on the overall output signal upon recombination. The extinction ratios of the  $23.46\mu\text{m}$  and  $37.23\mu\text{m}$  MZI's are shown in Fig. 4.5. As noted via graphical analysis from the previously mentioned figure, the extinction ratio of the  $23.46\mu\text{m}$  MZI is 97.4% and the  $37.23\mu\text{m}$  is 94.8%. The higher frequency modulation which followed the main signal trend is due to a Fabry-Perot effect and was noted to take place in experimentation when the tapered fiber is directly in front of the the detector, as shown in Fig. 4.6.

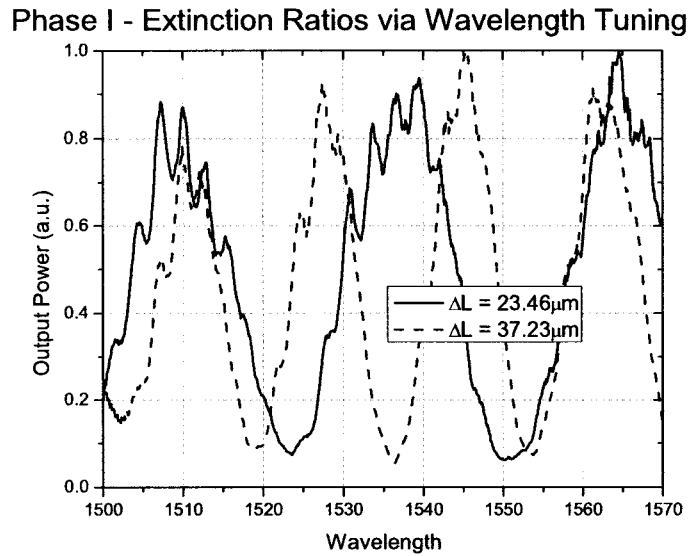


Figure 4.5: Normalized Experimental Extinction Ratios of Phase I Device via Wavelength Tuning

The smaller fringes in Fig. 4.5 exhibit a peak to peak spacing of around 3nm and the fringes in Fig. 4.6 show a 3nm peak to peak spacing. An experiment was conducted in which the tapered fiber was set at  $10\mu\text{m}$  to  $15\mu\text{m}$ ,  $15\mu\text{m}$  to  $20\mu\text{m}$ ,  $20\mu\text{m}$  to  $25\mu\text{m}$ , and  $25\mu\text{m}$  to  $40\mu\text{m}$  distances from

the silicon sample in order to determine the cause of the smaller fringes. This experiment shows that the air gap from the fiber to sample is not the cause of the fringes for changing the air gap does not alter the peak to peak spacing of the higher order fringes, as shown in Fig. 4.7. The fringes also occur when a sample is in place and fiber to sample spacing is held constant. An additional experiment was conducted whereby the tunable laser source was connected directly to the optical power meter in order to rule out fringes caused by air gaps between optical components. This setup also exhibited a 3nm peak to peak fringe spacing, as shown in Fig. 4.6. The 3nm fringe spacing is most likely Fabry-Perot interference fringes, which would suggest an air gap of  $400\mu\text{m}$  or a semiconductor gap of  $nL = 400\mu\text{m}$ . A possible cause of the repeatable fringes is a degradation of the anti-reflection coating within the tunable laser itself or an unknown air gap in the detector.

The precision of the Phase I device was limited by an inability to normalize the throughput with respect to the input to the MZI. Straight waveguide analysis via wavelength variation known as Fabry-Perot loss analysis indicated losses on the order of 4dB/cm to 7dB/cm depending on the waveguide [30]. In practice the MZI with a  $\Delta L$  of  $23.46\mu\text{m}$  was able to accurately measure temperature to about  $2^\circ\text{C}$ , while the MZI with a  $\Delta L$  of  $37.23\mu\text{m}$  had a temperature accuracy of  $1^\circ\text{C}$  and a sensitivity of  $0.5^\circ\text{C}$ .

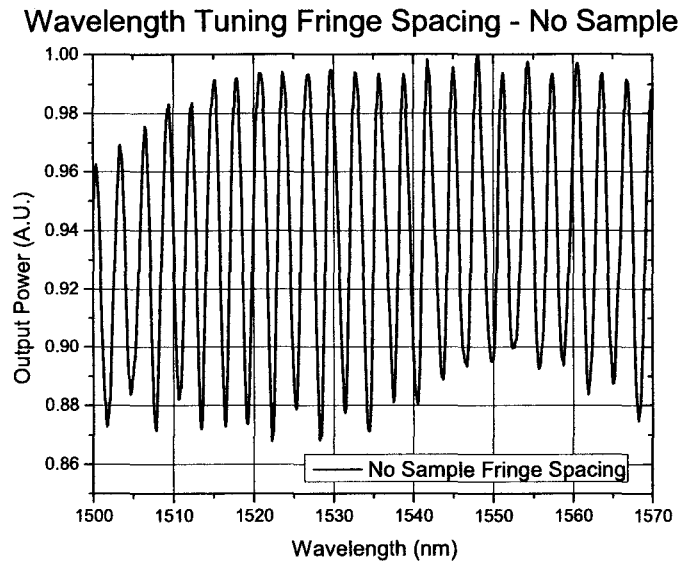


Figure 4.6: Normalized Experimental Wavelength Tuning: Tunable Laser Source Directly Into Optical Power Meter

### 4.1.2 Phase II Temperature Sensor

The phase II design was re-modeled in order to use a tighter bend radius as well as a more precise temperature range of 0 to 120°C, and in doing so required different dimensions as well as path length difference. The phase II design had a  $\Delta L$  of 27.85 $\mu\text{m}$ , which would give a working temperature range of 0 to 120°C at a wavelength of 1546.12nm. Moreover, the phase II design contained a self-normalizing arm, as shown in Fig. 4.8. The self-normalizing arm, or reference arm is necessary to have a point of intensity reference for the sensor.

An initial etch depth of 0.85 $\mu\text{m}$  was used, though this etch depth caused a poor splitting ratio from the main input waveguide. A second etch depth of 1.0 $\mu\text{m}$  was found to solve this problem. Both the 0.85 $\mu\text{m}$  and 1.0 $\mu\text{m}$

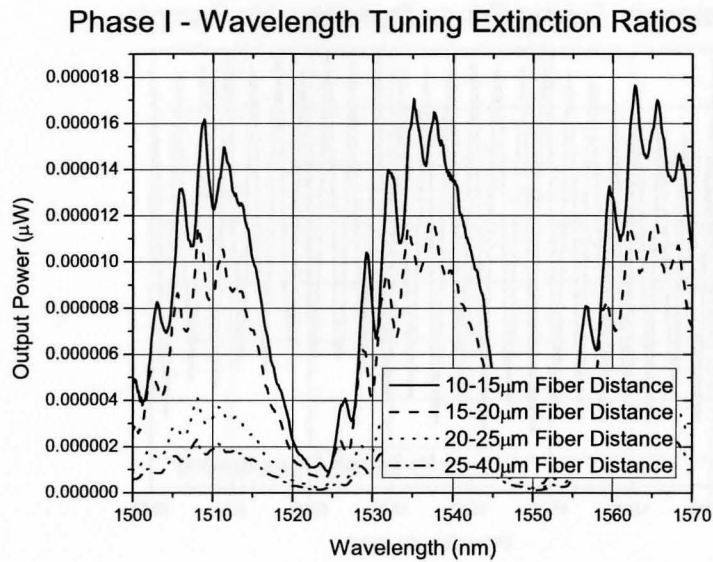


Figure 4.7: Phase I - Wavelength Variation with Fiber to Sample Distance Varied

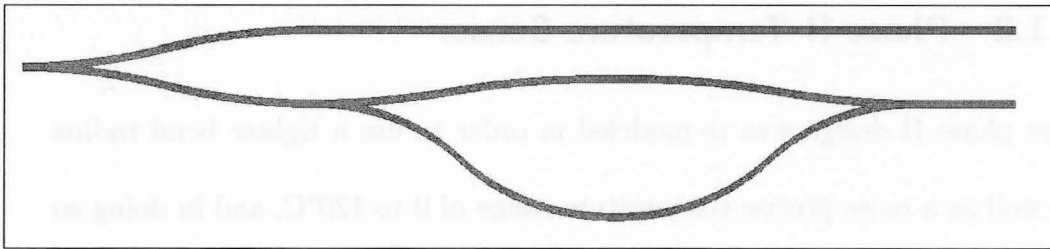


Figure 4.8: Phase II Mask Design - Self Normalizing Asymmetric Mach-Zehnder Interferometer with Reference Arm

etched samples were cleaved along the point of the initial arm split in order to determine splitting ratios. The shallow etched ribs had splitting ratios which ranged from 20/80 to 50/50 and showed no patterned consistency. However, the more deeply etched ribs showed a consistent splitting ratio of 50/50, to which the greatest deviation across 20 waveguides was 3%, with a standard deviation of 2.7.

The phase II temperature design had two consistent outputs for the

temperature range of 20 to 100°C, as shown in Fig. 4.9 and 4.10. The actual design was intended to appear as shown in Fig. 4.9, though half of the acquired data followed that of Fig. 4.10. Upon closer investigation of the governing equation, it is found that a deviation of 0.2 $\mu\text{m}$  in the path length difference will change the phase difference at the MZI output by 180°. This causes an interference pattern that decreases rather than increases with increasing temperature. It is believed that the branch points of the MZI are responsible for the  $\Delta L$  deviation for waveguide divergence and convergence points have spacing which are smaller than the experimental limits of the photolithography technique. The data shown in Fig. 4.9, and Fig. 4.10 are taken from MZI's that have been designed to have a path length difference of 27.85 $\mu\text{m}$ . Fig. 4.9 is representative of the path length difference 27.85 $\mu\text{m}$ , where Fig. 4.10 is representative of a path length difference of 28.05 $\mu\text{m}$  or 27.65 $\mu\text{m}$ . Experimental data also showed plots that contained maxima and minima of the sinusoidal curve. Output data of this nature is more difficult to interpret because a maxima or minima in an output curve allows for two temperature possibilities for a single intensity point.

By varying the wavelength, via a tunable wavelength source, the phase II extinction ratio and propagation loss were found. The extinction ratio was found by increasing the wavelength in increments of 0.1nm from 1500nm to 1570nm and taking data average at each point. The extinction ratio was found to be 87%, though this extinction ratio is not nearly as good as those

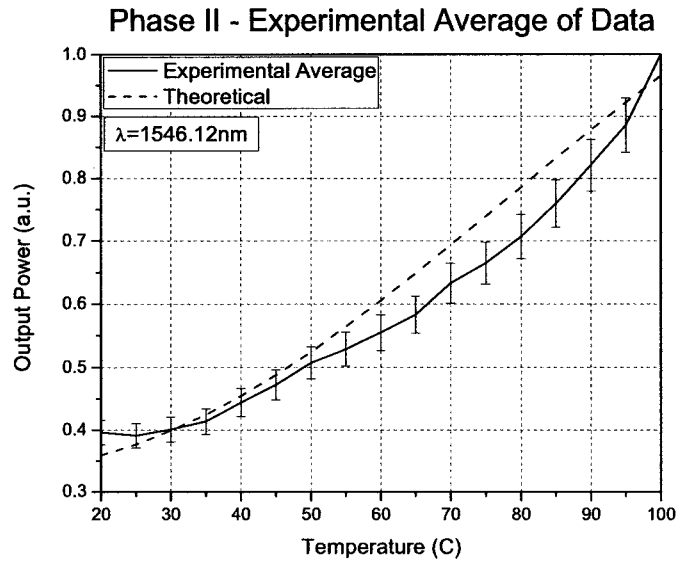


Figure 4.9: Phase II Experimental Data Type 1 - Normalized

found for the phase I design. The propagation loss of the phase II design was found by wavelength tuning in 0.001nm increments from 1550nm to 1551nm, and utilizing the Fabry-Perot Resonance method as described in reference [30, pp.93]. The propagation loss of the phase II design was found to be in the range of 3.5dB/cm to 4.5dB/cm. A contributing factor to the loss of the phase II design is believed to be the extra splitting arm which contains an inherent loss due to modal profile change in the widened section of the splitting arms.

The phase II design, though allowing for self-normalization, did not achieve a greater sensitivity than the phase I design. The accuracy was once again within the range of 1°C and a sensitivity of 0.5°C. The accuracy is limited by fiber alignment due to the expansion of the copper heating

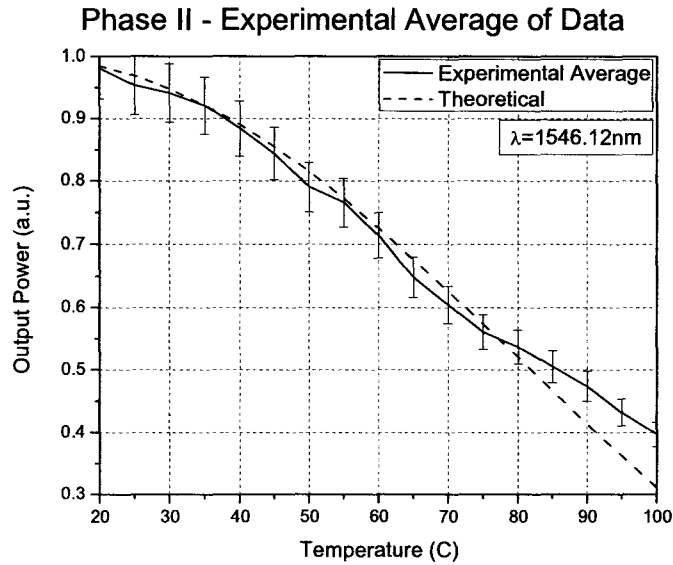


Figure 4.10: Phase II Experimental Data Type 2 - Normalized

block. A manner in which this could be rectified is fiber bonding. A single sample was fiber bonded, and the experimental data is shown in Fig. 4.11. The experimental data show a much smoother curve than the previous experimental figures. The two curves are showing two wavelengths used, to which there is a slight phase shift, which is to be expected.

## 4.2 Asymmetric Mach-Zehnder Fourier Spectrometer

The Asymmetric MZI Fourier Spectrometer represents a different application for the device structure that was originally intended as a vibration sensor. Path length differences of 1.05cm and 3.05cm were utilized for theoretical and experimentation purposes. In order to fully understand the workings of the highly asymmetric MZI a  $1^\circ$  temperature scan was com-

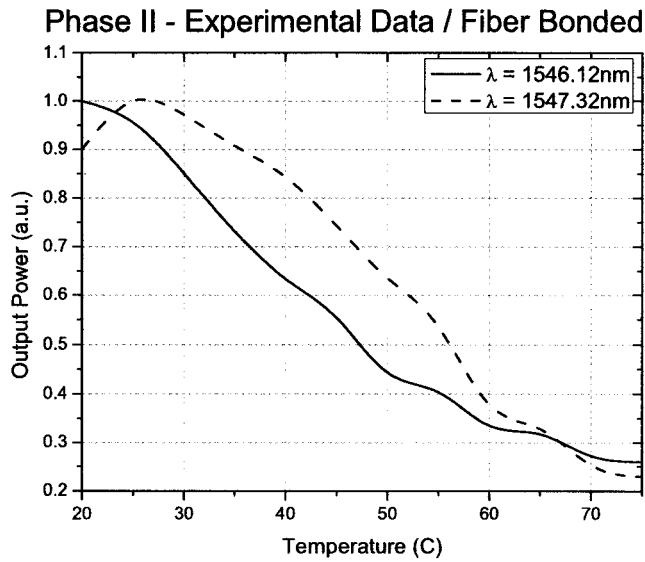


Figure 4.11: Phase II Experimental Data - Fiber Bonded

pleted for both the 1.05cm and 3.05cm  $\Delta L$  MZI. In both cases the theoretical matched exceptionally well with the experimental results, as shown in Fig. 4.12 and Fig. 4.13. The experimental curves were obtained by tuning the temperature via a thermal electric cooler and thermistor, which was driven by a Newport TEC controller. An important and interesting observation is the small offset in the TE and TM polarized outputs from Fig. 4.13. The very small phase offset is to be expected due to the difference in the effective indices of the TE and TM modes. The importance of Fig. 4.12 and Fig. 4.13 lies in one being able to determine the Nyquist frequency for the purpose of signal analysis via the FFT. The temperature scan of the 1.05cm  $\Delta L$  shows that in order to obtain sufficient data to process an appropriate FFT, a data point must be taken every  $0.45^\circ\text{C}$ , and the 3.05cm

$\Delta L$  requires a data point taken every  $0.15^\circ\text{C}$ . To ensure consistency, data points were taken every  $0.1^\circ\text{C}$  in the experimental analysis of both path length differences.

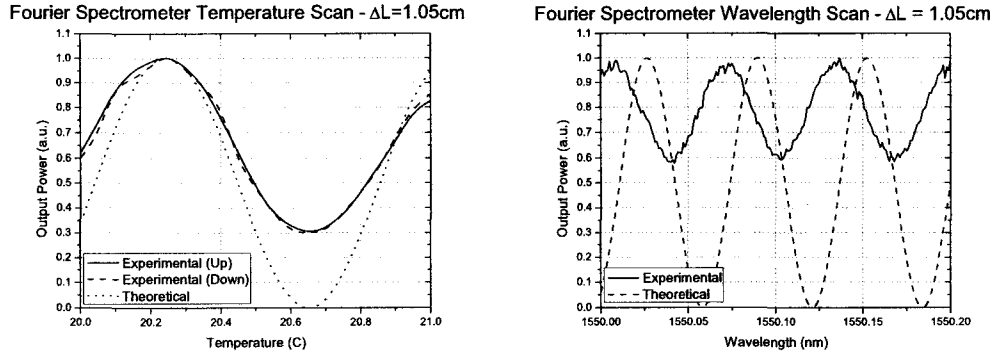


Figure 4.12: High Asymmetry MZI ( $\Delta L = 1.05\text{cm}$ ) - Normalized experimental against theoretical for  $1^\circ$  temperature range and  $0.2\text{nm}$  wavelength scan

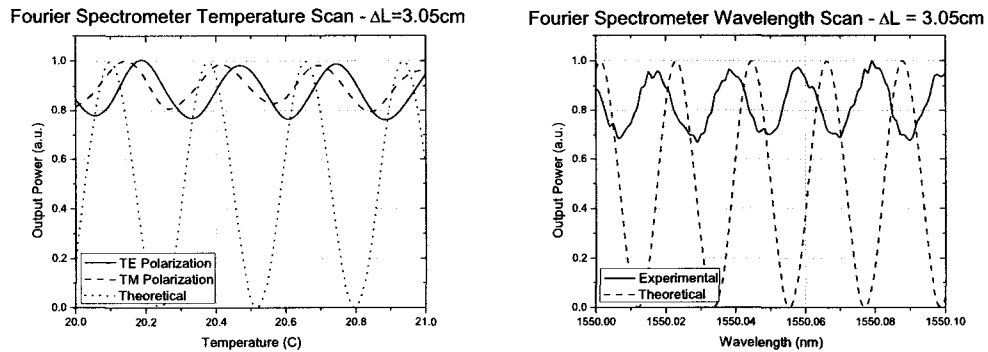


Figure 4.13: High Asymmetry MZI ( $\Delta L = 3.05\text{cm}$ ) - Normalized experimental with polarization against theoretical for  $1^\circ$  temperature range and  $0.1\text{nm}$  wavelength scan

One might note the extinction ratio's contained in Fig. 4.12 are similar, though not exact to each other and yet much smaller than those of the phase II temperature sensor. The reasoning behind this is the extra distance the long arm signal must travel with comparison to the short arm signal. The

longer path of one arm will cause greater attenuation, which in turn lessens the power upon recombination at the output Y-branch. The power ratio upon recombination will therefore not be 50/50 and hence the extinction ratio is lessened. The same problem is worse when  $\Delta L = 3.05\text{cm}$ . In both cases, if propagation losses could be made negligible, the output signal would be in better agreement with the theoretical output as shown in Fig. 4.12 and Fig. 4.13. The theoretical curves in these figures were generated using equation 1.3. Experimentally a temperature point was taken every  $0.1^\circ\text{C}$  and in the case of Fig. 4.13, TE and TM polarization's were isolated. Theoretical curves with horizontal axis labeled wavelength used equation 1.3, though in this case the wavelength is varied, which causes a change in  $k_o$  and  $n(\lambda)$ . Experimentally the wavelength analysis is performed using a laser with wavelength tuning from 1500nm to 1570nm, with a precision of 0.001nm

The MZI Fourier spectrometer has a theoretical output as shown in Fig. 4.14 for a  $\Delta L$  of 1.05cm and a temperature range of  $40^\circ\text{C}$  for two input wavelengths of 1546.12nm and 1562.68nm. Fig. 4.14 contains three separate graphs which are: the input wavelengths, the output interference spectrum with temperature variation, and the FFT of the interference spectrum. The theoretical analysis shows that for this path length difference and temperature range, there is only a single resolvable peak, which is centered at FFT bin number 64. However, for the  $\Delta L$  of 3.05cm, there are two

resolvable peaks in the FFT, which correspond to the two input wavelengths of 1546.12nm and 1564.68nm.

The main peaks of the FFT for each  $\Delta L$  is zero buffered, which is a means to smooth data as well as extract underlying data. By appending zeros to the actual data set, to a number  $2^N$ , the FFT is more able to extract and resolve raw data. Furthermore, by appending zeros to the raw data set one is able to reduce the spacing between frequency bins and thus create a FFT spectrum which has greater density and precision without distorting the data itself, as shown in appendix C.

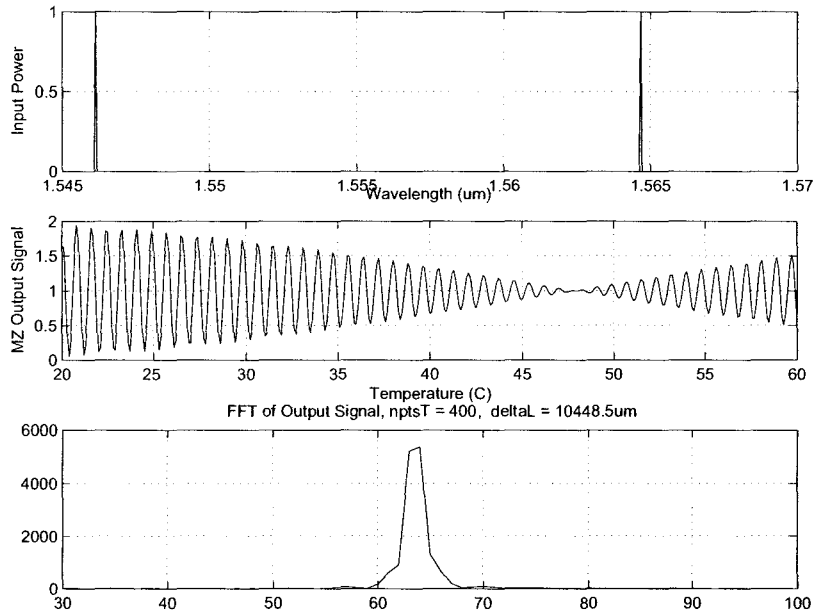


Figure 4.14: High Asymmetry MZI ( $\Delta L = 1.05\text{cm}$ ) - Theoretical FFT output for  $\lambda=1546.12\text{nm}$  and  $\lambda=1564.68\text{nm}$ . Top - Input Wavelengths / Center - Output Interference Spectrum / Bottom - FFT of Output Interference Spectrum

The experimental result of both path length differences aligns well with that of the theoretical. The experimental data analysis for the 1.05cm  $\Delta L$

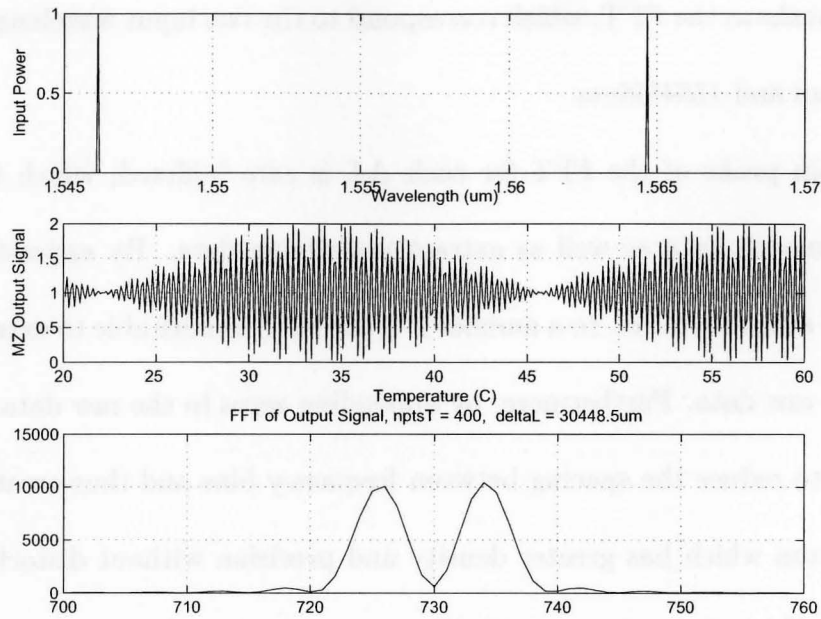


Figure 4.15: High Asymmetry MZI ( $\Delta L = 3.05\text{cm}$ ) - Theoretical FFT output for  $\lambda=1546.12\text{nm}$  and  $\lambda=1564.68\text{nm}$ . Top - Input Wavelengths / Center - Output Interference Spectrum / Bottom - FFT of Output Interference Spectrum

is shown in Fig. 4.16, in which the central peak is at FFT bin number 64, as is with the theoretical. However, as explained in section 2.5.1 the bin numbers for wavelengths 1546.12nm and 1564.68nm are given as 64.2 and 63.5, respectively, which are not resolvable. It is due to this inability to resolve the bin numbers that one is only able to see a single peak from the 1.05cm  $\Delta L$  MZI with a temperature range of  $40^\circ$ . If equation 2.87 is used to analyze the experimental peak with bin number 64, it can be found that the corresponding wavelength is 1551.4nm, which sits between the actual wavelengths used.

The experimental and theoretical results for  $\Delta L$  equal to 3.05cm is shown in Fig. 4.17 and Fig. 4.15, respectively. Although the experimental

and theoretical do not align overly well, the experimental output is reasonably consistent within itself. Again, in following with the arguments made in section 2.5.1, the bin numbers or FFT frequency for wavelengths 1546.12nm and 1564.68nm are 733.24 and 725.54, respectively for theoretical data. The FFT bin numbers correspond to the input wavelengths by using equation 2.87. The experimental peaks found in Fig. 4.17 are 740 and 760, which correspond to wavelengths 1534.6nm and 1494.2nm respectively.

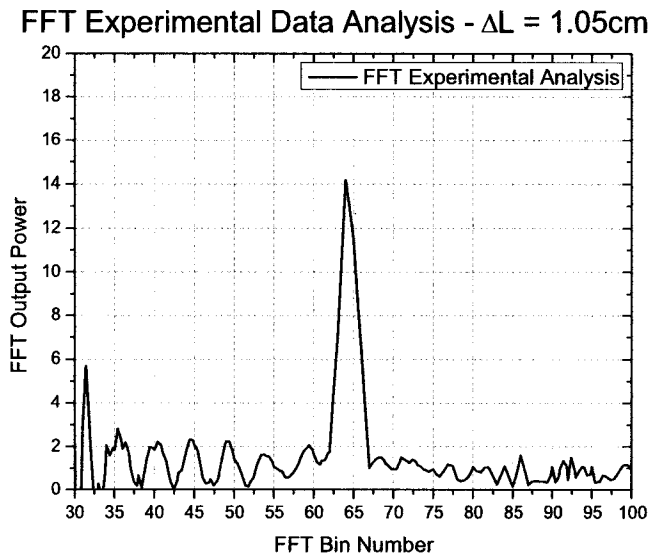


Figure 4.16: High Asymmetry MZI ( $\Delta L = 1.05\text{cm}$ ) - Experimental FFT output for  $\lambda=1546.12\text{nm}$  and  $\lambda=1564.68\text{nm}$

Although the Fourier Spectrometer based on highly asymmetric MZIs was not completely successful in matching theory to experimentation, a basis of operation has been shown. In order to improve this device a larger  $\Delta L$  or larger  $\Delta T$  would be highly desirable, which would allow for greater resolution. Based on the small temperature variation used for initial analysis

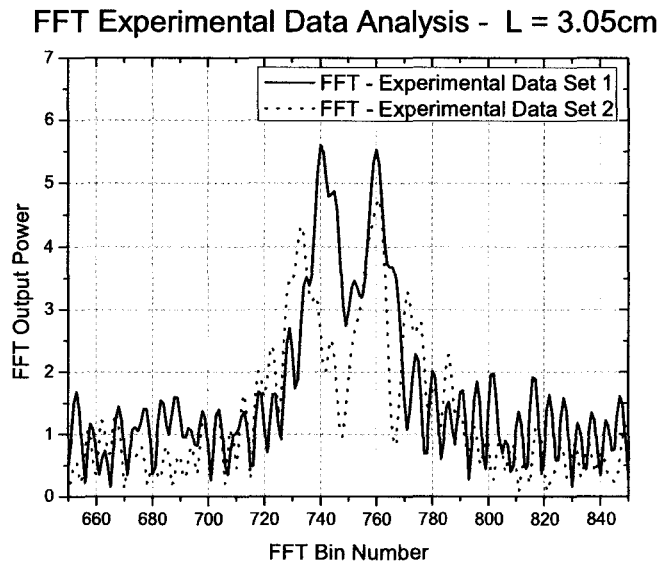


Figure 4.17: High Asymmetry MZI ( $\Delta L = 3.05\text{cm}$ ) - Experimental FFT output for  $\lambda=1546.12\text{nm}$  and  $\lambda=1564.68\text{nm}$

(Fig. 4.12 and Fig. 4.13), the high asymmetry MZIs could be utilized as a small range temperature sensor, which would have an accuracy of  $0.1^\circ\text{C}$  and a sensitivity of  $0.05^\circ\text{C}$ .

A theoretical analysis was done to compare a titanium in-diffused  $\text{LiNbO}_3$  ( $\text{Ti:LiNbO}_3$ ) based MZI as a Fourier Spectrometer. The  $\text{Ti:LiNbO}_3$  MZI is assumed to be symmetric. One arm will be acted upon by an electric field along the  $r_{33}$  direction to induce the greatest refractive index change due to the electro-optic effect, which is  $30.8 \times 10^{-12}\text{m/V}$  [30, p.99]. The index change caused by the electro-optic of Pockels effect is shown in equation 4.1, where  $E$  is the electric field. In the case of a symmetric MZI, the physical path length is the same, however, intensity modulation will occur if one can

change the optical path length of one arm.

$$\Delta n = r_{33}n_{33}^3 \frac{E}{2} \quad (4.1)$$

Investigation revealed that the greatest change in refractive index is  $1.6 \times 10^{-3}$  because this is the breakdown electric field of  $\text{LiNbO}_3$ , which corresponds to a field of  $\frac{10V}{\mu m}$  [31, p.103].

The electric field breakdown of  $\text{LiNbO}_3$  puts a limitation on the possible index change in turn causing limitations on the resolution of the spectrometer device. In order to achieve appropriate resolution for two wavelengths of 1546nm and 1564nm, the active region of the MZI must be to the order of 5cm to 10cm in length, which are impractical dimensions for a device of this nature.

### 4.3 Polarizer on SOI Rib Waveguide

The rib waveguide polarizer was not successful due to an inability to process the materials in an appropriate manner. Aluminum was evaporated onto the sample after the rib waveguides had been fabricated. In order to remove the aluminum from all locations, nay the ribs, the initial photomask was used again, which required an initial alignment of  $2\mu m$  chromium mask lines onto  $2\mu m$  etched ribs. It is assumed that there was a slight misalignment, for the metal clad ribs did not act as theory stated. Theoretically the TE mode was to propagate with little to no loss, while the TM mode was to

be attenuated rapidly with respect to cladding length. However, as shown in Fig. 4.18 and Fig. 4.19, the following does not hold true. Polarization was set via the use of polarization paddles. Measurements were taken by measuring output power with no post sample polarizer, then with the post sample polarizer set to TM, then TE throughput.

Fig. 4.18 depicts a TM input polarization, which at the output is a composition of a mainly TM, though a slight amount of TE. The total power as well as TM power decays as expected due to the increasing metal cladding lengths. However, when the data is normalized it becomes apparent that the amount of TM throughput with regards to the total power is actually increasing, while that of the TE continues to decrease.

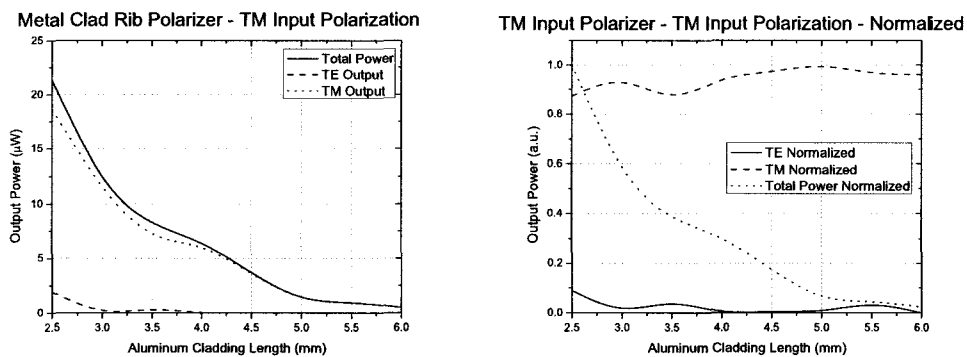


Figure 4.18: Aluminum Clad Rib Polarizer - TM Input and TM Input Normalized

Investigation of Fig. 4.18 depicts a circumstance which is completely undesirable, for the TE polarized mode is to remain relatively stable as the aluminum cladding length increased. However, it is very apparent that TE polarized component of the total, TE input polarized, signal is decreasing

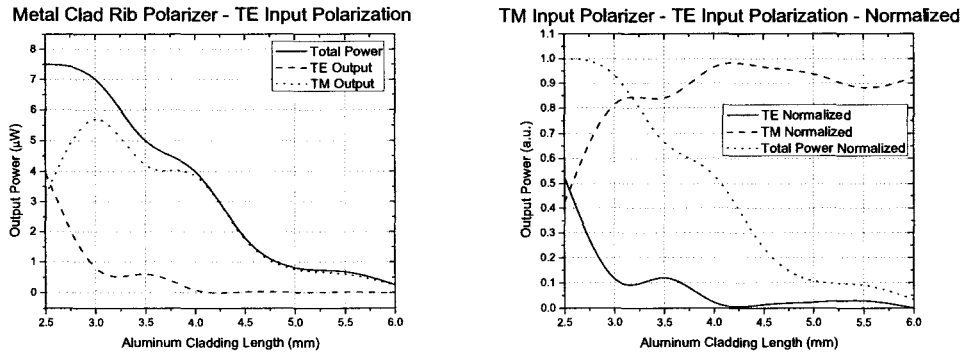


Figure 4.19: Aluminum Clad Rib Polarizer - TE Input and TE Input Normalized

at a much faster rate than that of the TM component. The normalized plot in Fig. 4.19 shows that the normalized TM power is increasing with respect to the total output power. This suggests that the metal cladding is attenuating both the TE and TM polarizations. However, the TE input is rotating the relative polarization power to TM. These peculiar results are believed to be caused by a strain induced birefringence due to an aluminum film remaining on the sides of the rib as opposed to only the top.

## Chapter 5

---

# Conclusion and Future Work

---

An interference based temperature sensor was designed and fabricated in SOI. The optical path length difference in an asymmetric MZI varies due to a change in refractive index with respect to temperature. Upon recombination, there will be a temperature dependent phase difference, which in turn causes constructive or destructive phase interference. The intensity modulation due to phase difference allows for a measurable and repeatable output power variation with respect to temperature. Two designs were fabricated, which are noted as Phase I and Phase II. The phase I design contained four MZI designs of  $\Delta L$   $2.54\mu\text{m}$ ,  $10.5\mu\text{m}$ ,  $23.46\mu\text{m}$ , and  $37.23\mu\text{m}$ . The phase II design had a single  $\Delta L$  of  $27.85\mu\text{m}$  and had the advantage of being self normalizing.

A Mach-Zehnder was also designed to act as a vibration sensor. Harmonic vibration along straight sections of a highly asymmetric MZI would induce a strain field within the arms and thereby induce the photoelastic

effect. In essence, the sensor measures strain, though it is believed that vibration could be monitored due to the inherent acceleration and harmonic nature of a vibrating system. However, no experimental data was collected on the vibration sensor. In order to obtain a data set, three asymmetry factors were fabricated, which were 1.05cm, 2.04cm, and 3.05cm.

The vibration sensor was not tested experimentally, though the devices were fabricated. The devices, however, were used to test a proof of concept for a Fourier spectrometer. By changing the temperature of the MZI an interference pattern could be found. This interference pattern consisted of one or two signals undergoing phase modulation, and summing to a single intensity signal. This intensity signal was then processed by zero buffering then FFT analysis.

The temperature sensor was designed such that the signal would follow, at most, a  $\pi/2$  traversal of a cosine signal with no maxima or minima in the curve, which would give rise to a monotonic response of intensity with respect to temperature. The average temperature accuracy of the phase I design was  $2^{\circ}\text{C}$  for a  $\Delta L$  of  $23.46\mu\text{m}$ , and around  $1^{\circ}\text{C}$  for a  $\Delta L$  of  $37.23\mu\text{m}$  with a sensitivity of  $0.5^{\circ}\text{C}$ . The measurable temperature range was from  $20\text{-}100^{\circ}\text{C}$  due to experimental limitations. The phase II temperature sensor was a changed design, in that the desired range was from  $0\text{-}120^{\circ}\text{C}$ , though once again the experimental range was from  $20\text{-}100^{\circ}\text{C}$ . The accuracy of the phase II design was  $1^{\circ}\text{C}$  for  $\Delta L$  of  $27.85\mu\text{m}$ , with a sensitivity of  $0.5^{\circ}\text{C}$ .

One sample of the phase II design was fiber bonded at the input in an attempt to decrease thermal drift. The accuracy of the fiber bonded sample was 0.5-1°C. To increase accuracy and sensitivity, a design with a desired temperature range of 10-100°C would be beneficial. However, from the standpoint of industrial design the sample would need be fiber bonded, which in turn would negate drift and hence increase temperature accuracy.

An improved temperature sensor design could use a device already fabricated, as shown in appendix D, Fig. D.2. The highly asymmetric MZI boast a temperature accuracy of 0.1°C and a sensitivity of 0.05°C, though the dynamic range is limited to around 1°C due to an inability to determine fringe points. With further investigation one could incorporate both the  $\Delta L$  of 27.85 $\mu\text{m}$  MZI and the  $\Delta L$  of 1.05cm MZI to be used as a single device. Being that a  $\Delta L$  of 1.05cm would have hundreds of fringes for a 100°C temperature scan, it alone is not practical as a large range temperature sensor. However, one could use the 27.85 $\mu\text{m}$  MZI as a fringe marker. By utilizing both MZI devices, one is able to know the fringe number, and hence the temperature point while having the greater accuracy and sensitivity of the highly asymmetric MZI.

The Fourier Spectrometer made use of devices that were not specifically designed for that purpose and hence the MZI dimensions were not optimized. The experimental results did not match exactly with the theoretical, though the experimental results were reproducible across a number

of samples. The MZI with a  $\Delta L$  of 1.05cm was not able to resolve two wavelengths of 1546.12nm and 1564.68nm with a temperature scan of 40°C, though this was shown theoretically as well. However, the FFT analysis did show an experimental peak at FFT bin number 64, which corresponds to the theoretical MatLab FFT output bin number 64. The larger  $\Delta L$  of 3.05cm was able to resolve the two above mentioned wavelengths, though the experimental did not align with the theoretical. The experimental showed peaks at FFT frequency of 740 and 760, where the theoretical showed the resolvable peaks at 725 and 735. This suggests that there was a FFT frequency shift in the experimental as well as a two fold expansion in the peak to peak distance. However, the experimental data does show a proof of concept, though slightly skewed. To better the design, a larger  $\Delta L$  of 5cm would be advantageous. As well, a fiber bonded system, in which measurements are taken via Labview would allow for greater accuracy and less human interference. The highly asymmetric MZI designs with  $\Delta L$  of 1.05cm, 2.04cm, and 3.05cm did show great sensitivity to temperature response within a temperature range of 1°C with a accuracy of 0.1°C and a sensitivity of 0.05°C.

---

# Bibliography

---

- [1] L.Pavesi and D.J.Lockwood. *Topics in Applied Physics: Silicon Photonics*. Springer, Berlin Germany, 2004. [cited at p. iii, 10, 11, 22]
  
- [2] Frank L.Pedrotti and Leno S.Pedrotti. *Introduction to Optics*. Prentice-Hall, Inc., Upper Saddle River, New Jersey, 2nd edition, 1993. [cited at p. iii, 7, 14, 27, 60, 64]
  
- [3] L.Liao, D.Samara-Rubio, M.Morse, A.Liu, D.Hodge, D.Rubin, U.D.Keil, and T.Franck. High speed silicon mach-zehnder modulation. *Optics Express*, 13:3129–3135, April 2005. [cited at p. 2]
  
- [4] A.Irace and G.Breglio. All-silicon temperature sensor based on multi-mode interference. *Optics Express*, 11:2807–2812, November 2003. [cited at p. 2]
  
- [5] F.Prieto, B.Sepulveda, A.Calle, A.Llobera, C.Dominguez, and L.M.Lechuga. Integrated mach-zehnder interferometer based on arrow structures for biosensor applications. *Sensors and Actuators B*, 92:151–158, January 2003. [cited at p. 2]

- [6] R. Bernini and A. Cusano. Generalized mach-zehnder interferometers for sensing applications. *Sensors and Actuators B*, 100:72–74, February 2004. [cited at p. 2]
- [7] T. Ma, W. Zhaob, and J. Liuac. A mems vibration sensor based on mach zehnder interferometers. *Proc. of SPIE*, 6529, 2007. [cited at p. 3]
- [8] Safa O. Kasp. *Optoelectronic Devices and Photonics, Principles and Practices*. Prentice-Hall, Inc., Upper Saddle River, New Jersey, 2001. [cited at p. 7]
- [9] H. H. Li. Refractive index of silicon and germanium and its wavelength and temperature derivatives. *Journal of Physical and Chemical Reference Data*, 9(3):561–658, 1980. [cited at p. 8]
- [10] INSPEC. *Properties of Crystalline Silicon*. INSPEC, The Institution of Electrical Engineers, Six Hills Way, Stevenage, United Kingdom, 1999. [cited at p. 8, 9, 11, 22]
- [11] INSPEC. *Properties of Amorphous Silicon and its Alloys*. INSPEC, The Institution of Electrical Engineers, Six Hills Way, Stevenage, United Kingdom, 1998. [cited at p. 9]
- [12] INSPEC. *Properties of Porous Silicon*. INSPEC, The Institution of Electrical Engineers, Six Hills Way, Stevenage, United Kingdom, 1997. [cited at p. 9]
- [13] J. F. Nye. *Physical Properties of Crystals: Their Representation by Tensors and Matrices*. Oxford Scientific Publications, Walton Street Oxford, 1992. [cited at p. 12]

- [14] E.Peiner, D.Scholz, A.Schlachetzki, and P.Hauptmann. A micromachined vibration sensor based on the controle of power transmitted between optical fibers. *Sensors and Actuators A*, 65:23–29, 1998. [cited at p. 17]
- [15] Roark. *Roark's Formulas for Stress and Strain*. McGraw-Hill, Great Britain, 338 Euston Road, London NW1 3BH, 2004. [cited at p. 19]
- [16] C.F.Beards. *Structural Vibration: Analysis and Damping*. Arnold, Great Britain, 338 Euston Road, London NW1 3BH, 2nd edition, 1996. [cited at p. 19]
- [17] Graham Woan. *The Cambridge Handbook of Physics Formulas*. Cambridge University Press, The Edinburgh Building, Cambridge, CB2 2RU, UK, 2000. [cited at p. 19]
- [18] J.Kalenik and R.Pajak. A cantilever optical-fiber accelerometer. *Sensors and Actuators A*, 68:350–355, 1998. [cited at p. 20]
- [19] M.Kimura and K.Toshima. Vibration sensor using optical-fiber cantilever with bulb-lens. *Sensors and Actuators A*, 66:178–183, 1998. [cited at p. 20]
- [20] S.M.Sze and K.K.Ng. *Physics of Semiconductor Devices*. John Wiley and Sons Inc., Hoboken, NewJersey, 3rd edition, 2007. [cited at p. 22, 23]
- [21] S.K.Ramesh and K.C.Wong. Design and fabrication of a fiber bragg grating temperature sensor. *SPIE Conference on Int. Opt. Devices III*, 3620:338–344, 1999. [cited at p. 26]

- [22] V.N.Protopopov, V.I.Karpova, O.I.Medvedkova, S.A.Vasilieva, M.V.Grekov, E.M. Djova, and S.P.Paltob. Temperature sensor based on fiber bragg grating. *Proceedings of SPIE*, 4083:224–228, 2000. [cited at p. 26]
- [23] Pochi Yeh. *Optical Waves in Layered Media*. John Wiley and Sons Inc., Hoboken, NewJersey, 2005. [cited at p. 32, 34, 64]
- [24] O.Powell. Single-mode condition for silicon rib waveguides. *J. Lightwave Technologies*, 20(10):1851–1855, 2002. [cited at p. 43, 45]
- [25] R.A.Soref, J.Schmidtchen, and K.Petermann. Large single-mode rib waveguides in gesi-si and si-on-so<sub>2</sub>. *IEEE J. Quantum Electronics*, 27(8):1971–1974, 1991. [cited at p. 45]
- [26] S.P.Pogossian, L.Vescan, and A.Vonsovici. The single-mode condition for semiconductor rib waveguides with large cross section. *J. Lightwave Technologies*, 16(10):1851–1853, 1998. [cited at p. 45]
- [27] J.Lousteau, D.Furniss, A.B.Seddon, T.M.Benson, A.Vukovic, and P. Sewell. The single-mode condition for silicon-on-insulator optical rib waveguides with large cross section. *J. Lightwave Technologies*, 22(8):1923–1929, 2004. [cited at p. 45]
- [28] K.Kawano and T.Kitoh. *An Introduction to Optical Waveguide Analysis: Solving Maxwell's Equations and the Schrodinger Equation*. John Wiley and Sons Inc., 605 Third Ave New York NY, 2001. [cited at p. 48]

- [29] C.Yuanyuan, Y.Qingfeng, Y.Di, C.Shaowu, and Y.Jinzhong. Structural optimization of soi-based single-mode rib waveguide bends. *IEEE*, pages 2015–2017, 2004. [cited at p. 51, 57, 58, 123]
- [30] A.P.Knights and G.T.Reed. *Silicon Photonics: An Introduction*. John Wiley and Sons Inc., West Sussex England, 2004. [cited at p. 52, 93, 97, 105]
- [31] H.Nishihara, M.Haruna, and T.Suhara. *Optical Integrated Circuits*. McGraw-Hill, NewYork USA, 1989. [cited at p. 53, 64, 106]
- [32] R.Halir, A.Ortega-Monux, J.G.Wanguemert-Perez, I.Molina-Fernandez, and P.Cheben. Fabrication tolerance analysis of bent single-mode rib waveguides on soi. *Optical and Quantum Electronics*, 38:921–932, 2007. [cited at p. 54]
- [33] V.Subramaniam, G.N.De Brabander, D.H.Naghski, and J.T.Boyd. Measurement of mode field profiles and bending and transition losses in curved optical channel waveguides. *J. Lightwave Technology*, 15(6):990–997, 1997. [cited at p. 54]
- [34] Donald L.Lee. *Electromagnetic Principles of Integrated Optics*. John Wiley and Sons, Toronto Canada, 1986. [cited at p. 56, 124]
- [35] E.A.J.Marcatili. Bends in optical dielectric guides. *Bell Syst.Tech.J.*, 48:2103–2132, 1969. [cited at p. 56]
- [36] D.Marcuse. *Light Transmission Optics*. Krieger Pub Co., 1972. [cited at p. 57]

- [37] Graham N.Pearson. *Temperature-Insensitive Mach-Zehnder Interferometer Strain Senso in Silicon-On-Insulator (M.Sc Thesis)*. McMaster University, Hamilton, Ontario, 2003. [cited at p. 58]
- [38] J.J.Wortman and R.A.Evans. Young's modulus, shear modulus, and poisson's ratio in silicon and germanium. *J. Applied Optics*, 36(1):153–156, 1965. [cited at p. 59]
- [39] M.Gottlieb. *Elastoplastic Materials, CRC handbook of laser science and technology*. CRC Press, 1986. [cited at p. 59]
- [40] G.N.DeBrabander, J.T.Boyd, and H.E.Jackson. Single polarization optical waveguide on silicon. *IEEE*, 27(3):575–579, 1991. [cited at p. 64]
- [41] V.L.Gupta, E.K.Sharma, K.N.Tripathi, and G.P.Srivastava. Rib waveguide polarizer in gaas/algaas. *Kodaikanal Obs.Bull*, 11:99–104, 1991. [cited at p. 64]
- [42] I.P.Kaminow, W.L.Mammel, and H.P.Weber. Metal-clad optical waveguides: Analytical and experimental study. *Applied Optics*, 3(2):396–405, 1974. [cited at p. 64]
- [43] T.Hayakawa, T.Suzuki, T.Uesugi, and Y.Mitsushima. Mechanism of residue formation in silicon trench etching using a bromine-based plasma. *Jpn. J. Appl. Phys*, 37:5–9, 1998. [cited at p. 79]
- [44] S.Roberts and P.J.Dobson. Evidence for reaction at the al-sio<sub>2</sub> interface. *J. Phys. D: Appl. Phys*, 14:L17–L22, 1981. [cited at p. 83]

# Appendices



## Appendix A

---

# Maple Programs

---

Programs Designed and Implemented on Maple 11. However, should be easily converted to earlier versions of maple with few disasters.

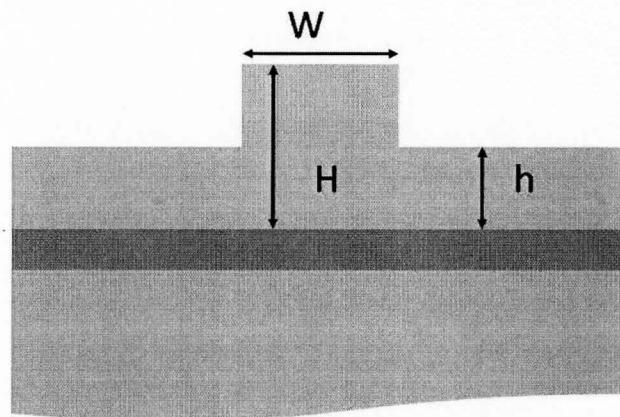


Figure A.1: Cross Section of Rib Waveguide With Geometric Variables

## A.1 Single Mode Condition

Initially it is desirable to set up the initial conditions that will govern the geometry as well as the material values of the rib waveguide. Values correspond to those in figure A.1, and are a preamble to all following programs. The following has been designed for a single mode SOI rib waveguide, though the geometric and material parameters can easily be changed.

\*

### Geometry, Material, and Wavelength Conditions for Silicon

$n[cover] := 1.0;$	Refractive Index of Cover (air in most cases)
$n[slab] := 3.562;$	Refractive Index of Slab Region (Si)
$n[insulator] := 1.47;$	Refractive Index of Insulator (SiO <sub>2</sub> )
$H := 2.5E - 6;$	Height of Rib
$h := 1.5E - 6;$	Height of Slab
$w := 2.0E - 6;$	Width of Rib
$\lambda := 1.55E - 6;$	Wavelength to be used

### Single Mode Program

$\alpha[s] := 0.3;$	fitting constant
$evalb(\frac{w}{H} \leq \alpha[s] + \frac{\frac{h}{H}}{sqrt(1-(\frac{h}{H})^2)});$	Condition 1
$evalb(\frac{h}{H} \geq 0.5);$	Condition 2

The program will give forth a TRUE or FALSE answer depending on the geometry chosen. If either condition 1 or condition 2 gives a FALSE answer, the waveguide will most likely not be single mode. The  $\alpha[s]$  constant is set up in a manner that the user can choose values of -0.05, 0.0, or 0.3, depending on what is desired, and which author one chooses to follow.

## A.2 Effective Index Method

The effective index calculation has been customized from reference [29]. The values depicted are not as exact as the actual EIM, though for structural analysis they are an excellent basis of design. Again, ensure to implement the preamble information at the beginning. The process is as follows.

### Cross Section (Vertical) Effective Index in Slab / Rib Region

$$N[I] := \text{evalf}\left(\sqrt{n[\text{slab}]^2 - \frac{\pi^2}{\left(\frac{2 \cdot \pi \cdot H}{\lambda} + \frac{2}{\sqrt{n[\text{slab}]^2 - n[\text{insulator}]^2}}\right)^2}}\right);$$

Effective index of rib

$$N[II] := \text{evalf}\left(\sqrt{n[\text{slab}]^2 - \frac{\pi^2}{\left(\frac{2 \cdot \pi \cdot h}{\lambda} + \frac{2}{\sqrt{n[\text{slab}]^2 - n[\text{insulator}]^2}}\right)^2}}\right);$$

Effective index of Slab

**Required Variables to be Found**

$$b[I] := \frac{N[I]^2 - n[\text{insulator}]^2}{n[\text{slab}]^2 - n[\text{insulator}]^2}; \quad \text{Guided Index in Rib}$$

$$b[I] := \frac{N[II]^2 - n[\text{insulator}]^2}{n[\text{slab}]^2 - n[\text{insulator}]^2}; \quad \text{Guided Index in Slab}$$

$$V[\gamma] := \text{evalf}\left(\frac{2\pi}{\lambda} \cdot w \cdot \sqrt{N[I]^2 - N[II]^2}\right); \quad \text{Normalized Rib Width}$$

$$a[TE] := \frac{N[II] - n[\text{cover}]}{N[I] - N[II]}; \quad \text{Asymmetry in TE plane (horizontal)}$$

$$a[TM] := \left(\frac{N[I]}{n[\text{cover}]}\right)^2 \cdot a[TE]; \quad \text{Asymmetry in TM plane (vertical)}$$

$$V[\gamma] \cdot \sqrt{1 - b[TE]} = \arctan\left(\sqrt{\frac{b[TE]}{1 - b[TE]}}\right) + \arctan\left(\sqrt{\frac{b[TE] + a[TE]}{1 - b[TE]}}\right); \quad \text{Dispersion}$$

Curve for TE mode

$$V[\gamma] \cdot \sqrt{1 - b[TM]} = \arctan\left(\sqrt{\frac{b[TM]}{1 - b[TM]}}\right) + \arctan\left(\sqrt{\frac{b[TM] + a[TM]}{1 - b[TM]}}\right); \quad \text{Dispersion}$$

Curve for TM mode

The following required manual rearrangement, however, this portion has been completed.

$$\text{isolate}(\tan(V[\gamma] \cdot \sqrt{1 - b[TE]}) = \sqrt{\frac{b[TE]}{1 - b[TE]}} + \sqrt{\frac{b[TE] + a[TE]}{1 - b[TE]}}); \quad \text{Isolates and}$$

solves value of b[TE]

$$\text{isolate}(\tan(V[\gamma] \cdot \sqrt{1 - b[TM]}) = \sqrt{\frac{b[TM]}{1 - b[TM]}} + \sqrt{\frac{b[TM] + a[TM]}{1 - b[TM]}}); \quad \text{Isolates and}$$

solves value of b[TM]

Both isolate factors will solve for, and find the b values for both the TE and TM modes. For further understanding, look to page 92 of reference [34].

$N[TE] := \sqrt{N[II]^2 + b[TE] \cdot (N[I]^2 - N[II]^2)}$ ; Effective index of TE mode  
(topographical)

$N[TM] := \sqrt{N[II]^2 + b[TM] \cdot (N[I]^2 - N[II]^2)}$ ; Effective index of TM  
mode (topographical)

$\beta[TE] := \text{evalf}(\frac{2\pi}{\lambda} \cdot N[TE])$ ; Propagation Constant TE

$\beta[TM] := \text{evalf}(\frac{2\pi}{\lambda} \cdot N[TM])$ ; Propagation Constant TM

Now the variable of effective index across the rib has been found to be  $N[TE]$  and  $N[TM]$ , furthermore the propagation constants have been found as well. In order to check for correctness of coding, the following simple check should allow for confidence.

$B[TE] := \frac{N[TE]-N[II]}{N[I]-N[II]}$ ; Will equal value previously found for  $b[TE]$

$B[TM] := \frac{N[TM]-N[II]}{N[I]-N[II]}$ ; Will equal value previously found for  $b[TE]$

## A.3 Bend Loss

The Following program will give the appropriate bend loss coefficients and bend radius loss, though in order to properly run the program, the previous program for effective index calculations must be implemented first. Also, the initial preamble information need be set up with exact script as shown

above with regards to material and geometric variables. Throughout all programs, the variable have been kept the same. The original program implements all three in a single run, however one may net feel the desire to execute any one of the three.

To begin, run the EIM program, ensuring to maintain all variables in the appropriate format.

### Marcuse via Journal

It was found that a separate journals had interpreted the bend loss found by

Marcuse in separate manners. Both will be shown.  $k_{TE} := evalf(\sqrt{(\frac{2\cdot\pi}{\lambda})^2 \cdot N[I]^2 - \beta_{TE}^2})$ ;

TE Rib propagation constant

$$k_{TM} := evalf(\sqrt{(\frac{2\cdot\pi}{\lambda})^2 \cdot N[I]^2 - \beta_{TM}^2}); \quad \text{TM rib propagation constant}$$

$$p_{TE} := evalf(\sqrt{\beta_{TE}^2 - \frac{2\cdot\pi^2}{\lambda}}N[II]^2); \quad \text{TE Slab propagation constant}$$

$$p_{TM} := evalf(\sqrt{\beta_{TM}^2 - \frac{2\cdot\pi^2}{\lambda}}N[II]^2); \quad \text{TM Slab propagation constant}$$

$$C[1-Marcuse-a_{TE}] := evalf\left(\frac{p_{TE}^2 \cdot k_{TE}^2 \exp 2 \cdot p_{TE} \cdot w}{2(\frac{2\cdot\pi}{\lambda})^2 \cdot (N[I]^2 - N[II]^2) \cdot \beta_{TE} \cdot (1 + p_{TE} \cdot w)}\right);$$

TE Constant for bend loss

$$C[1-Marcuse-a_{TM}] := evalf\left(\frac{p_{TM}^2 \cdot k_{TM}^2 \exp 2 \cdot p_{TM} \cdot w}{2(\frac{2\cdot\pi}{\lambda})^2 \cdot (N[I]^2 - N[II]^2) \cdot \beta_{TM} \cdot (1 + p_{TM} \cdot w)}\right);$$

TM Constant for bend loss

$$C[2 - Marcuse - a_{TE}] := \frac{2p_{TE}^3}{3\beta_{TE}^2}; \text{ TE Constant for bend loss}$$

$$C[2 - Marcuse - a_{TM}] := \frac{2p_{TM}^3}{3\beta_{TM}^2}; \text{ TM Constant for bend loss}$$

$\alpha[Marcuse - a_{TE}] := C[1 - Marcuse - a_{TE}] \exp(-C[2 - Marcuse - a_{TE}] \cdot R \cdot 0.001)$ ; TE Bend Loss in  $\text{cm}^{-1}$ .

$\alpha[Marcuse - a_{TE} - DB] := 10 \cdot \log_{10}(\frac{\alpha[Marcuse - a_{TE}] \cdot R \cdot 0.001 \pi}{2})$ ; TE Bend Loss in  $\text{dB}/90^\circ$

$\alpha[Marcuse - a_{TM}] := C[1 - Marcuse - a_{TM}] \exp(-C[2 - Marcuse - a_{TM}] \cdot R \cdot 0.001)$ ; TM Bend Loss in  $\text{cm}^{-1}$ .

$\alpha[Marcuse - a_{TM} - DB] := 10 \cdot \log_{10}(\frac{\alpha[Marcuse - a_{TM}] \cdot R \cdot 0.001 \pi}{2})$ ; TM Bend Loss in  $\text{dB}/90^\circ$

plot([0.1E-1· $\alpha[Marcuse - a_{TE}]$ , 0.1E-1· $\alpha[Marcuse - a_{TM}]$ ], R = 0 .. 3, 0 .. 10, title = "Bend Loss Calculations Marcuse-Journal", labels = ["Radius (mm)", "Bend Loss Coefficient (mm-1)"], la belldirections = [HORIZONTAL, VERTICAL], legend = ["TE", "TM"], axes = BOXED, thickness = 1, resolution = 5000, numpoints = 1000, gridlines); Plots loss coefficient  $\alpha$  in  $\text{mm}^{-1}$  vs Bend Radius in mm.

plot([ $\alpha[Marcuse - a_{TE} - DB]$ ,  $\alpha[Marcuse - a_{TM} - DB]$ ], R = 0 .. 2, 0 .. 300, title = "Bend Loss Calculations Marcuse-Journal", labels = ["Radius (mm)", "Bend Loss Db / 90 degrees"], la belldirections = [HORIZONTAL, VERTICAL], legend = ["TE", "TM"], axes = BOXED, thickness = 1, resolution = 5000, numpoints = 1000, gridlines); Plots loss in  $\text{dB}/90^\circ$  vs Bend radius in mm.

The first plot will give loss in terms of  $\text{mm}^{-1}$  with respect to bend radius in mm for both the TE and TM modes. The second plot will give loss in terms of  $\text{dB}/90^\circ$  with respect to bend radius in mm.

**Marcuse**

$$\alpha x_{TE} := \text{evalf}\left(\frac{2\pi\sqrt{N_{TE}^2 - N[II]^2}}{\lambda}; \quad \text{TE propagation parameter in Rib}$$

$$\alpha x_{TM} := \text{evalf}\left(\frac{2\pi\sqrt{N_{TM}^2 - N[II]^2}}{\lambda}; \quad \text{TM propagation parameter in Rib}$$

$$k[2x_{TE}] := \text{evalf}\left(\frac{2\pi\sqrt{N[I]^2 - N_{TE}^2}}{\lambda}; \quad \text{TE propagation parameter in slab}$$

$$k[2x_{TM}] := \text{evalf}\left(\frac{2\pi\sqrt{N[I]^2 - N_{TM}^2}}{\lambda}; \quad \text{TM propagation parameter in slab}$$

$$C_1[\text{Marcuse}_{TE}] := \text{evalf}\left(\frac{\alpha x_{TE}^2 k[2x_{TE}]^2 \exp(\alpha x_{TE} \cdot w)}{\left(\frac{2\pi}{\lambda}\right)^3 \cdot N_{TE} \cdot (N[I]^2 - N[II]^2) \cdot (1 + \alpha x_{TE} \cdot \frac{w}{2})}\right);$$

TE Constant for bend loss

$$C_1[\text{Marcuse}_{TM}] := \text{evalf}\left(\frac{\alpha x_{TM}^2 k[2x_{TM}]^2 \exp \alpha x_{TM} \cdot w}{\left(\frac{2\pi}{\lambda}\right)^3 \cdot N_{TM} \cdot (N[I]^2 - N[II]^2) \cdot (1 + \alpha x_{TM} \cdot \frac{w}{2})}\right);$$

TM Constant for bend loss

$$C_2[\text{Marcuse}_{TE}] := \frac{2\alpha x_{TE}^3}{3\beta_{TE}^2}; \quad \text{TE Constant for bend loss}$$

$$C_2[\text{Marcuse}_{TM}] := \frac{2\alpha x_{TM}^3}{3\beta_{TM}^2}; \quad \text{TM Constant for bend loss}$$

$$\alpha q \text{Marcuse}_{TE} := C_1[\text{Marcuse}_{TE}] \exp(-C_2[\text{Marcuse}_{TE}] \cdot R \cdot 0.001); \quad \text{TE}$$

bend loss in  $\text{cm}^{-1}$ 

$$\alpha q \text{Marcuse}_{TE-DB} := 10 \log_{10}\left(\exp\left(\frac{\alpha q \text{Marcuse}_{TE} \cdot R \cdot 0.001 \pi}{2}\right)\right); \quad \text{TE bend loss in}$$

dB/90°

$$\alpha q \text{Marcuse}_{TM} := C_1[\text{Marcuse}_{TM}] \exp(-C_2[\text{Marcuse}_{TM}] \cdot R \cdot 0.001); \quad \text{TM}$$

bend loss in  $\text{cm}^{-1}$ 

$$\alpha q \text{Marcuse}_{TM-DB} := 10 \log_{10}\left(\exp\left(\frac{\alpha q \text{Marcuse}_{TM} \cdot R \cdot 0.001 \pi}{2}\right)\right); \quad \text{TM bend loss in}$$

dB/90°

plot([0.1E-1· $\alpha$  qMarcuse<sub>TE</sub>, 0.1E-1· $\alpha$  qMarcuse<sub>TM</sub>], R = 0 .. 3, 0 .. 10, legend = ["TE", "TM"], title = "Bend Loss Calculations Marcuse", labels = ["Radius (mm)", "Bend Loss Coefficient (cm-1)"], labeldirections = [HORIZONTAL, VERTICAL], axes = BOXED, thickness = 1, resolution = 5000, numpoints = 1000, gridlines);

plot([ $\alpha$  qMarcuse<sub>TE-DB</sub>, 1 $\alpha$  qMarcuse<sub>TM-DB</sub>], R = 0 .. 5, 0 .. 70, legend = ["TE", "TM"], title = "Bend Loss Calculations Marcuse", labels = ["Radius (mm)", "Bend Loss Db / 90 degrees"], labeldirections = [HORIZONTAL, VERTICAL], axes = BOXED, thickness = 1, resolution = 5000, numpoints = 1000, gridlines);

### Marcatili

$$A_{TE} := evalf(\lambda \cos(\frac{\pi k[2x_{TE}] \cdot w}{180})^2 \exp(\alpha x_{TE} \cdot w)); \quad \text{TE Constant 1}$$

$$A_{TM} := evalf(\lambda \cos(\frac{\pi k[2x_{TM}] \cdot w}{180})^2 \exp(\alpha x_{TM} \cdot w)); \quad \text{TM Constant 1}$$

$$B_{TE} := w^2 \cdot \alpha x_{TE} \cdot N_{TE}; \quad \text{TE Constant 2}$$

$$B_{TM} := w^2 \cdot \alpha x_{TM} \cdot N_{TM}; \quad \text{TM Constant 2}$$

$$C_{TE} := evalf(\frac{w}{2} + \frac{\sin(k[2x_{TE}] \cdot w)}{2 \cdot k[2x_{TE}]} + \frac{\cos(k2x_{TE} \cdot w/2)}{\alpha x_{TE}}); \quad \text{TE Constant 3}$$

$$C_{TM} := evalf(\frac{w}{2} + \frac{\sin(k[2x_{TM}] \cdot w)}{2 \cdot k[2x_{TM}]} + \frac{\cos(k2x_{TM} \cdot w/2)}{\alpha x_{TM}}); \quad \text{TM Constant 3}$$

$$C[1 - Marc_{TE}] := \frac{A_{TE}}{B_{TE} \cdot C_{TE}}; \quad \text{TE Constant relation 1}$$

$$C[1 - Marc_{TM}] := \frac{A_{TM}}{B_{TM} \cdot C_{TM}}; \quad \text{TM Constant relation 1}$$

$$C[2 - Marc_{TE}] := evalf(2 \cdot \alpha x_{TE} (\frac{\lambda \beta_{TE}}{2 \cdot \pi \cdot N[II]} - 1)); \quad \text{TE propagation}$$

relationship

$$C[2 - Marc_{TM}] := evalf(2 \cdot \alpha x_{TM} (\frac{\lambda \beta_{TM}}{2 \cdot \pi \cdot N[II]} - 1)); \quad \text{TM propagation}$$

relationship

$$\alpha Marc_{TE} := C[1 - Marc_{TE}] \exp(-C[2 - Marc_{TE}] \cdot R \cdot 0.001); \quad \text{TE loss in}$$

cm<sup>-1</sup>

$$\alpha Marc_{TE-DB} := 1 - \log_{10}(\exp(\frac{\alpha Marc_{TE} \cdot R \cdot 0.001}{2})); \quad \text{TE loss in dB/90}^\circ$$

$$\alpha Marc_{TM} := C[1 - Marc_{TM}] \exp(-C[2 - Marc_{TM}] \cdot R \cdot 0.001); \text{TM loss in}$$

cm<sup>-1</sup>

$$\alpha Marc_{TM-DB} := 1 - \log_{10}(\exp(\frac{\alpha Marc_{TM} \cdot R \cdot 0.001}{2})); \quad \text{TM loss in dB/90}^\circ$$

plot([0.1E-1·α Marc<sub>TE</sub>, 0.1E-1·α Marc<sub>TM</sub>], R = 0 .. 2, 0 .. 10, legend = ["TE", "TM"], title = "Bend Loss Calculations Marcetilli", labels = ["Radius (mm)", "Bend Loss Coefficient (cm-1)"], labeldirections = [HORIZONTAL, VERTICAL], axes = BOXED, thickness = 1, resolution = 5000, numpoints = 1000, gridlines);

plot([α Marc<sub>TE<sub>DB</sub></sub>, α Marc<sub>TM<sub>DB</sub></sub>], R = 0 .. 2, 0 .. 150, legend = ["TE", "TM"], title = "Bend Loss Calculations Marcetilli", labels = ["Radius (mm)", "Bend Loss Db / 90 degrees"], labeldirections = [HORIZONTAL, VERTICAL], axes = BOXED, thickness = 1, resolution = 5000, numpoints = 1000, gridlines);

## Lee

$$k[z_{TE}] := \frac{N_{TE} \cdot 2\pi}{\lambda}; \quad \text{TE wavenumber topographical}$$

$$k[z_{TM}] := \frac{N_{TM} \cdot 2\pi}{\lambda}; \quad \text{TM wavenumber topographical}$$

$$k1_{TE} := \frac{N[II] \cdot 2\pi}{\lambda}; \quad \text{TE wavenumber cross section rib}$$

$$k1_{TM} := \frac{N[II] \cdot 2\pi}{\lambda}; \quad \text{TE wavenumber cross section rib}$$

$$C[1 - Lee_{TE}] := \text{evalf}\left(\frac{\alpha x_{TE}^2 \lambda \cos\left(\frac{k[2x_{TE} \cdot w]}{2}\right) \exp(\alpha x_{TE} \cdot w)}{\pi(\alpha x_{TE} \cdot w + 2)}\right);$$

TE loss constant 1

$$C[1 - Lee_{TM}] := evalf\left(\frac{\alpha x_{TM}^2 \lambda \cos\left(\frac{k[2x_{TM} \cdot w]}{2}\right) \exp(\alpha x_{TM} \cdot w)}{\pi(\alpha x_{TM} \cdot w + 2)}\right);$$

TM loss constant 1

$$C[2 - Lee_{TE}] := \frac{2\alpha_{TE}(k[z_{TE}] - k_{1TE})}{k_{1TE}}; \quad \text{TE loss constant 2}$$

$$C[2 - Lee_{TM}] := \frac{2\alpha_{TM}(k[z_{TM}] - k_{1TM})}{k_{1TM}}; \quad \text{TM loss constant 2}$$

$$\alpha Lee_{TE} := C[1 - Lee_{TE}] \exp(-C[2 - Lee_{TE}] \cdot R \cdot 0.001); \quad \text{TE loss in cm}^{-1}$$

$$\alpha Lee_{TE-DB} := 10 \log_{10}\left(\exp\left(\frac{\alpha Lee_{TE} \cdot R \cdot 0.001 \pi}{2}\right)\right); \quad \text{TE loss in dB/90}^\circ$$

$$\alpha Lee_{TM} := C[1 - Lee_{TM}] \exp(-C[2 - Lee_{TM}] \cdot R \cdot 0.001); \quad \text{TM loss in cm}^{-1}$$

$$\alpha Lee_{TM-DB} := 10 \log_{10}\left(\exp\left(\frac{\alpha Lee_{TM} \cdot R \cdot 0.001 \pi}{2}\right)\right); \quad \text{TM loss in dB/90}^\circ$$

```
plot([0.1E-1·αLeeTE, 0.1E-1·αLeeTM], R = 0 .. 2, 0 .. 10, legend =
["TE", "TM"], title = "Bend Loss Calculations Lee", labels = ["Radius
(mm)", "Bend Loss Coefficient (cm-1)"], labeldirections = [HORIZONTAL,
VERTICAL], axes = BOXED, thickness = 1, resolution = 5000, numpoints
= 1000, gridlines);
```

```
plot([αLeeTE_DB, αLeeTM_DB], R = 0 .. 2, 0 .. 300, legend = ["TE",
"TM"], title = "Bend Loss Calculations Lee", labels = ["Radius (mm)",
"Bend Loss Db / 90 degrees"], labeldirections = [HORIZONTAL, VER-
TICAL], axes = BOXED, thickness = 1, resolution = 5000, numpoints =
1000, gridlines);
```

### Bend Loss Comparison

It was found advantageous to compare outputs from Marcuse, Marcatili, and Lee for both the bend loss coefficient and bend radius loss for both TE and TM modes. The following will give these plots.

**Plots TE Loss ( $\text{cm}^{-1}$ ) with respect to Bend Radius (mm)**

```
plot([0.1E-1· $\alpha$ [Marcuse-aTE], 0.1E-1· $\alpha$ qMarcuseTE, 0.1E-1· $\alpha$ MarcTE, 0.1E-1· $\alpha$ LeeTE], R = 0 .. 3, 0 .. 1, title = "Bend Loss Calculations TE", labels = ["Radius (mm)", "Bend Loss Coefficient (cm-1)"], labeldirections = [HORIZONTAL, VERTICAL], legend = ["Marcuse A[TE]", "Marcuse B[TE]", "Marcatili[TE]", "Lee[TE]"], axes = BOXED, thickness = 1, resolution = 5000, numpoints = 1000, gridlines);
```

**Plots TM Loss ( $\text{cm}^{-1}$ ) with respect to Bend Radius (mm)**

```
plot([0.1E-1· $\alpha$ [Marcuse-aTM], 0.1E-1· $\alpha$ qMarcuseTM, 0.1E-1· $\alpha$ MarcTM, 0.1E-1· $\alpha$ LeeTM], R = 0 .. 3, 0 .. 1, title = "Bend Loss Calculations TM", labels = ["Radius (mm)", "Bend Loss Coefficient (cm-1)"], labeldirections = [HORIZONTAL, VERTICAL], legend = ["Marcuse A[TM]", "Marcuse B[TM]", "Marcatili[TM]", "Lee[TM]"], axes = BOXED, thickness = 1, resolution = 5000, numpoints = 1000, gridlines);
```

**Plots TE Loss dB/90° with respect to Bend Radius (mm)**

```
plot([ $\alpha$ [Marcuse-aTEDB], alphaqMarcuseTEDB,  $\alpha$ MarcTEDB,  $\alpha$ LeeTEDB], R = 0 .. 2, 0 .. 300, title = "Bend Loss Calculations TE", labels = ["Radius (mm)", "Bend Loss Db / 90 degrees"], labeldirections = [HORIZONTAL, VERTICAL], legend = ["Marcuse A [TE]", "Marcuse B [TE]", "Marcatili [TE]", "Lee [TE]"], axes = BOXED, thickness = 1, resolution = 5000, numpoints = 1000, gridlines);
```

**Plots TM Loss dB/90° with respect to Bend Radius (mm)**

```
plot([ $\alpha$ [Marcuse-aTMDB], alphaqMarcuseTMDB,  $\alpha$ MarcTMDB,  $\alpha$ LeeTMDB], R = 0 .. 2, 0 .. 300, title = "Bend Loss Calculations TM", labels = ["Radius (mm)", "Bend Loss Db / 90 degrees"], labeldirections = [HORIZONTAL, VERTICAL], legend = ["Marcuse A [TM]", "Marcuse B [TM]", "Marcatili [TM]", "Lee [TM]"], axes = BOXED, thickness = 1, resolution = 5000, numpoints = 1000, gridlines);
```

# Appendix B

---

## MatLab Programs

---

### B.1 Fourier Spectrometer Program

The following program was devised by Dr. Paul Jessop as a tool to understand the capabilities of various highly asymmetric Mach-Zehnders as possible Fourier Spectrometers.

```
clear;
deltaL = 30448.5; % deltaL = path length difference in microns
nptsT = 400;      % nptsT = number of points in Temperature scan
nptsWL = 400;    % nptsWL = number of points in Wavelength scan
Tstep = 40/nptsT; % T = Temperature in C
%
%   Generate a spectrum of spikes near the ITU C-Band
%
wlmin = 1.546;
wlmax = 1.565;
wlstep = (wlmax-wlmin)/(nptsWL-1);
for j=1:nptsWL
    wl(j) = wlmin + (j-1)*wlstep;
    power(j) = 0;      % default is zero power at each wavelength
end
power(4)=1;
power(200)=0;
power(393)=1;
```

```

power(190)=0;
subplot(3,1,1);
plot(wl,power);
xlabel('Wavelength (um)');
ylabel('Input Power');
grid;
%
%Send that spectrum through an asymmetric MZ and scan the temperature
%
for i = 1:nptsT                                % scan temperature over n steps
    T(i) = i*Tstep;
    neff = (3.476 + 0.0001818*T(i));
    S(i) = 0;      % S is the output signal from the MZ interferometer
    for j = 1:nptsWL
        k = neff*2*pi/wl(j);
        S(i) = S(i) + power(j)*0.5*(1+cos(k*deltaL));
    end
end
subplot(3,1,2)
plot(T,S);
xlabel('Temperature (C)');
ylabel('MZ Output Signal');
grid;
%
%   Fourier Transform the output signal
%
ft = fft(S,2048);
spectrum = ft.*conj(ft);
spectrum(1)=0;      % Get rid of big DC component in FFT
spectrum(2)=0;
spectrum(2048)=0;
subplot(3,1,3);
plot(spectrum);
title(['FFT of Output Signal, nptsT = ',num2str(nptsT),',
deltaL = ',num2str(deltaL),'um']);
grid;

```

## Appendix C

---

# Various FFT Outputs due to Zero Buffering

---

In order to obtain more usable data for FFT analysis a method known as zero buffering was used. Zero buffering is a simple method by which zeros are appended to the raw data to a data number,  $N$ , equal to a factor of  $2^n$ . The following figures are various levels of zero buffering.

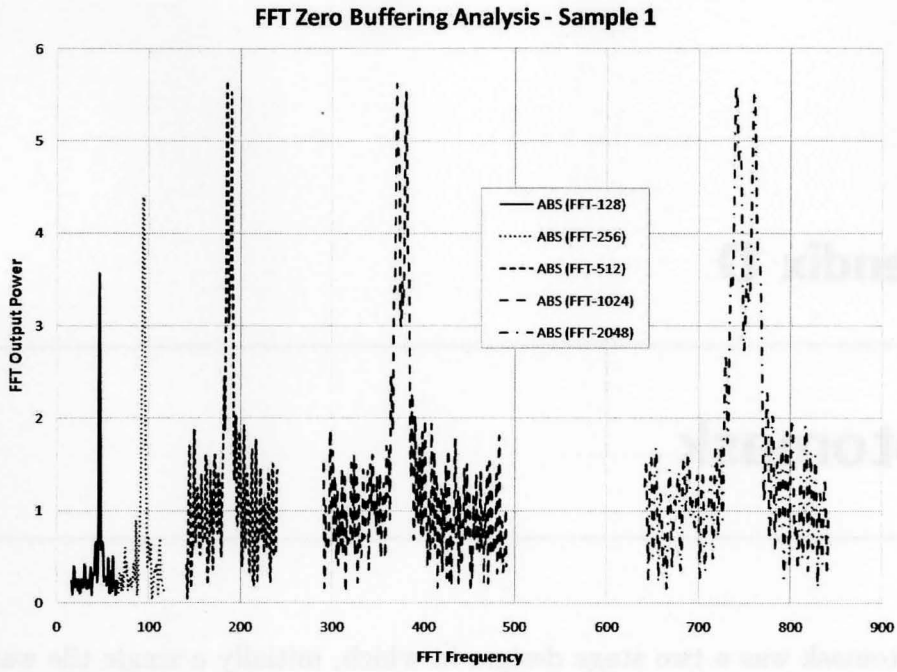


Figure C.1: Sample 1 MZI ( $\Delta L = 3.05\text{cm}$ ) - Experimental FFT output for  $\lambda=1546.12\text{nm}$  and  $\lambda=1564.68\text{nm}$  with Various Zero Buffering

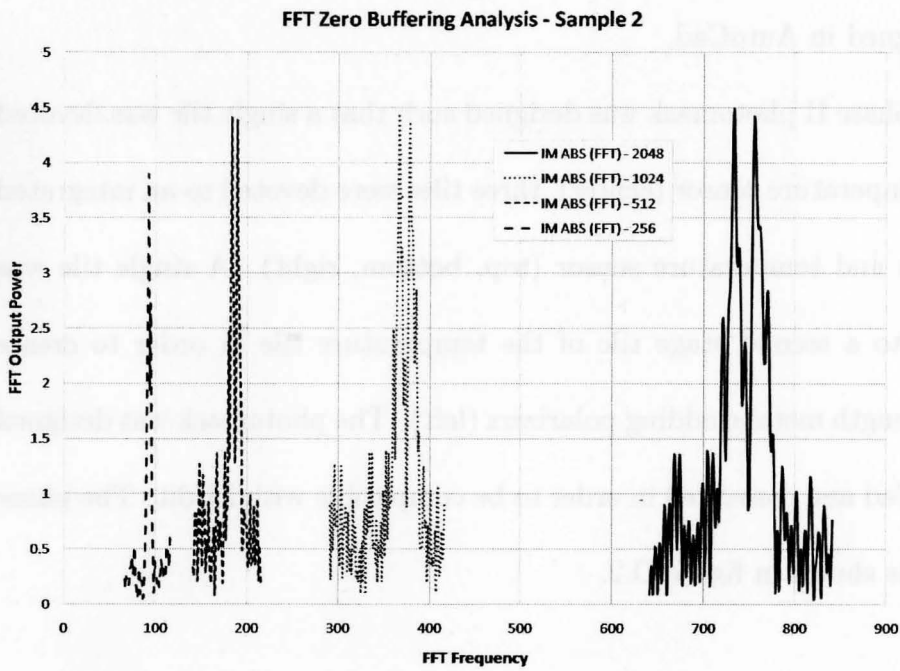


Figure C.2: Sample 2 MZI ( $\Delta L = 3.05\text{cm}$ ) - Experimental FFT output for  $\lambda=1546.12\text{nm}$  and  $\lambda=1564.68\text{nm}$  with Various Zero Buffering

## Appendix D

---

### Photomask

---

The photomask was a two stage design, in which, initially a single tile was designed and acted as the Phase I temperature sensor template. The single tile measured one inch square, and is shown in figure D.1. The phase I mask was designed in AutoCad.

The phase II photomask was designed such that a single tile was devoted to the temperature sensor (center), three tiles were devoted to an integrated vibration and temperature sensor (top, bottom, right). A single tile was devoted to a second stage tile of the temperature tile in order to create specific length metal cladding polarizers (left). The photomask was designed in AutoCad and converted in order to be compatible with LEdit. The phase II mask is shown in figure D.2.

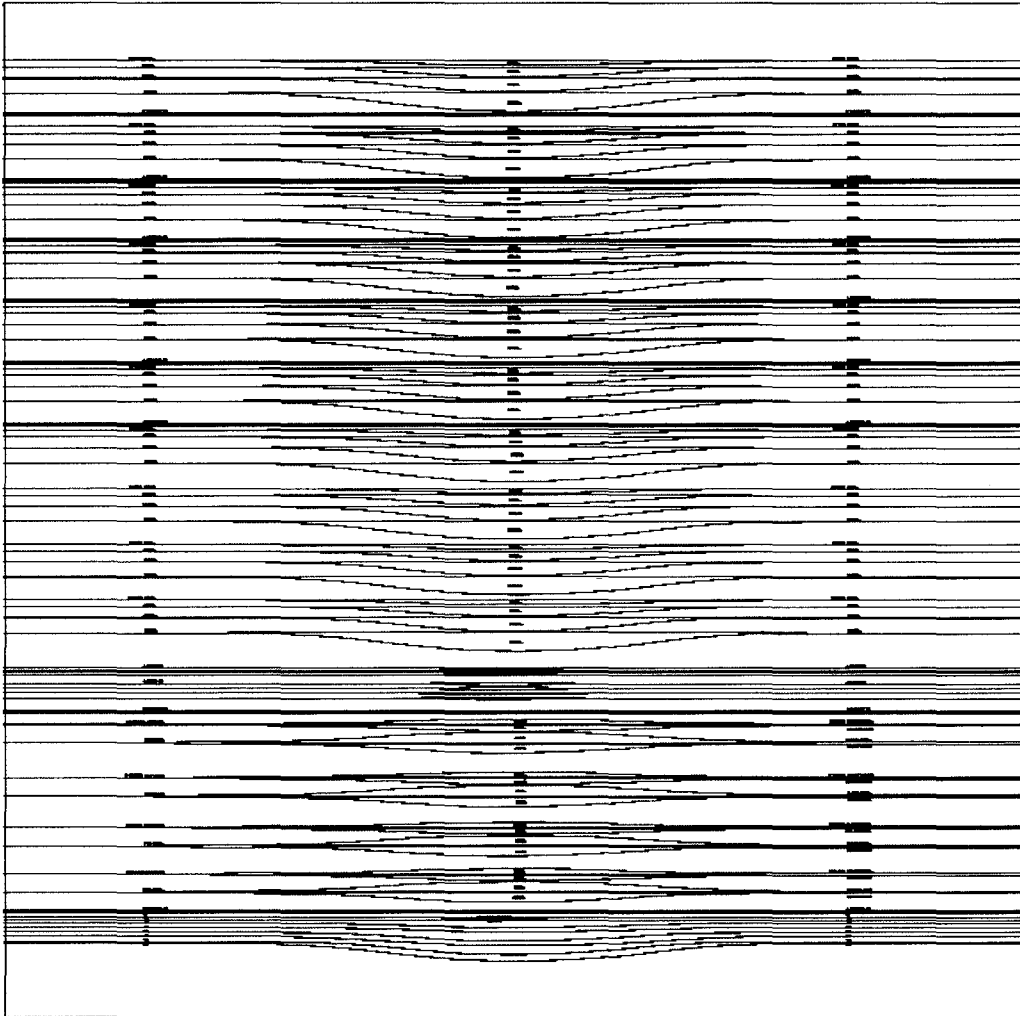


Figure D.1: Phase I Photomask Tile

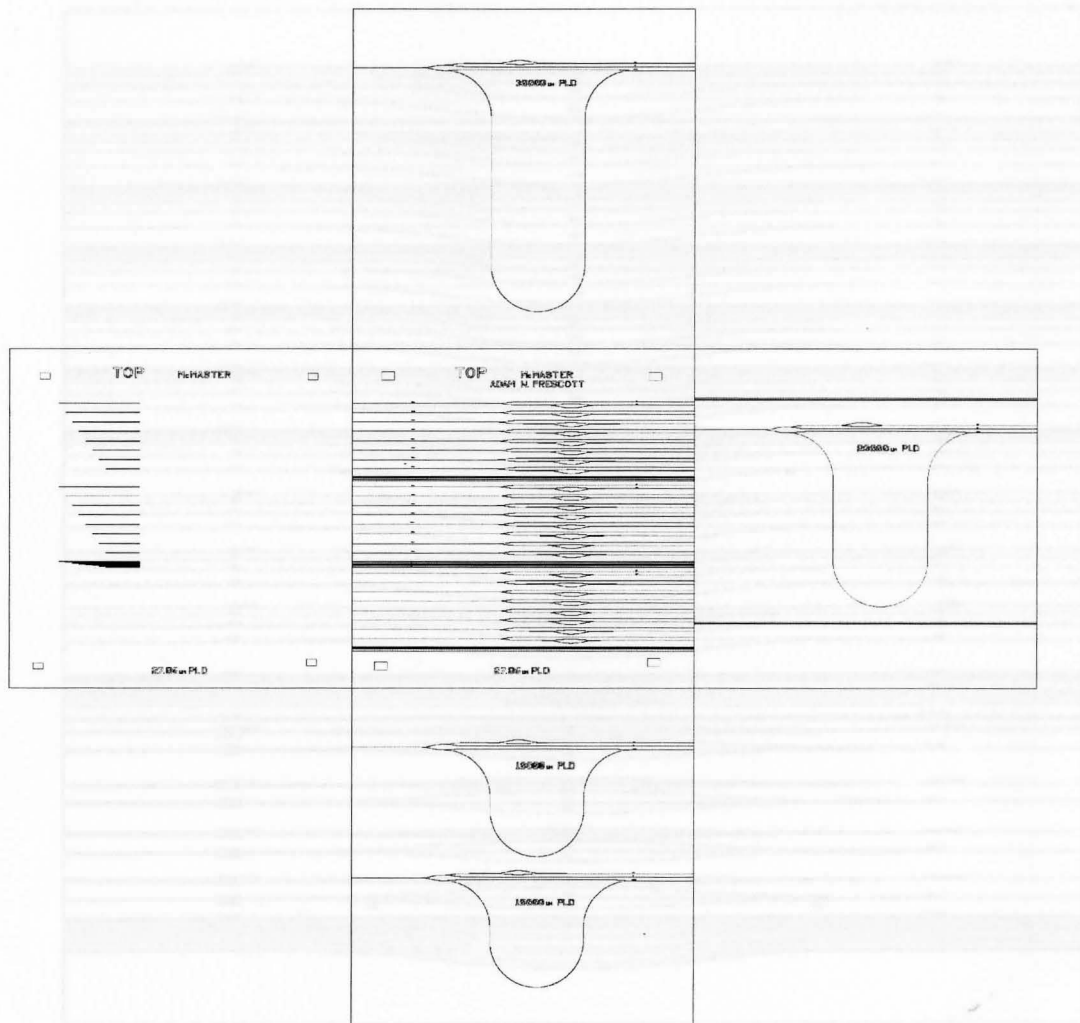


Figure D.2: Phase II Photomask



## Appendix E

---

# List of Symbols and Abbreviations

---

MZI	Mach-Zehnder Interferometer
SOI	Silicon-On-Insulator
$\Delta L$	Path Length Difference
$c$	speed of light ( $3 \times 10^8$ )m/s
$E_g(0)$	Band Energy at 0 Kelvin
$E_g(T)$	Band Energy at T Kelvin
$\epsilon_o$ [F/cm]	Permittivity in Vacuum( $8.854 \times 10^{-14}$ )
$\epsilon_r$ [F/cm]	Relative Permittivity
$h$ [J/s]	Plank's Constant ( $6.626 \times 10^{-34}$ )
$I(T), I_T$	Output Intensity
$k_o = \frac{2\pi}{\lambda}$	Wavenumber

$\mathbf{k}$	Propagation Vector
$\Lambda$	Grating Pitch
$\lambda$	Wavelength
$\lambda_o$	Wavelength in Free Space
$n$	refractive index (Bulk Silicon)
$N / N_{eff}$	Effective index (Rib Waveguide)
$N_{TE} / N_{TM}$	Effective Index (Polarized to Rib Geometry)
$\omega = 2\pi\nu$	Angular Frequency
$r_{TE, TM}$	Interface Reflection (Polarization Sensitive)
$\phi_{TE, TM}$	Interface Phase Shift (Polarization Sensitive)
$\mu[\text{H/cm}]$	Permeability in Vacuum ( $1.2566 \times 10^{-8}$ )
$W$	Rib Waveguide Width
$H$	Rib Waveguide Height
$h$	Slab Height
$\mathbf{E}[\text{V/m}]$	Electric Field Vector
$\mathbf{H}[\text{A/m}]$	Magnetic Field Vector
$\mathbf{D}[\text{C/m}^2]$	Electric Displacement
$\mathbf{B}[\text{W/m}^2]$	Magnetic Displacement
$\mathbf{P}$	Electric Polarization